M 2023

U.PORTO
FEUP FACULDADE DE ENGENHARIA
UNIVERSIDADE DO PORTO

SELF-HEALING TECHNIQUES ON VANADIUM REDOX FLOW BATTERIES

MARIANA CHIBANTE
MASTER THESIS IN CHEMICAL ENGINEERING
PRESENTED TO THE FACULTY OF ENGINEERING
OF THE UNIVERSITY OF PORTO

Master in Chemical Engineering

Self-Healing Techniques on Vanadium Redox Flow Batteries

Master dissertation

of

Mariana Chibante

Developed within the course of dissertation

held in

Vasco da Gama CoLAB - Energy Storage - Associação

Supervisor at FEUP: **Dr. Miguel Duarte**

Joint supervisor at FEUP: **Prof. Adélio Mendes**

Coordinator at Vasco da Gama CoLAB – Energy Storage - Associação: **Eng. José Fonseca**

Joint-coordinator at Vasco da Gama CoLAB – Energy Storage - Associação: **Dr. Temple Douglas**

July 2023

Acknowledgment

This work was financially supported by the Project "Baterias 2030" with the reference POCI-01-0247-FEDER-046846, co-financed by the Competitiveness and Internationalisation Operational Programme (COMPETE 2020), within the Partnership Agreement - Portugal 2020, through the European Regional Development Fund (ERDF).

I would like to start by thanking FEUP for the preparation and baggage to face opportunities like this one. It has given me the necessary tools to develop interesting work and contribute to the development of current topics, which I shall keep doing my best to apply in my work.

To Vasco da Gama CoLAB, I would like to express my appreciation for such a warm welcome and integration in the team. Their availability and willingness to help surely contributed to the development of this dissertation. I would like to mention particularly Eng. Guilherme Perestrelo for all the help in the preparation and assembly of the tests' setup and for the support regarding the execution of the tests. Dr. Diana Julião for the availability to perform the FTIR analysis. Eng. Ângela Lacerda for the help with the preparation and execution of the EIS measurements. And, finally, Dr. Alan Lima for the introduction to the lab work.

To Prof. Arménio Serra from the University of Coimbra, I would like to express my appreciation for all the interest took in the work developed, for the readiness to meet and provide counselling that largely contributed for the development of one of the technologies investigated. I would like to also thank for providing some of the reagents necessary for the development of this idea (the silane compounds).

To the supervisors and coordinators of this dissertation: Dr. Miguel Duarte, Prof. Adélio Mendes, Eng. José Fonseca and Dr. Temple Douglas, I would like to thank for all the support, availability and guidance during the development of this work. To Prof. Adélio Mendes I would like to thank for the resources and contacts provided to enrich this thesis. To Dr. Miguel Duarte, I would like to appreciate the readiness to help and discuss the development of this work. And, most importantly, to Eng. José Fonseca, who followed the daily development of this work, I would like to express my gratitude for all the time, patience and guidance that certainly played an important role in the evolution and outcome of this dissertation.

Finally, I would like to thank the people from my daily life that have always supported me and encouraged me to achieve my goals. A special thanks to my parents and brother, to my friends and boyfriend, some of whom also took on this journey of developing the master's thesis.

All the people mentioned have positively impacted this work, in several different ways, and I would like to express my gratitude to them for making this dissertation possible.

Abstract

The all-vanadium redox flow batteries (VRFBs) emerged as one promising energy storage technology. However, these may present electrolyte leakage problems that result in electrolyte imbalance, loss of energy capacity and loss of battery efficiency. One way of mitigating small leaks without human intervention is by employing self-healing techniques to ensure the sealing of the leakage and the normal function of the battery as soon as it appears.

This work aimed to develop self-healing techniques to prevent electrolyte leakage problems in VRFBs. Two different approaches were explored: inducing the precipitation of sulphate salts by the application of a calcium carbonate film in PTFE gaskets and applying an epoxy film with silane-terminated compounds in PVC gaskets to induce crosslinking reactions whenever a leak occurs.

Calcium carbonate was mixed with a binder, PVDF, to adhere to the gaskets and induce the precipitation of sulphate salts to obstruct possible leaks. It was determined that a film with 60% ratio between solids and solvent, where the solids are 95% $CaCO_3$ and 5% PVDF is the optimal option. The precipitates resulting from this technique were analysed through FTIR and evidenced the presence of sulphates, hydroxides and oxides. It was determined that the film was able to prevent loss of electrolyte through a leak with a cross-sectional area of 0.25 mm^2 for a circulation flowrate of 180 $mL \cdot min^{-1}$, using gaskets for a cell with an active area of 4 cm^2. The main problems encountered were the poor adhesion of the calcium carbonate film to the gaskets which could exacerbate the leakage due to uneven thickness of the gasket.

Regarding the application of silane-terminated compounds, these were incorporated in an epoxy resin, and several compositions were tested. The tests with the best results – meaning that they contained the electrolyte, allowed a uniform application and contained a considerable concentration of silane monomers – 30% of silanes on component A, or 50% of silanes in component B. The resins were taken to FTIR analysis that evidenced the presence of silica network for all the samples, so it cannot be stated that the hydrolysis mechanism is only triggered by contact with the electrolyte. However, it seems to be able to prevent the loss of electrolyte.

EIS measurements were performed on a single cell to evaluate the influence of the application of calcium carbonate film on the resistances of the cell. The values obtained for the ohmic and charge transfer resistances were 0.660 and 0.202 $\Omega \cdot cm^2$ for the test with the film, and 1.101 and 0.542 $\Omega \cdot cm^2$ for the test without the film, respectively. Regarding these results, there seems to be no significant contamination of the electrolyte.

Keywords (theme): vanadium redox flow battery, electrolyte leakage, self-healing

Resumo

As baterias de escoamento de vanádio surgiram como uma tecnologia promissora de armazenamento de energia. No entanto, estas podem apresentar problemas de fuga de eletrólito que resultam em desequilíbrio de cargas do eletrólito, perda de capacidade de energia e perda de eficiência da bateria. Uma forma de mitigar pequenas fugas sem intervenção humana é pela aplicação de técnicas de auto cura para garantir a vedação da fuga e o funcionamento normal da bateria assim que esta apareça.

Este trabalho teve como objetivo desenvolver técnicas de auto cura para prevenir problemas de vazamento de eletrólito. Foram exploradas duas abordagens diferentes: induzir a precipitação de sais de sulfato pela aplicação de um filme de carbonato de cálcio em juntas de PTFE e aplicar um filme de resina epóxi com compostos que contenham grupos silanos em juntas de PVC, para induzir reações de reticulação sempre que ocorrer um vazamento.

O carbonato de cálcio foi misturado com um ligante, PVDF, para aderir às juntas e induzir a precipitação de sais de sulfato para obstruir possíveis vazamentos. Foi determinado que um filme com uma proporção de 60% entre sólidos e solvente, sendo os sólidos 95% CaCO3 e 5% PVDF, é a opção ótima. Os precipitados resultantes dessa técnica foram analisados por FTIR e evidenciaram a presença de sulfatos, hidróxidos e óxidos. Foi determinado que o filme foi capaz de evitar a perda de eletrólito através de um vazamento com uma área de secção transversal de 0,25 mm^2 para um caudal de eletrólito de 180 $mL \cdot min^{-1}$. Os principais problemas encontrados foram a fraca aderência do filme de carbonato de cálcio ao material das juntas, o que poderá agravar o vazamento devido à espessura irregular da junta.

Quanto à aplicação de silanos, estes foram incorporados numa resina epóxi e várias composições foram testadas. Os testes com os melhores resultados - ou seja, aqueles que continham o eletrólito, permitiam uma aplicação uniforme e continham uma concentração considerável de monómeros de silano - continham 30% de silanos no componente A, ou 50% de silanos no componente B. As resinas foram submetidas a análise por FTIR, que evidenciou a presença de uma rede de sílica em todas as amostras e, portanto, não se pode afirmar que o mecanismo de hidrólise seja acionado apenas quando há vazamento de eletrólito, no entanto, aparenta prevenir a perda de eletrólito.

Foram realizadas medições de EIS numa célula completa para avaliar a influência da aplicação do filme de carbonato de cálcio nas resistências da célula. Os valores obtidos para as resistências óhmica e de transferência de carga foram de 0.660 e 0.202 $\Omega \cdot cm^2$ para o teste com o filme, e 1.101 and 0.542 $\Omega \cdot cm^2$ para o teste sem o filme, respetivamente. Com base nestes resultados, parece não haver contaminação significativa do eletrólito.

Declaration

I hereby declare, under word of honour, that this work is original and that all non-original contributions is indicated and due reference is given to the author and source

3rd of July of 2023,

Mariana Chibante

Index

List of Figures

List of Tables

Notation and Glossary

Im(Z)	imaginary part of the impedance	$\Omega \cdot cm^2$
m	mass	g
n	number of moles	mol
R	resistance	$\Omega \cdot cm^2$
Re(Z)	real part of the impedance	$\Omega \cdot cm^2$
V	volume	mL

Greek Letters

ρ	density	$g \cdot cm^{-3}$

Indexes

Ω	ohmic
CT	charge-transfer

List of Acronyms

AS	3-(Aminopropyl)dimethylmethoxysilane
DMAc	N,N-dimethylacetamide
DMF	Dimethylformamide
EIS	Electrochemical impedance spectroscopy
ES	Methoxydimethyl-(oxiran-2-ylmethyl)silane
FTIR	Fourier-transform infrared spectroscopy
MEMO	(3-Methacryloxypropyl)trimethoxysilane
NMP	N-methyl-2-pyrrolidone
PTFE	Polytetrafluoroethylene
PVC	Polyvinylchloride
RES	Renewable energy sources
RFB	Redox flow battery
UV	Ultraviolet
VRFB	Vanadium redox flow battery

1 Introduction

1.1. Framing and presentation of the work

Energy production from renewable energy sources (RES) is a topic under investigation for several decades now. Production of energy from RES is the main strategy to meet the increasing energy demand while accomplishing the goals set by the Paris Agreement and the European Union (EU) for the decrease in the greenhouse gas emissions (Gordon and Weber 2021, Ciucci 2023).

However, RES are characterized by their intermittency throughout the day or year (Thoubboron 2022). Therefore, RES alone cannot guarantee a reliable supply, which could become a problem of shortage in periods of high energy consumption and low production, or curtailment in low consumption periods and high production. This implies a combination of various renewable energy sources and investing in energy storage systems to prevent energy shortages (Energy Storage 2023).

Redox flow batteries (RFBs) are one of the promising technologies for energy storage due to the possibility of decoupling for different power and energy requirements, by changing the size and number of cells in a stack and the volume of the electrolyte, respectively (Lourenssen, et al. 2019). To mitigate the consequences of crossover, the all-vanadium redox flow batteries (VRFBs) emerged, using $V^{(II)}/V^{(III)}$ and $V^{(IV)}/V^{(V)}$ as redox couples for the negative and positive half-cells, respectively (Iwakiri, et al. 2021).

Despite the many advantages, the VRFBs present electrolyte leakage problems, meaning that electrolyte volume is lost to the exterior of the battery. These problems result in electrolyte imbalance, loss of energy capacity and loss of the battery efficiency, translating in extra costs in maintenance and operation (Huang, et al. 2022). Solving this problem without human intervention may be possible with self-healing techniques to ensure the sealing of the leakage and the normal function of the battery as soon as it appears.

1.2. Presentation of the company

Vasco da Gama CoLAB – Energy Storage – Associação is a non-profit organization committed to the investigation and development in two main areas - electrochemical energy storage, and power electronics and energy management.

The mission of this organization is to merge academia, industry and start-ups to develop mid-TRL solutions in the field of power electronics and energy management, design and

development of modules and packs, and cell scale-up, where the redox flow batteries are included.

1.3. Contribution of the author to the work

In this dissertation, the author contributed with the research and investigation regarding the development of the context and gathering the state-of-the-art in the scope of the topic. Based on the research executed, the author contributed with the development of possible pathways to respond to the objective of this dissertation. The author also contributed to the development and execution of the methods to implement the chosen paths.

Finally, from the results obtained, the author was able to fit them in the scope of the topic and draw conclusions, while suggesting further work in this area.

1.4. Organization of the dissertation

This document is divided in 6 chapters. The first chapter aims to introduce the reader to the topic of the dissertation. There is a brief presentation of the topic and its interest is explained. The company where this work was developed is presented, and there is also mention of the contribution of the author to the work.

The second chapter presents the contextualization of the topic and a synthesis of important discoveries and developments in the area in question. This chapter leads the reader towards the work developed within this dissertation.

The third chapter elaborates the work developed to respond to the objectives of this thesis, while explaining the methods used and the conditions of each experiment.

Chapter 4 presents the results obtained in the scope of the work developed and thoroughly analyses them, while inserting them in the objective of the dissertation.

In chapter 5, the main conclusions are presented as well as possible paths to proceed to improve or continue the work developed.

Lastly, chapter 6 presents a reflection regarding the work developed by the author.

2 Context and State of the art

The increased use of electrical energy and the need for the transition to RES calls for an investment in energy storage technologies. Energy storage is the solution to prevent power shortages caused by the intermittent nature of RES, and to guarantee a reliable energy supply for on and off-grid applications (Jirabovornwisut and Arpornwichanop 2019).

One interesting technology of energy storage field are RFBs due to their many advantages: fast response, long service life, safety, flexible design and relatively low environmental impact (Skyllas-Kazacos, Cao and Kazacos, et al. 2016). Another great advantage is the ability to change the power output and the energy capacity independently, since the first is related to the area of the cells in a stack, while the other is related to the volume of the electrolyte and its concentration (Sanchez-Díez, et al. 2021).

The main components of RFBs are the two tanks where the electrolyte solution is kept and the stack where the redox reactions occur (Sanchez-Díez, et al. 2021). Within one cell, there are two current collectors, two bipolar plates, two electrodes and one membrane, as illustrated in Figure 2.1 (Cho, Krieg e Kerres 2018).

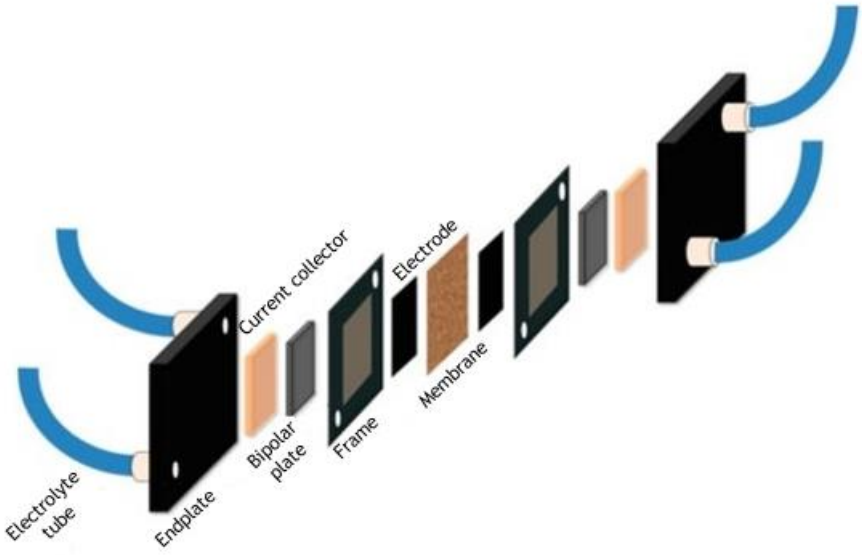

Figure 2.1 Components of a RFB single cell. Adapted from (Cho, Krieg e Kerres 2018).

There are different chemistries that have been investigated for RFBs: VRFB, including generation 1 VRFB, generation 2 vanadium–bromine battery, and generation 3 mixed-acid VRFB; polysulfide-based flow battery; zinc-bromine flow battery; cerium-zinc flow battery; and iron–chromium flow battery (León, et al. 2006, Xu, et al. 2020, Zeng, et al. 2016, Li and Lu 2021, Amini and Pritzker 2020). Of all these redox couples, the $V^{(II)}/V^{(III)}$ and $V^{(IV)}/V^{(V)}$ pair has been

the most studied, and generation 1 VRFBs have seen the highest level of commercialization to date (Choi, et al. 2017).

RFBs can have several configurations, according to the type of technology used. One of the possible configurations are the membraneless batteries that, as the name suggests, operate without a membrane, aiming to reduce capital costs (Navalpotro, et al. 2018). However, the major disadvantage is the high crossover effect since the separation of the two electrolyte solutions is only dependent on the laminar flow or on their immiscibility (Bamgbopa, Almheiri and Sun 2017). In semi-solid flow batteries, the active species are in a suspension instead of a solution, allowing to overcome solubility problems (Ventosa 2022). The main disadvantage is the high viscosity of the electrolyte, that affects the performance for high currents (Wang, Chai and Jiang 2021). Another configuration is the metal-air flow battery, where a metal reacts on the anode side and oxygen on the cathode side. These batteries are being explored to increase the energy density. The main drawback is the price of the catalysts necessary to the operation of the battery (Han, et al. 2018). Zinc-bromine RFBs consist of another possible configuration. The physical state of the active species depends on the charge/discharge phase – when the battery is fully charged, zinc is in solid state, which contributes to a higher energy density. However, these batteries require the use of auxiliary components to tackle their reduced efficiency and allow a safe operation, like complexing agents to prevent bromine vapour emissions, which increases capital costs (Sanchez-Díez, et al. 2021).

2.1. Vanadium Redox Flow Batteries

VRFBs were initially proposed in the 1980s by Skyllas-Kazacos as a solution for the cross-contamination problems, low reversibility and self-discharge detected in other RFBs (Iwakiri, et al. 2021). VRFBs exploit the four oxidation states of vanadium to compose the redox couples, since they have very different half-cell potentials. The electrochemical reactions at the positive and negative electrodes occur as presented in equations (2.1) and (2.2), respectively (Skyllas-Kazacos, Cao and Kazacos, et al. 2016).

$$\mathrm{VO_2^+(aq) + 2H^+(aq) + e^- \rightleftharpoons VO^{2+}(aq) + H_2O(l)} \quad (2.1)$$

$$\mathrm{V^{3+}(aq) + e^- \rightleftharpoons V^{2+}(aq)} \quad (2.2)$$

These batteries became known as 1st generation VRFBs. One of the main advantages is the high equilibrium cell voltage of 1.25 V. (Jirabovornwisut and Arpornwichanop 2019, Cunha, et al. 2014, Choi, et al. 2017). Higher cell voltage translates into higher power density, reducing the number of cells required for a given power output (Cheng 1991).

The major disadvantages of 1st generation VRFBs are the low energy density when compared to other battery technologies and limited operating temperature range - $V^{(V)}$ tends to precipitate

at temperatures above 40 °C, while the $V^{(II)}$, $V^{(III)}$ and $V^{(IV)}$ aqueous compounds precipitate below 10 °C (Rahman 1998). The operating temperature range can be increased by decreasing the concentration of the electrolyte. However, vanadium salt concentrations of at least 2 mol·L^{-1} are recommended to maximize the energy density (Carvalho Jr, et al. 2021).

To increase the solubility of the vanadium species in the electrolyte, 2nd generation VRFBs were proposed. They operate with a vanadium-halide solution that incorporates HBr and HCl in the electrolyte. The chloride ions react with vanadium ions to give vanadium (II) and vanadium (III) chloride on the negative side of the cell. While on the positive side the bromine ions react with chloride ions, releasing two electrons that are consumed in the reactions on the negative side (Skyllas-Kazacos 2003). These batteries can operate with vanadium concentrations of 2-3 M in a solution of 7-9 M of HBr and 1.5-2 M of HCl (Skyllas-Kazacos, Kazacos, et al. 2010). The main disadvantage is the need to use complexing agents to prevent the formation of bromine vapours, which represents an economic barrier (D. Kim, et al. 2019).

To increase the operating temperature range, 3rd generation VRFBs proposed the use of a mixed-acid electrolyte, combining HCl with H_2SO_4 present in the electrolyte (Li, et al. 2011). The temperature is limited to 40 °C due to the endothermal reaction of $V^{(V)}$ with water, as explained in equation (2.3). Therefore, increasing the temperature favours the precipitation of V_2O_5. The addition of HCl increases the concentration of protons, shifting the equilibrium of equation (2.3) to the left, and consequently increasing the upper limit of the operating temperature (Cheng, Electrolyte Optimization and Studies for the Vanadium Redox Flow Battery 1991). The main disadvantage presence of chlorine ions due to the addition of HCl, that brings the additional risk of the formation of HCl vapours during operation at higher temperatures (Skyllas-Kazacos, Cao and Menictas, et al. 2018).

$$2VO_2^+(aq) + H_2O(l) \rightleftharpoons V_2O_5(s) + 2H^+(aq) \quad (2.3)$$

VRFBs have potential for several applications: load-levelling – store energy produced off-peak hours, to have enough energy to provide when the price is high; as an independent emergency power source – to assure operation of important equipment in case of a power failure; for remote area power supply and for large scale photovoltaic applications – the energy produced needs to be stored for later use (Rahman 1998, Cunha, et al. 2014). These batteries are already on the market, however, their commercialization is limited due to their low energy density (suitable for stationary applications only due to the required size of the tanks), which depends on the vanadium concentration on the electrolyte. Thus, the electrolyte solution is one of the key components of the battery (Carvalho Jr, et al. 2021).

2.1.1 Components of the Vanadium Redox Flow Batteries

A vanadium redox flow cell configuration was presented previously in Figure 2.1. The main components of a battery are the membrane, electrodes, bipolar plates, gaskets, flow fields, current collectors and the electrolyte that is stored in tanks (Lourenssen, et al. 2019).

The membranes used in VRFBs can be cation exchange membranes, anion exchange membranes, amphoteric membranes, non-ionic separators or nanofiltration membranes. The most important characteristics in a membrane are high ion exchange capacity, high electrical conductivity, good chemical and thermal stabilities, low swelling ratio, low surface resistance, low vanadium ion penetration, water migration and low cost (Lim, Ulaganathan and Yan 2015). Cation exchange membranes allow the exchange of protons to even the charges in the positive and negative sides of the cell and prevent the crossover of negative ions. They are composed of fixed ionic functional groups responsible for creating electrostatic bonds with the protons from the electrolyte solution and allowing their passage to the other side of the cell, and mobile counter-ions that are replaced by these protons, to keep the membrane electrically neutral. Nafion is one of the most common materials used (Lim, Ulaganathan and Yan 2015).

The electrode is the electrochemical reaction site and, therefore, directly affects the polarization of the battery (Huang, et al. 2022). The activity of the electrode determines the potential that needs to be sacrificed to start the electrochemical reactions, and, therefore, affects the activation polarization. Its porosity influences the distribution of the electrolyte, and, consequently, the concentration polarization. Lastly, its high conductivity decreases the resistance of the cell and the ohmic polarization (Pinto, Oliveira and Falcão 2018, Pinto, Oliveira and Falcão 2018).

The bipolar plates should conduct the current and separate each cell. Their characteristics must include high conductivity, strong current collection capability, high stability and corrosion resistance. In VRFBs the materials employed for bipolar plates are based on graphite. Metal and carbon-plastic composites have also been investigated (Kim, Kim and Lee 2014, Sanchez-Díez, et al. 2021). Bipolar plates based on graphite present high conductivity and are easy to machine comparing to other materials investigated, however it also has disadvantages such as high cost and the complicated preparation process (Lee, et al. 2012). Flow channels might be employed in bipolar plates to promote an even distribution of the electrolyte, and to decrease the pressure drop across the cell and, therefore, lower the required pumping power to circulate the electrolyte. Although there are several designs commonly used, they should be carefully chosen so as not to have the opposite effect on the performance of the cell (Tian, et al. 2011, Huang, et al. 2022).

Gaskets are used to connect sequential components in the cell. They are usually placed between the bipolar plate and the membrane, composing the necessary thickness for the

electrode to have a satisfactory contact with both components (Lourenssen, et al. 2019). To maintain this thickness, hard materials are usually employed, such as polytetrafluoroethylene (PTFE) and polyvinyl chloride (PVC). Other materials can be used as secondary sealants to allow the correct assembly of the cell without using excessive amounts of pressure, which would contribute to the aggravation of problems such as electrolyte leakages (Mohamed, et al. 2012).

Finally, the electrolyte is an important component of the battery - where the energy is stored and greatly affects the performance of the battery. In VRFBs, the electrolyte is responsible for a major percentage of the total cost of the battery – between 30% and 50%, depending on the specifications of the battery (Martin, Schafner and Turek 2020). The constituents of an electrolyte are the active redox species and the supporting electrolyte, that includes the solvent and the supporting salt (Milshtein, et al. 2017). In VRFBs, using the same active species in the catholyte and negolyte ($V^{(V)}/V^{(IV)}$ and $V^{(III)}/V^{(II)}$) allows to prevent capacity loss due to cross-contamination (Weber, et al. 2011). The solvent used is water, due to its high availability and low cost, high conductivity, low viscosity, and being capable of dissolving a wide variety of metals (Iwakiri, et al. 2021). The supporting electrolyte is H_2SO_4 since it contributes to a higher conductivity (Lourenssen, et al. 2019).

Several studies have focused on the solubility of the vanadium species in the electrolyte to analyse the influence of temperature and concentration on the precipitation behaviour (Cheng 1991, Rahman 1998, Carvalho Jr, et al. 2021, Skyllas-Kazacos, Cao and Kazacos, et al. 2016). The optimal composition of the electrolyte has been found to be 1.5-2 M of V^{5+} in 3 M of H_2SO_4, for an operating temperature range between 10 °C and 40 °C (Lourenssen, et al. 2019).

The energy density of the battery is essentially determined by the vanadium concentration – increasing the concentration, increases the energy density and decreases the volume needed to store the electroactive material (Carvalho Jr, et al. 2021). As previously mentioned, this parameter also limits the operating temperature of the battery to the range of 10 °C to 40 °C, for reasonable concentrations of vanadium in the electrolyte. The relation between solubility and temperature is not the same for all vanadium compounds – the extent of equation (2.3) increases with higher temperatures, while for lower temperatures, besides the formation of aqueous compounds, the precipitation of sulphate salts of $V^{(II)}$, $V^{(III)}$ and $V^{(IV)}$ occurs according to equations (2.4), (2.5) and (2.6), respectively.

$$V^{2+}(aq) + {SO_4}^{2-}(aq) \rightleftharpoons VSO_4(s) \tag{2.4}$$

$$2V^{3+}(aq) + 3{SO_4}^{2-}(aq) \rightleftharpoons V_2(SO_4)_3(s) \tag{2.5}$$

$$VO^{2+}(aq) + {SO_4}^{2-}(aq) \rightleftharpoons VOSO_4(s) \tag{2.6}$$

The concentration of H_2SO_4 also influences the stability of the vanadium species – from equations (2.4), (2.5) and (2.6), it is understood that for higher concentrations of the supporting

electrolyte, the concentration of sulphate ions increases, contributing to the precipitation of $V^{(II)}$, $V^{(III)}$ and $V^{(IV)}$ salts (Cheng 1991). On the other hand, Rahman determined that the $V^{(V)}$ solubility increases with higher concentration of H_2SO_4 (Rahman 1998). The explanation for this phenomenon is based on the previously explained equation (2.3). Complementing this analysis, Rahman and Skyllas-Kazacos, et al. also present equations (2.7), (2.8) and (9) to justify the consumption of VO_2^+ ions with the increase of sulphate ions, which also contributes to shifting the equilibrium of equation (2.3) to the left, preventing the formation of V_2O_5 (Rahman 1998, Skyllas-Kazacos, Cao and Kazacos, et al. 2016).

$$VO_2^+(aq) + HSO_4^-(aq) \rightleftharpoons VO_2SO_4^-(aq) + H^+(aq) \quad (2.7)$$

$$VO_2^+(aq) + SO_4^{2-}(aq) \rightleftharpoons VO_2SO_4^-(aq) \quad (2.8)$$

$$VO_2^+(aq) + VO_2SO_4^-(aq) \rightleftharpoons (VO_2)_2SO_4(s) \quad (2.9)$$

There have been several additives studied to improve the performance of the electrolyte. In Skyllas-Kazacos, et al., organic and inorganic additives are mentioned as possible precipitation inhibitors. It is determined that these compounds allow to extend the induction times of the precipitation phenomenon, however, they do not increase the solubility of vanadium ions. Therefore, precipitation would still occur if solutions remained at high or low temperatures for long periods of time. Limiting the range of the state-of-charge of the battery is also proposed to prevent precipitation since none of the vanadium species would be at the saturation level (Skyllas-Kazacos, Cao and Kazacos, et al. 2016).

2.1.2 Electrolyte leakage problems and associated causes

One of the challenges associated with VRFBs is electrolyte leakage. Leakages are essentially induced by uneven stress distribution in the stack along with electrolyte surface tension that give rise to the capillary effect. Applying excessive amounts of stress in any component of the stack can lead to plastic deformation or even cracks, that exacerbate the electrolyte leakage (Xiong, et al. 2018).

Leaks can affect the core performance of the battery by causing capacity attenuation. The capacity of the battery is determined by the volume of the electrolyte and the solubility of the electroactive species – the more species available to store energy, the bigger the capacity of the battery (Huang, et al. 2022).

To prevent this phenomenon in the long-term operation of the battery, gaskets and O-rings can be combined to provide the optimum sealing of the stack, by the application of compressive forces on the endplates (Mohamed, et al. 2012). Performing mechanical analyses of the cell stack to predict the stress distribution and the mechanical response of all components allows

to enhance the stack design and assembly. Optimizing these characteristics avoids material failure and electrolyte leakage, increasing the lifetime of the battery (Xiong, et al. 2018).

2.1.3 Self-healing techniques

Self-healing is a term originated from software-based systems and can be defined as the ability of a system to act, to prevent and react to failure, in the absence of human intervention (Ganek and Corbi 2003). The state of the system can be classified as normal, damaged or broken. Self-healing is triggered when it is detected that the system is damaged – standard operating levels are no longer attained, and restorative actions are put into practice. These actions should restore the normal functioning of the system before the broken state is reached and the system is no longer able to provide acceptable service (Varga and McMillan 2022). In the context of electrolyte leakage in VRFBs, self-healing can be understood as the chain of events that is triggered when a leak occurs, and that is able to stop it, preventing the aggravation of this problem and further loss of electrolyte.

Some of the methods to prevent electrolyte loss are essentially related to the assembly of the stack (Mohamed, et al. 2012). As mentioned in the previous subsection, uneven stress distribution and magnitude is in the root of the problem and so the investigation of these key components under specified sealing gasket designs and clamping forces is important (Xiong, et al. 2018).

In other systems, methods that consist in physically covering the leak have been investigated as self-healing. One of the approaches developed for pressurized pipelines is the Platelet Technology™. The method was developed based on the human body leak sealing method and consists on locating leaks in pressurized pipelines and placing platelets above the location of the leak. Since the flow is modified around the leak, fluid forces entrain them into the leak and hold them against the pipeline wall. The platelets are designed specifically for each operation, and so the materials and geometry of the platelets are optimized according to the problem in question (Evans, Ryan and McEwan 2007). This technique probably would not be applicable in VRFBs - the addition of platelet-like compounds to the electrolyte could damage the electrodes and the membrane, besides affecting the performance of the battery due to its higher viscosity.

Methods based on precipitation reactions have also been explored in other systems. In concrete structures under the combination of sustained loading and high-water pressure, direct tension cracks can be sealed by filling them with products of various chemical and physical reactions. One of the mechanisms responsible for self-healing in these systems is the precipitation of calcium carbonate. Calcium ions are available in the inner parts of the crack wall and are dissolved in water, that contains carbonate ions. Since calcium carbonate is practically insoluble in water, this salt is able to remediate the crack to some extent (Hooshmand, et al.

2020). Another self-healing technique has been explored in the self-repair of lead halide perovskite solar modules. For this investigation, an encapsulated perovskite solar cell module damaged by mechanical impact was simulated, and the Pb leakage was quantitatively measured. The limitation of the leakage was tested based on the self-repair ability of polymers when subjected to temperatures higher than their glass transition temperature. Therefore, an epoxy resin-based polymer was incorporated in the encapsulation of perovskite solar modules and revealed a higher mechanical resistance and a successful reduction of the Pb leakage when compared to other methods of encapsulation. The self-healing properties of this polymer were triggered by the heat on sunny days that brings the temperature above the glass transition temperature (Jiang, et al. 2019).

Precipitation as a self-healing technique in VRFBs

Precipitation can be explored as a self-healing technique in electrolyte leakage control in VRFBs. This mechanism can either be triggered by chemical reactions, or by changing certain parameters that affect the solubility of compounds present in the electrolyte. These parameters can be the concentration of these compounds, or temperature, for example (Skyllas-Kazacos, Cao and Kazacos, et al. 2016). The limiting temperatures and concentrations of each vanadium species in the electrolyte have already been mentioned in previous subsections - it is known that the solubility of vanadium species changes differently with temperature and sulphate concentrations. Therefore, inducing precipitation by changing these two parameters and guaranteeing an efficient self-healing mechanism for all states of charge of the battery might be a difficult task. One possible alternative is to induce the precipitation of sulphate salts since the supporting electrolyte is the same for both sides of the cell. The precipitation of sulphate salts can be achieved through acid-base neutralization – using a strong base like sodium hydroxide would lead to the formation of sodium sulphate and water, according to equation (2.10).

$$\mathrm{H_2SO_4(aq) + 2NaOH(aq) \rightleftharpoons Na_2SO_4(s) + 2H_2O(l)} \qquad (2.10)$$

However, it would not be practical to add sodium hydroxide to the electrolyte – the precipitation of sodium sulphate would not be confined to the area of the leak and, therefore, could damage the electrodes, membrane, and pumps, besides affecting the performance of the battery.

One possible mechanism to have sodium ions available whenever a leakage occurs could be through the application of sodium polyacrylate hydrogel in the gaskets of the stack. The behaviour of sodium polyacrylate gel has been studied regarding its kinetics and degree of swelling for different media and crosslink densities. It was determined that the degree of swelling is maximum in neutral media, decreasing for higher crosslink densities. For pH values under 3, the degree of swelling is very low due to the replacement of the sodium ions with

protons in the gel, leading to the formation of polyacrylic acid (Elyashevich, Bel'nikevich and Vesnebolotskaya 2009). This means that, when exposed to the acidic environment of the electrolyte, sodium ions would quickly be released, contributing to a fast sealing of the leak. However, the synthesis of the sodium polyacrylate hydrogel involves the use of several toxic compounds, which could be released due to the dissolution of the gel in the electrolyte. Given that, a safer technique should be explored (Arens, et al. 2019).

The precipitation of other sulphate salts can be explored as a self-healing technique. A study on sulphate removal from waste chemicals investigated the feasibility of using calcium and barium to induce the precipitation of sulphates. It was determined that, for a concentration of 80 $g \cdot L^{-1}$, the percentage of sulphate removal with barium was 61,4 % and with calcium was 99 % (Benatti, Tavares and Lenzi 2009). In fact, the solubility of calcium sulphate in acidic media is lower than the solubility of sodium sulphate, meaning that precipitation of sulphates as a self-healing technique should be more effective with calcium ions (Toro, Dobrosz-Gómez and García 2014, Li and Demopoulos 2005).

To trigger this precipitation, calcium ions need to be available to the electrolyte whenever a leak occurs. This can be achieved by applying in the gaskets a calcium salt that is more soluble than calcium sulphate in the electrolyte – to ensure that the dissolution and precipitation rate are high enough to prevent the loss of a considerable amount of electrolyte before sealing the leak.

Calcium carbonate is an example of a non-hazardous salt that can be applied in this technique. Through the analysis and comparison of several studies focused on the solubility of these two calcium salts in several environments, it is possible to predict that the solubility of calcium carbonate in the electrolyte should be much higher than the solubility of calcium sulphate (Gal, et al. 1996, Kurdowski and Bochenek 2012, Goss, et al. 2007). In fact, calcium carbonate has already been studied as a neutralizing agent in treatment plants of acid mine drainage effluents, with the purpose of decreasing its acidity. This salt is precisely used to induce the precipitation of calcium sulphate – a slab of calcium carbonate is slowly dissolved in the effluent, that contains sulfuric acid, leading to the precipitation and deposition of calcium sulphate on the surface of the slab (Fusi, Primicerio and Monti 2015).

As mentioned previously, one of the materials used for the gaskets is PTFE, and, therefore, exhibits extremely low surface tension. This means that it cannot be wet by most liquids without a previous surface treatment (Holooly 2023). Calcium carbonate would have to be dissolved or mixed in a solution or binder that would adhere to the gaskets during the operation of the battery. Using a binder like PVDF, that is a fluorinated compound like PTFE, increases the probability of successfully placing calcium carbonate in the gaskets. PVDF needs to be dissolved in an appropriate solvent forming a solution that can be applied in the gasket – some

of the solvents that can be used are N,N-dimethyl acetamide (DMAC), dimethyl formamide (DMF) and N-methyl-2-pyrrolidone (NMP) (Kang and Cao 2014).

Crosslinking as a self-healing technique in VRFBs

Gaskets in VRFBs can also be made of PVC which has a higher surface tension than PTFE and, therefore, it is easier to find compounds compatible with this material. Purcar, et. al investigated the use of modified silica materials to synthesize hydrophobic and transparent coatings for PVC substrates. A silane compound was used as the silica source and was pre-hydrolysed using several silane precursors at room temperature. The resulting solutions were manually applied in the PVC substrates. The photopolymerization was initiated using an UV-lamp, and hydrophobic, transparent coatings were obtained (Purcar, et al. 2021).

The preparation of the silane solutions from the study mentioned above was achieved by inducing silane crosslinking reactions (Purcar, et al. 2021). Silane crosslinking occurs at room temperature when exposed to moisture or water, through a two-step process – first hydrolysis, and then condensation, as presented in Figure 2.2. In the first step, the methoxyl groups are hydrolysed to hydroxyl groups while methanol is released. In the second step, the recombination of hydroxyl groups takes place through a condensation reaction, releasing water (Bengtsson and Oksman 2006).

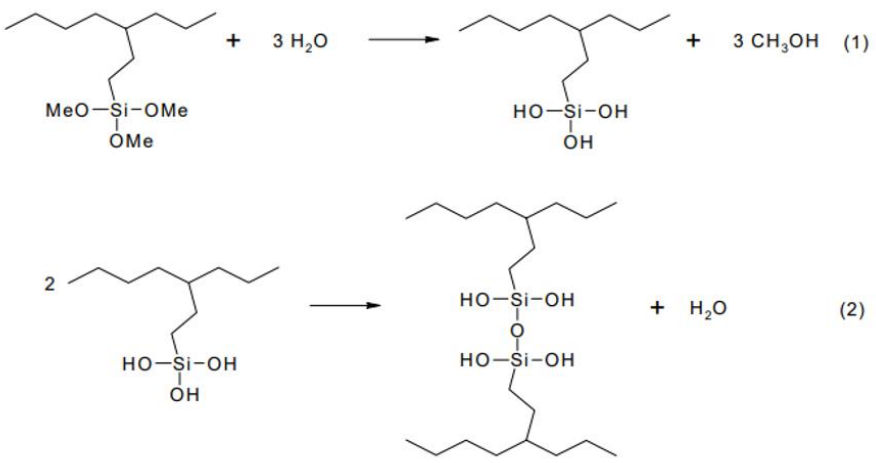

Figure 2.2 Hydrolysis (1) and condensation (2) steps during silane crosslinking (Bengtsson and Oksman 2006).

The methanol that would be released in the first step of the silane crosslinking can react with the available sulfuric acid and lead to the formation of methyl hydrogen sulphide (CH_3OSO_3H), according to the reactions described in the following equations – from (2.11) to (2.15).

$$H_2SO_4(aq) + H_2O(l) \rightleftharpoons HSO_4^-(aq) + H_3O^+(aq) \quad (2.11)$$

$$HSO_4^-(aq) + H_2O(l) \rightleftharpoons SO_4^{2-}(aq) + H_3O^+(aq) \quad (2.12)$$

$$CH_3OH(aq) + H_3O^+(aq) \rightleftharpoons CH_3OH_2^+(aq) + H_2O(l) \quad (2.13)$$

$$HSO_4^-(aq) + CH_3OH(aq) + H_3O^+(aq) \rightleftharpoons CH_3OSO_3H(aq) + 2H_2O(l) \quad (2.14)$$

$$CH_3OSO_3H(aq) + H_2O(l) \rightleftharpoons CH_3OSO_3^-(aq) + H_3O^+(aq) \quad (2.15)$$

The sulphate ester group $(-OSO_3H)$ has been found to chemically stable in the harsh environment of the electrolyte. A study on the use of acidic sulphate ester group for high conductivity membranes determined that, after immersing the membrane in 1.5 mol·L^{-1} VO_2^+ and 3 mol·L^{-1} H_2SO_4, acid or vanadium ions are more likely to attack polymer backbone rather than ion conductive groups. Therefore, it is unlikely that methyl hydrogen sulphide will react any further with the electrolyte (Van Loon and Allen 2004).

The behaviour of the crosslinking mechanism has been studied in acidic medium. Morin, et. al investigated the acid hydrolysis of MEMO ((3-methacryloxypropyl)trimethoxysilane) using HCl at room temperature. It was determined that, using a concentration of 0.1 mol·L^{-1} of HCl, most of the silane groups were hydrolysed in the first 10 minutes of reaction. The extent of the condensation reactions was, however, smaller, since no oligomers larger than octamers were detected (Morin, et al. 2004). Park and Kim performed the acid-catalysed hydrolysis and condensation of trimethoxysilanes using tetrahydrofuran as a solvent and HCl as the catalyst. After stirring for 3 min, precipitates were formed and analysed, revealing the formation of siloxane linkages (Park and Kim 2008).

Considering the acidic nature of the electrolyte, self-healing could be performed by inducing the hydrolysis and condensation of available silane groups. For these groups to be available to undergo crosslinking reactions, a silane terminated film needs to be synthesized to apply over the PVC substrate.

There are several types of silane-terminated compounds that can polymerize into a film to be applied in PVC – for example, epoxy silanes. Epoxy resins are widely used for their toughness, rigidity, temperature resistance, chemical resistance, and adhesive properties. Besides, these compounds can polymerize at room temperature and are easy to manipulate. The coupling mechanism of silane-terminated epoxy resins occurs as described in Figure 2.3 (Gelest, Inc. 2017). Generally, the amine nitrogen executes a nucleophilic attack on the terminal carbon of the epoxy group, involving the formation of intermediate complexes, ring-opening and proton transfer steps (Ran, et al. 2020).

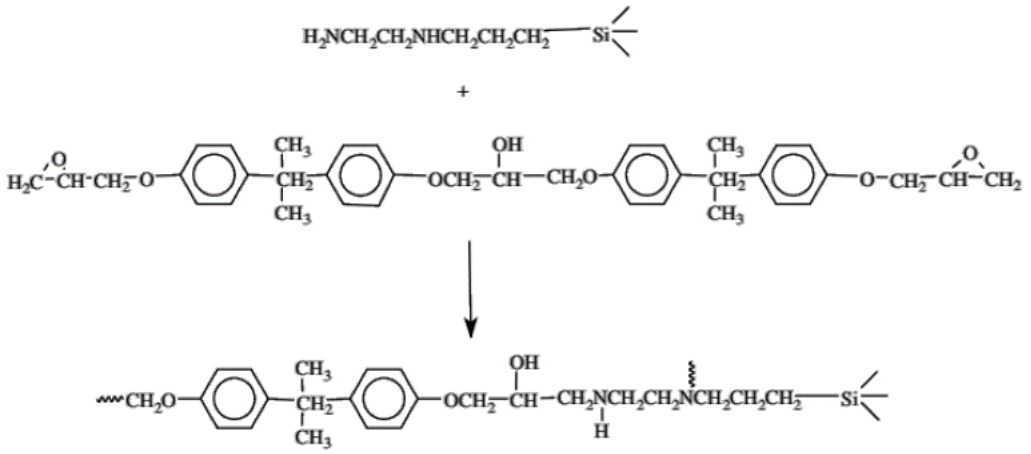

Figure 2.3 Scheme of epoxy-coupling reactions with silane-terminated compounds. Adapted from: (Gelest, Inc. 2017).

In conclusion, inducing the precipitation of sulphate salts by the application of calcium carbonate, or applying a film with silane-terminated compounds offer promising self-healing techniques for controlling electrolyte leakage in VRFBs. Calcium carbonate, with its higher solubility compared to calcium sulphate, can be mixed with a binder like PVDF to adhere to the gaskets and induce the precipitation of sulphate salts to obstruct possible leaks. While modified silane-terminated films can be applied to PVC substrates, providing hydrophobic coatings with self-healing properties. Epoxy silanes, known for their toughness and adhesive characteristics, offer a coupling mechanism for polymerization at room temperature, making an interesting alternative to synthesize silane-terminated films. Both these techniques hold potential for enhancing the reliability and performance of VRFBs by effectively addressing electrolyte leakage issues.

3 Materials and Methods

For the development of self-healing techniques for VRFBs, two methods were studied and tested, based on the research mentioned in the "Context and State of the art" chapter being the chosen methods the precipitation of calcium sulphate and silane crosslinking.

3.1. Precipitation as a self-healing technique

The main objective of this method is to trigger the precipitation reaction between calcium carbonate and sulfuric acid to seal the leak with the resulting salt – calcium sulphate.

Calcium carbonate needs to be deposited in the gaskets, to ensure its availability whenever an electrolyte leakage is detected. Due to the presence of fluorine atoms in PTFE gaskets, PVDF can be an appropriate binder to proceed with this technique. This binder needs to be firstly dissolved, so that the solution can be spread across the gasket.

The first step in testing this method is to find the optimum composition of the mixture, combining PVDF with NMP (the solvent) and calcium carbonate. The intended composition is to have the maximum amount of calcium carbonate available, while ensuring its proper application. Several compositions were tested, and evaluated regarding the mixing of all components, homogeneity, adherence to PTFE and the aspect of the dried film.

3.1.1 Determination of the optimum composition

In the application of the mixtures, the materials used were: closed glass vial with a magnetic bar, a magnetic agitator, a spatula, PTFE gasket, doctor blade, a graduated pipette and pompet, and, finally, personal protective equipment.

The procedure was the following for all the tested mixtures:

1. Weight the necessary amount of PVDF to a glass vial with a magnetic bar;
2. Add NMP with the graduated pipette and pompet to the glass vial;
3. Place the glass vial in the magnetic agitator, and mix at room temperature until complete dissolution of the PVDF;
4. Weight the necessary amount of calcium carbonate into a petri dish;
5. Slowly add the calcium carbonate while mixing the slurry at room temperature until obtaining a homogenous mixture.
6. In a clean gasket, apply the defined thickness of the slurry using the doctor blade and let it dry at room temperature for 1 to 2 days.

In Table 3.1, several compositions planned for testing are presented. The parameters modified between each mixture were the ratio between the mass of solids and mass of solvent, and/or

the percentages of calcium carbonate and PVDF. In Appendix A.1, it is explained how the values were calculated to determine the composition of each mixture.

Table 3.1 Planned mixtures to determine the optimum composition regarding applicability in the gasket and the amount of calcium carbonate.

ID	Composition					Solvent		
	$CaCO_3$ (%)	PVDF (%)	m_{total} (g)	m_{CaCO_3} (g)	m_{PVDF} (g)	m_{NMP} (g)	$\frac{m_{solids}}{m_{solvent}}$ (%)	V_{NMP} (mL)
1	95	5.0	1	0.0480	0.00250	0.100	50	0.0970
2	90	10	1	0.0900	0.0100	0.200	50	0.194
3	85	15	1	0.128	0.0225	0.300	50	0.291
4	50	50	1	0.250	0.250	0.667	75	0.647
5	50	50	1	0.250	0.250	0.833	60	0.809
6	70	30	1	0.210	0.0900	0.500	60	0.485
7	95	5.0	1	0.0480	0.00250	0.0830	60	0.0810

3.1.2 Observation of the interaction of the electrolyte with the film

After determining the compositions that displayed the best performance, the interaction between the electrolyte and the dried film after applied in the gasket must be studied. For these tests, the materials used were: PTFE gaskets covered with calcium carbonate film, a micropipette and a commercial vanadium electrolyte with the following specifications: 1.6 mol·L^{-1} of V^{3+}/V^{4+} and 2 mol·L^{-1} of H_2SO_4 in water with 0.05 mol·L^{-1} of H_3PO_4 as an additive.

One of the mixtures was ID6 - two drops of electrolyte that composed a total volume of 200 µL were applied in the gaskets covered with this film, and the gaskets were placed vertically to spread the electrolyte. The other mixture was ID7 - only one drop of 20 µL was applied. For the latter, the remaining solids were taken for analysis using FTIR to determine their composition.

The FTIR analysis consisted in the observing the transmittance of the samples in a predefined range of wavenumber (cm^{-1}) – from 350 to 4000 cm^{-1}. The peaks obtained were then analysed and attributed to the most suitable vibration and molecule.

3.1.3 Testing the self-healing properties of the film

To perform the tests, a set-up similar to the one presented in Figure 2.1 was used. Since the objective was just to keep the electrolyte in circulation and evaluate the stability of the film, there was no membrane and only one electrode was used for these experiments, as it is presented in Figure 3.1. To induce a leak in the cell, a gasket was cut, forcing the electrolyte loss. In Figure 3.1, this gasket is represented by number 7, and in Figure 3.2 two images of gaskets used in these tests are presented. The electrolyte entered and exited through the same side of the set-up, flowing through the gaskets and the electrode. The number of gaskets was

the necessary to make up a thickness of 3.5 cm (including the thickness of the film), to ensure the necessary compression of the electrode.

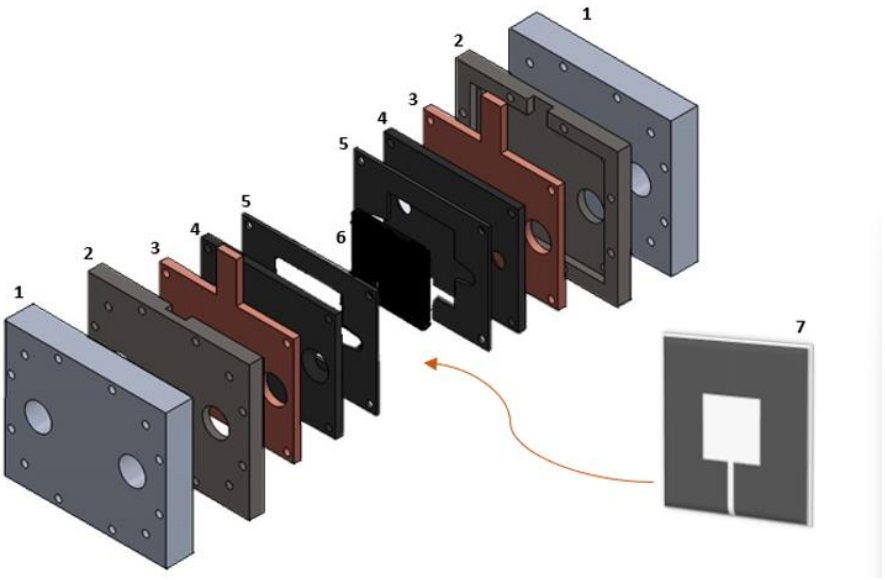

1 – Aluminium case
2 – Plastic case
3 – Current collector
4 – Bipolar plate
5 – Gasket/Flow field
6 – Electrode
7 – Cut gasket to simulate the leak

Figure 3.1. Schematic representation of the half-cell used to perform the tests. Adapted from: (Iwakiri, et al. 2021).

Figure 3.2 Image of two of the gaskets cut to simulate the leak of electrolyte for (a) the electrode of 25 cm^2, and (b) 4 cm^2.

For all the tests, the cell was assembled firstly without any film, and, for different flowrates defined for circulating the electrolyte, the flowrate in the cut area was measured using a graduated beaker and a timer.

The materials needed for this were: the half-cell components, one pump to circulate the electrolyte solution; an electrolyte solution with 1.6 mol·L^{-1} of V^{3+}/V^{4+} and 2 mol·L^{-1} of H_2SO_4 in water with 0.05 mol·L^{-1} of H_3PO_4 as an additive; a graduated beaker and a timer.

Some conditions were changed throughout these tests: the length of the film and the width of the leak. The length of the film was modified by changing the electrode area – for the same cell, a gasket for a smaller electrode provides a wider area to apply the film, or by changing the scheme of application. These alterations allowed to determine the amount of film required to seal the leak properly. The width of the leak was altered by changing the width of the cut and allowed to observe the success of this technique for different leakage flowrates. Table 3.2 presents the different characteristics of the gaskets tested to simulate the leak. The electrolyte flowrates were defined by measuring the leakage flowrate, since these depend on the gasket used (mainly on the width of the cut) and determining whether it was representative of a realistic leak.

Table 3.2 Characteristics of the different gaskets tested to simulate the leak and electrolyte flowrates used to measure the leak flowrate.

Gasket	Electrode area (cm^2)	Width of the cut (mm)	Cross-sectional area of the leak (mm^2)	Electrolyte flowrates tested (mL·min^{-1})
1	25	1	0.5	5 10 15 25 30
2	25	0.5	0.25	15 20 25 30 35
3	4	0.5	0.25	180 200 220 230 241

3.2. Crosslinking as a self-healing technique

The aim of this technique is to create an active physical barrier by incorporating silane-terminated monomers in an epoxy resin. The objective is that the hydrophobic characteristics of the epoxy resin, in combination with the hydrolysis and condensation of the accessible silane groups, prevent the loss of electrolyte by forming a stable and polymerized structure around the cell.

An epoxy resin is a two-component material, usually by combination of epoxy-terminated monomers (component B) with amine-terminated ones (component A). Therefore, the integration of silane groups should be easier by using epoxy-silane and amino-silane compounds: 3-(Aminopropyl)dimethylmethoxysilane (AS) is the amine-terminated silane and Methoxy-dimethyl-(oxiran-2-ylmethyl)silane (ES) is the epoxy-terminated silane.

The incorporation of these monomers was studied to determine the optimal composition of the epoxy resin – it should adhere to the gaskets, while providing a stable barrier to keep the electrolyte from leaking. The gaskets are made of PVC due to the better adhesion of epoxy resin to this material, when compared to the PTFE gaskets.

The synthesized resins were analysed through FTIR to study the changes in the chemical structure after the incorporation of silanes, and their contact with the electrolyte.

3.2.1 Synthesis of the epoxy-silane resins

The incorporation of the silane monomers was tested firstly on component A, then on component B, and lastly on both components. This substitution needs to consider the epoxy/amine ratio of the standard epoxy resin, so as not to interfere with its characteristics and curing process.

The reagents to prepare the resins were:

- Primer Epóxi Fetadit PA-47 - two component epoxy resin from Castro Composites, where component A contains the amine groups while component B contains the epoxy groups;
- Pure 3-(Aminopropyl)dimethylmethoxysilane – AS;
- Pure Methoxy-dimethyl-(oxiran-2-ylmethyl)silane – ES.

The materials needed were: spatulas, a magnetic agitator and magnetic bar, a micropipette (range from 50 to 2000 µL), a weighing scale, a glass flask and paraffin film (to keep the silanes protected from humidity), a hotte and personal protective equipment;

In Table 3.3, the composition of the resins studied in each experiment is specified. In Appendix B.1, the determination of the mass of each component is explained, taking into account the ratio of epoxy/amine groups. The total mass of the resin was defined according to the dimensions of the PVC plates and the intended area of application of the film.

Table 3.3 Composition of the resins in each experiment.

Test	Silane incorporation	Component A (g)	Component B (g)	AS (g)	ES (g)
0	---	2.19	0.690	---	---
1	10% AS	1.97	1.61	0.219	---
2	30% AS	1.53	3.46	0.657	---
3	50% AS	1.09	5.31	1.09	---
4	10% ES	2.47	0.620	---	0.0691
5	30% ES	3.03	0.480	---	0.207
6	50% ES	3.59	0.350	---	0.346
7	10% AS 41% ES	1.97	0.622	0.219	0.435
8	30% AS 73% ES	1.53	0.484	0.657	1.305
9	50% AS 86% ES	1.09	0.346	1.09	2.17

The general procedure for the preparation of the resins was the following (it was adapted to the reagents used in each experiment):

1. Weight the mass of component B to a glass flask with a magnetic bar;
2. Weight the mass of ES to the flask with component B and cover it with paraffin film;
3. Mix component B with ES until it is homogeneous;
4. Weight the mass of component A to another glass flask;
5. Weight the mass of AS to the flask with component A and cover it with paraffin film;
6. Mix component A and AS until it is homogeneous;
7. Add the mixture of component A and AS to the mixture of component B and ES and let it agitate until a homogeneous mixture is obtained.

3.2.2 Application of the epoxy-silane film

The objective was to study the influence of the incorporation of silanes in the adhesion of the resin to PVC substrates, and to study the interaction of the film with the electrolyte. Therefore, to perform these tests, the following materials were used: vanadium electrolyte solution with 1.6 mol·L^{-1} of V^{3+}/V^{4+} and 2 mol·L^{-1} of H_2SO_4 in water with 0.05 mol·L^{-1} of H_3PO_4 as an additive; PVC plates set-up as in Figure 3.2 – three plates put together with approximately the same length and width, with the middle plate cut in half, leaving a path of around 0.5 mm for the insertion of the electrolyte; spatula; support for the PVC plates; micropipette (range from 50 to 2000 µL); hotte; personal protective equipment.

In Figure 3.3, the setup of the experiments is presented – all the plates have approximately $10 \times 10 \times 0.4$ cm, and the middle plate has a vertical cut with approximately 0.5 mm of width.

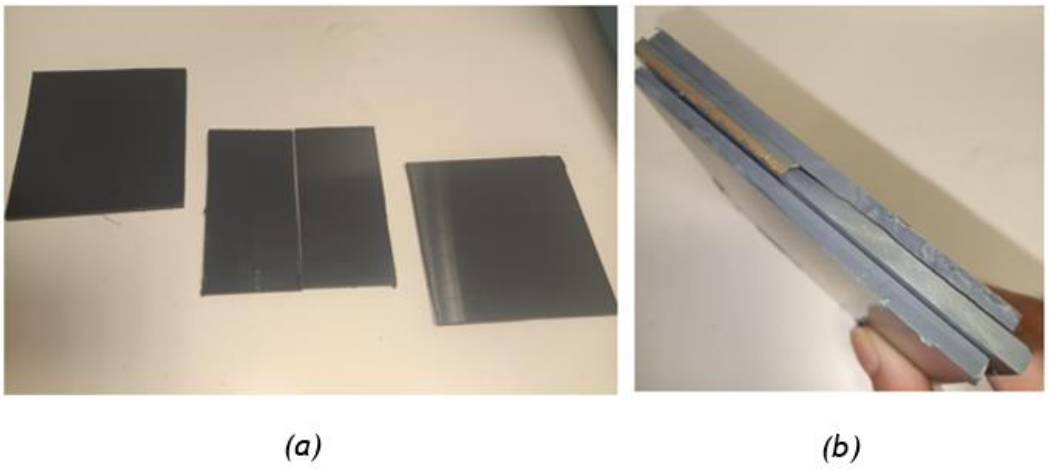

(a) (b)

Figure 3.3 Setup for the experiments with the PVC plates (a) size and shape of each plate, (b) assembly of the plates.

The application of the film was executed with a spatula, covering the whole base of the test setup. Care was taken to ensure that the cut of the middle plate was covered with resin. The plates were placed with the setup upside-down, to ensure a good adhesion of the resin to the PVC substrate. The curing process before the interaction with the electrolyte took approximately 24 hours. After this, the electrolyte was introduced in the path between the middle plates using a micropipette (about 2 mL were introduced). The ability of the resin to keep the electrolyte within the cell was observed, and after 1 hour, the resin samples were analysed through FTIR to determine the structure of each one.

3.3. EIS measurements

Electrochemical Impedance Spectroscopy (EIS) allows to determine voltage loss within a cell due to ohmic and non-ohmic contributions, which include adsorption processes, charge and mass transfer resistances and are time/frequency dependant. Impedance is therefore the ratio between the time-dependant voltage and time-dependant current. The results are the represented through a Nyquist plot - the imaginary part of the impedance as a function of the real part. These measurements can be performed under potentiostatic or galvanostatic mode. In potentiostatic mode, the amplitude of the measurements should be between 5 mV to 50 mV to maintain the linearity of the response, while separating the noise from the measurements. The frequency range is typically between 1 mHz and 100 kHz (Pinto, Oliveira and Falcão 2018).

This study was performed in a full cell to investigate the influence of the application of the calcium carbonate film in the resistance of the cell. From the experiments, it is possible to retrieve the ohmic resistance (R_Ω) and the charge-transfer resistance (R_{CT}) through the

intercept of the curve with horizontal axis and the diameter of the flattened semi-circle in low frequency region, respectively (Mazur, et al. 2019).

Figure 3.4 presents the full cell assembled, for this experiment a Zahner potentiostat was connected to the current collectors, and the measurements were followed using a Thales software.

There was a nafion membrane separating the two half-cells, and each half was constituted by (starting from the centre of the cell): one gasket of 0.5 mm, 0.5 mm of film, another 0.5 mm gasket, another 0.5 mm of film, another 0.5 mm gasket, one flowfield with 1 mm, graphite plate, current collector, rubber sealants and the endplates. To perform the test without the film, one gasket of 1 mm was added between the graphite plate and the flowfield in each side of the cell. The characteristics of the electrolyte are the same used for the other procedures in this document. The characteristics of the measurements are described in Table 3.4.

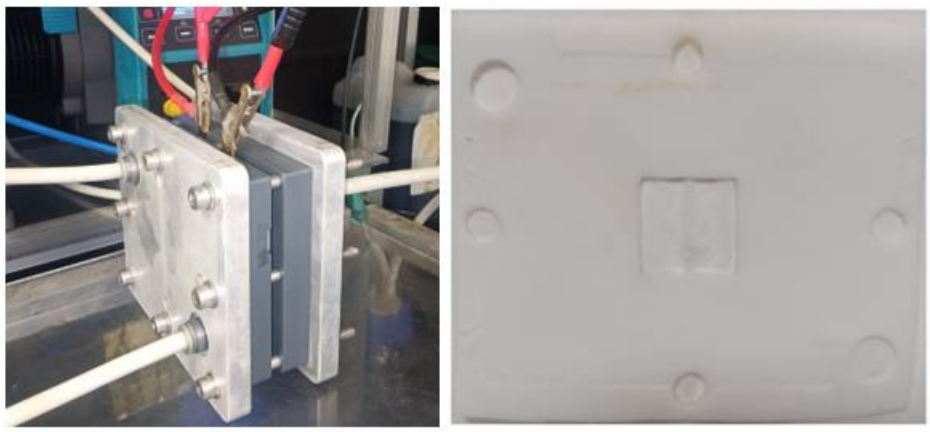

Figure 3.4 Full cell assembled for the EIS measurements (a) and scheme of application of the test with the film (b).

Table 3.4 Parameters of the EIS measurements.

Parameters	Test 1 (with film)	Test 2 (standard cell)
Volume of electrolyte (mL)	80 (positive side) and 60 (negative side)	80 (positive side) and 60 (negative side)
Electrolyte flowrate ($mL \cdot min^{-1}$)	50	50
Open circuit voltage (V)	1.312	1.312
Amplitude of measurements (V)	0.005	0.005
Frequency range (Hz)	0.010 to 100000	0.010 to 100000
Starting frequency (Hz)	100000	100000

4 Results and Discussion

In this chapter, the obtained results are presented and their relevance is discussed for the feasibility of the investigated techniques.

4.1. Application of the calcium carbonate film

Regarding the compositions presented in Table 3.1, the first to be formulated was ID2. The application in the gasket was not possible since there was no adhesion between the gasket and the mixture due to the low surface tension of PTFE, already mentioned in the chapter regarding the Context and State of the art. After this observation, it was decided that ID1 and ID3 would not be viable for application, since the solid/solvent ratio was the same as ID2. To make the application possible, the viscosity of the slurry had to be increased, as well as the surface energy of the gasket. For this to happen, an abrasive paper was used to polish the gasket, promoting surface roughness.

The following formulations were already applied in polished gaskets. Regarding ID4, the dissolution process of PVDF in NMP required a significant amount of time for the PVDF to dissolve completely. Additionally, achieving a proper mixture with calcium carbonate was impossible, there was no homogeneous slurry. Consequently, this formulation could not be applied in the gasket. For ID5, in comparison to ID4, the dissolution of PVDF in NMP was relatively easier due to the lower solid content. However, the incorporation of calcium carbonate into the solution was also problematic, leading to the absence of a homogeneous mixture. As a result, this formulation was also unsuitable for application in the gasket.

ID6, on the other hand, presented better results. The decrease in the amount of PVDF allowed for an easier dissolution in NMP. The mixing of calcium carbonate in the solution was also successful, leading to a homogeneous slurry. The slurry was applied both in a polished gasket and in a non-polished gasket. The application was more successful in the polished gasket and the film appeared to be more uniform. In Figure 4.1 can be seen images of the application of this formulation before and after drying.

(a) (b)

Figure 4.1 Film ID6: (a) right after application in the polished (left) and non-polished (right) gasket; and (b) after drying in the polished (left) and non-polished (right) gasket.

Finally, ID7 allowed to obtain a higher concentration of calcium carbonate, which should enhance the precipitation of calcium sulphate when in contact with the electrolyte. PVDF dissolved in NMP, resulting in a homogeneous solution. The addition of calcium carbonate was also successful since the particles blended with the solution. However, calcium carbonate since demonstrated the tendency to set at the bottom of the glass vial and a supernatant liquid that should be the PVDF dissolved in NMP. Therefore, for the film to be as homogeneous as possible, the slurry was kept in high agitation until the moment of application.

The compositions ID6 and ID7 were selected to test their interaction with the electrolyte, since they presented better results. For the film of the mixture ID6, two drops of a total volume of 200 µL of electrolyte were applied in a film with a thickness of 200 µm. In Figure 4.2, the results observed are presented.

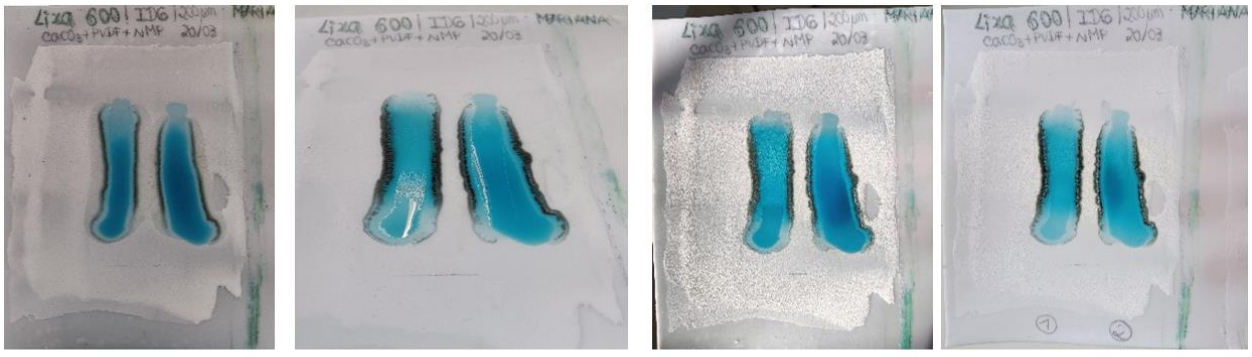

(a) (b) (c) (d)

Figure 4.2 Interaction of 200 µL of electrolyte (distributed in two different drops) with the ID6 applied in the polished gasket. Photos taken: (a) right after application, (b) 1h after the application, (c) 2h after the application and (d) the next day.

Right after the application, Figure 4.2 (a), there is the formation of a black solid particles in the limit of the area covered by the electrolyte. The area near the limit appears to have a

lighter blue/white precipitate. After 1 h of application, Figure 4.2 (b), the drop on the left presents half of the area solidified, being a major part covered by blue particles. The other drop still presents a large part of the area with liquid electrolyte. It can be seen in the other two photos that there are no significant changes. The volume of liquid electrolyte decreases slowly with time, presenting an increase in the amount of solid particles. The slow pace of solidification can be due to the quantity of electrolyte applied, so the amount of electrolyte should be decreased.

For the film with the solution ID7, only one drop with 20 µL was applied in a film with 200 µm. In Figure 4.3 the interaction of the electrolyte with this film is presented.

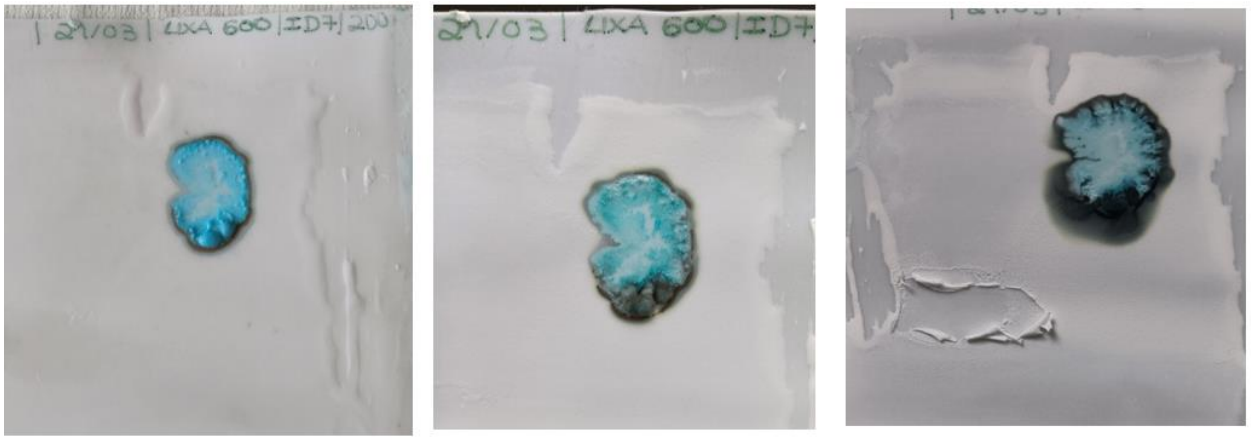

(a) (b) (c)

Figure 4.3 Interaction of 20 µL of electrolyte with the ID7 applied in the polished gasket. Photos taken: (a) right after application, (b) 90 min after the application and (c) the next day.

Right after the application, Figure 4.3 (a), it is observed the formation of solid particles, and there is no liquid electrolyte left. As observed for ID6, the limit of the area covered by the electrolyte presents black solid particles from the beginning. However, there is no light blue area observed near the limits. It can also be noted the formation of bubbles of several sizes, near the limit, with an intense blue coloration. The centre of the area presented a white coloration. After 90 min of the application of the electrolyte, the amount of black particles increases, the largest bubbles, initially blue, present now a black coloration, and the white precipitate in the centre of the area is more evident. In the next day, there is an expansion of the black precipitate area and most of the area initially occupied by blue solid particles is now occupied by white particles. To conclude, the solidification was much faster by decreasing the amount of electrolyte. These precipitates were taken for analysis through FTIR – the spectra obtained are presented in Appendix A.1.

For the sample of the calcium carbonate and PVDF film, the spectrum can be seen in Figure A.1, Appendix A.1. The presence of carbonate ions is marked by the peak at 711 cm^{-1} (Nyquist

and Kagel 1971). The structure of PVDF is evidenced by the C-H bending and wagging vibration at 871 and 1400 cm^{-1} (InstaNano 2023). The peaks at 1400 and 1074 cm^{-1} are also associated with CC asymmetric stretch, from the structure of PVDF (Peng, Sun and Wu 2008). Lastly, at 1182 cm^{-1} it can be seen the stretching of C-F bonds from PVDF and C-O from calcium carbonate.

The FTIR spectrum of the electrolyte after precipitation is presented in Figure A.2, in Appendix A.1. The C-F and C-O bonds visualized in Figure A.1, are also present in the spectrum of Figure A.2, at 1097 cm^{-1}. The stretching vibration of C=O is marked at 2343 cm^{-1}, and at 867 cm^{-1}, the CC symmetric stretch, along with CCC bending from the PVDF chain, and CF_2 symmetric stretch are evidenced (InstaNano 2023). Regarding the precipitation of vanadium oxides and hydroxides, along with other sulphate salts – O-H bending and stretching is presented in 1621, 3405 and 3529 cm^{-1}; SO_4 stretching is evidenced at 466, 663, and 1405 cm^{-1}, and, lastly, V-O bonds are represented at 590, 663 and 985 cm^{-1}. Combining these results with the colours of precipitates observed, it is possible that the solids are composed of $V_2(SO_4)_3$ in sky blue and VSO_4 in the darkest colour (Carvalho Jr, et al. 2021). The SO_4 stretching vibration should also be provoked by the precipitation of calcium sulphate.

To study the self-healing properties of the film with an electrolyte solution in circulation, the composition ID7 was firstly applied in gasket 1, composing a film with a thickness of 300 µm. The leakage flowrate was successfully reduced to half, when compared to the flowrate measured without the film (measured flowrate values can be found in Appendix A.2). However, it was not sealed - as it can be seen in Figure 4.4, the film applied in the area of the cut was removed with the running electrolyte, not having enough time to precipitate and cover the leak. It was decided not to pursue the tests for the other flowrates since the leakage flowrate would be higher and, therefore, the film would not be enough to prevent the loss of electrolyte. It can also be seen the formation of precipitates in that area, suggesting that the reaction with the film occurred, as previously observed in Figures 4.2 and 4.3.

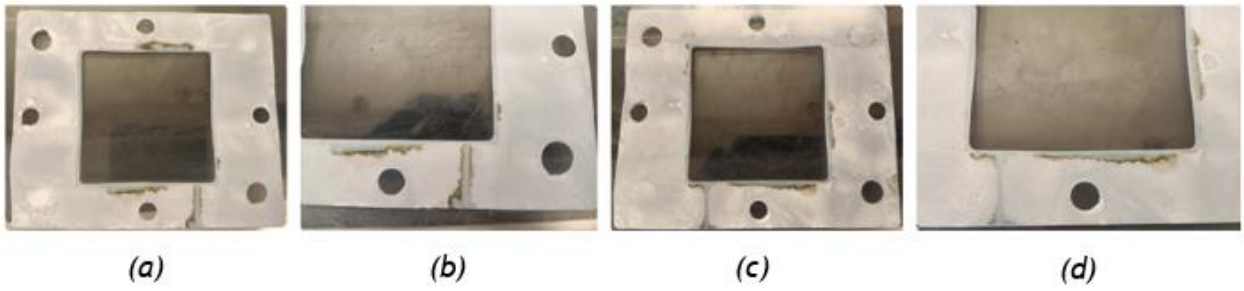

Figure 4.4 PTFE gaskets with ID7 film of 300 µm after the experiment with gasket 1 - (a) and (b) are images from one of the gaskets and (c) and (d) are from the other.

The formation of precipitates around the electrode suggests that there could be contamination of the circulating electrolyte, which could damage the performance of the cell in long term operation.

In the experiments with gasket 2, none of the films applied were able to seal the leak, even though the width of the cut in this gasket was smaller, suggesting that it should be possible to prevent or decrease the loss of electrolyte. All the experiments were executed using a film thickness of 500 µm. Comparing to the thickness of 300 µm used for gasket 1, it would be expected that the precipitation would be more effective, since there is more calcium carbonate available. However, it seems to have the opposite effect - the thickness of the film may be unevenly distributed throughout the gasket, exacerbating the loss of electrolyte, instead of solving the problem. The flowrate measured for gasket 2 and the registered photos from the tests can be consulted in Appendix A.3. The first test applied a flowrate of 15 $mL \cdot min^{-1}$, and, since the loss of electrolyte was exacerbated with the application of the method, the following experiments were performed for 5 $mL \cdot min^{-1}$. This flowrate is below the range of flowrates defined for gasket 2 when measuring the leakage flowrate without the film, however, the tests presented the same outcome as the first experiment. The scheme of application of the film was modified in one of the experiments with gasket 2 to prevent the possible contamination of the circulating electrolyte – it was applied leaving a margin around the electrode. The objective was to limit the film to the area that is under more pressure due to the assembly of the cell, to minimize the difference of thickness between the areas with and without the film. In Figure 4.5 this scheme is represented before and after the test (Figure 4.5 (a) and Figure 4.5 (b) and (c), respectively).

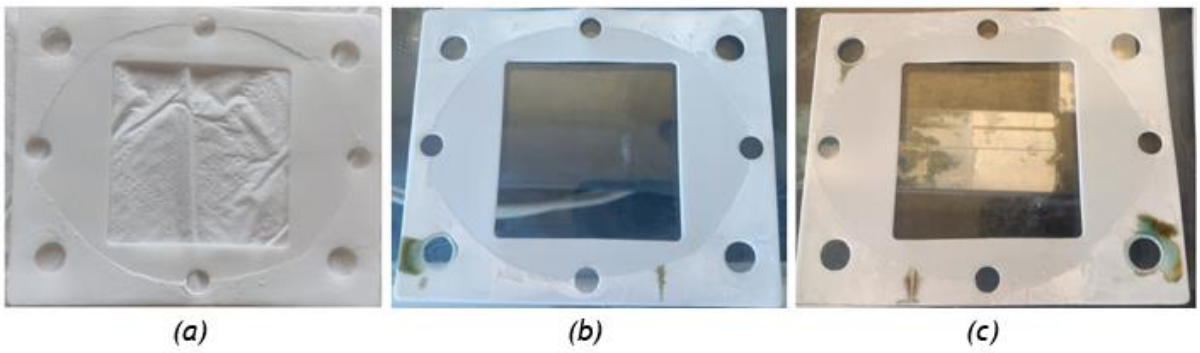

Figure 4.5 PTFE gaskets with a 300 µm film of ID7 - (a) scheme applied; (b) and (c) gaskets with the film after the experiment with gasket 3.

This application allowed to maintain the electrolyte leaking only through the area of the cut – there is no precipitation around the electrode area. However, as stated for the other experiments with gasket 2, the film was dissolved by the electrolyte, and so there was not

enough contact time between the film and the electrolyte to induce precipitation and obstruct the leak.

In gasket 3 the electrode area is smaller, meaning that the gaskets for this electrode provided a wider area for the application of the film. Therefore, satisfactory results are expected regarding its ability to seal the leak, when comparing to the gaskets of the largest electrode. The results of the flowrate measurements are presented in Appendix A.4. The first experiment was performed by applying the film in the whole gasket, not leaving a margin around the electrode, to maximize the amount of calcium carbonate available. It was determined that, for 180 $mL \cdot min^{-1}$, the electrolyte was able to circulate for 1 hour without significant loss – only one drop of electrolyte was observed, after 49 minutes of test. This positive result indicates that the wider area of these gaskets might be enough to control electrolyte leakages when the electrolyte is circulating at 180 $mL \cdot min^{-1}$. After 30 minutes of operation a drop of electrolyte was observed, in the entrance of electrolyte on the half-cell – this leak could be associated with a faulty assembly of the cell. The photographic registration of the gaskets with the film ID7 after the first experiment are provided in Figure 4.6. As expected, since there was no margin left in the centre of the gasket, precipitation occurred around the electrode due to the contact between the film and the circulating electrolyte.

Figure 4.6 PTFE gaskets with the film after the first experiment with gasket 3 - (a) is from one of the gaskets and (b) is from the other.

To prevent the possible contamination of the electrode, a different scheme of the film was applied in the gaskets for the smaller electrode, as previously tested in Figure 4.5. This scheme intended to limit the film to the area that is under more pressure when the cell is assembled. The experiment was also performed for a flowrate of 180 $mL \cdot min^{-1}$, and there was no registration of electrolyte loss through the area of the cut in gasket 3. However, as registered for the experiment associated with Figure 4.6, other leaks were observed – the electrolyte leaked through centred holes of the endplate. This can be associated with a flawed assembly of the cell. Figure 4.7 presents the registered images of the scheme applied and the results after the experiment. It can be determined that, even though it is possible to prevent

electrolyte loss with a smaller gasket area covered with the film, the electrolyte is leaking through the whole gasket, instead of only flowing through the cut in gasket 3.

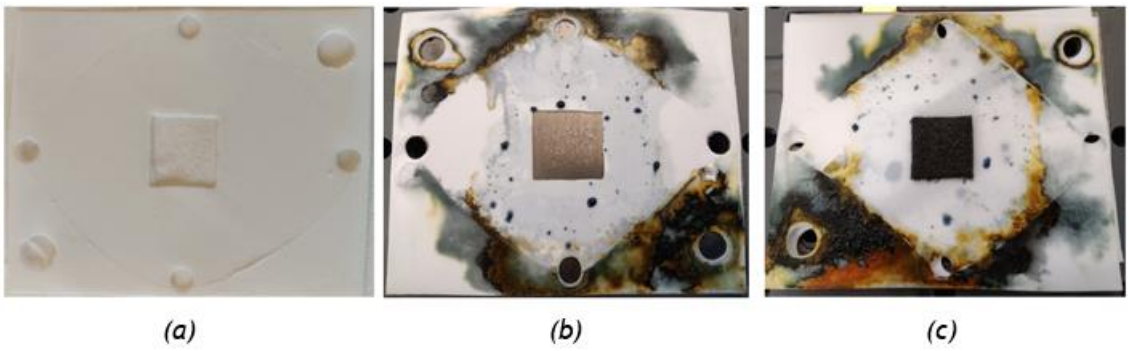

Figure 4.7 PTFE gaskets with a 500 µm film of ID7 applied with a different scheme - (a) scheme applied; (b)and (c) gaskets with the film after the experiment with gasket 3.

Another scheme was experimented, by limiting the area covered by the film closer to the pressured points in the gasket. It was also taken into consideration that there should not be calcium carbonate around the holes of entrance and exit of the electrolyte, so as not to contaminate the solution. In Figure 4.8, the scheme applied and the results after the experiments are presented. The test was performed for a flowrate of 180 $mL \cdot min^{-1}$, and the leak was effectively sealed. The same leak registered for the experiment of Figure 4.5 in the centred holes of the endplate was observed. It was determined that reducing the area of application of the electrolyte effectively reduced the electrolyte leakage through paths other than the cut in gasket 3. However, the width of the film should be reduced, so that the thickness increase caused by the application of the film does not exacerbate the loss of electrolyte.

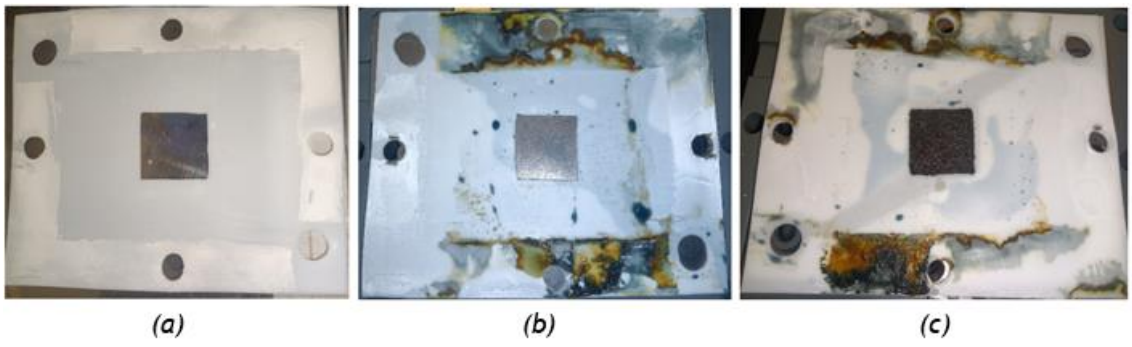

Figure 4.8 PTFE gaskets with a 500 µm film of ID7 applied with a different scheme - (a) scheme applied; (b) and (c) gaskets with the film after the experiment with gasket 3.

The scheme of application of Figure 4.8 (a) was repeated, and the results of these experiments can be seen in Appendix A.4. Among these tests, the width of the film applied was changed to successfully prevent the loss of electrolyte while restraining the electrolyte leakage to the area of the cut. The most promising result obtained is presented in Figure 4.9 – the scheme of application can be seen in Figure 4.9 (a), and the photos of the gaskets after the test for a

flowrate of 180 mL·min^{-1} are given in Figure 4.9 (b) and (c). There is still precipitation in both the upper and lower side of the gasket, meaning that the width reduction was not enough, even though the loss of electrolyte was effectively prevented.

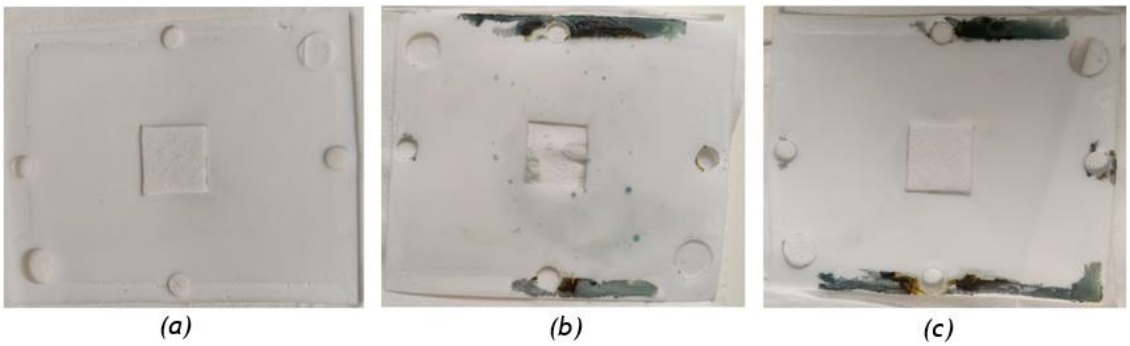

Figure 4.9 PTFE gaskets with a 500 µm film of ID7 applied with a different scheme - (a) scheme applied; (b) and (c) gaskets with the film after the experiment with gasket 3.

From the study of the effectiveness of calcium carbonate film as a self-healing technique, it can be concluded that this precipitation mechanism can be a viable option prevent the loss of electrolyte due to electrolyte leakage during operation of the cell, for a flowrate of 180 mL·min^{-1}. However, a different approach should be investigated. It is possible that the additional thickness of the film is creating a pathway between different gaskets for the electrolyte to flow through, worsening the problem that is being investigated.

4.2. Application of the epoxy-silane resin

Testing the application of a silane-terminated epoxy resin started with the preparation of the mixtures displayed in Table 3.3. The experimental values of each test are presented in Appendix B.2.

Test 0 consisted of the standard epoxy resin, with no modification in any of the components. Both the preparation and application of the film were easily performed, and the film presented good adhesion to the PVC substrate. In Figure 4.10 (a) an image of the mixture inside the glass flask is presented, and in Figure 4.10 (b) the film after 1 day of curing can be seen. The consistency presented in Figure 4.10 (a) was obtained with around 15-20 min of aggitation.

Figure 4.10 Image of the standard epoxy resin after the mixing of both components (a), and after the application and curing of the film (b).

Tests 1 to 3 investigated the incorporation of AS in component A. It was determined that the addition of AS influenced the homogeneity of the resin since it was not possible to mix these two components properly. In Figure 4.10 is presented the mixture of component A and AS after agitation for 30 min, for test 1 – the intensity of the yellow color characteristic of the resin is not evenly distributed. It should be noted that for this test, the concentration of AS is not 10%, as planned, but instead 14%. The amount of component B was adjusted to maintain the epoxy/amine ratio.

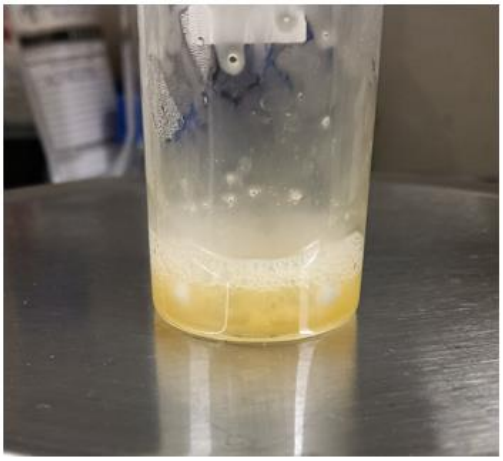

Figure 4.11 Image of component A and AS (14 %) after agitation for 30 min, for the preparation of test 1.

Due to this lack of homogeneity, after the addition of component B to the mixture in Figure 4.11, the resin did not present the same results as seen for the standard version for test 1 (14% AS) – a supernatant phase was observed, and so, the final mixture was not also properly homogeneous. The resulting film after 1 day of curing can be seen in Figure 4.12. It was possible to effectively cover the cut in the setup for test 1. The resin passed through the cut, and filled the pathway designed for the introduction of the electrolyte, so it was difficult to insert the electrolyte between the plates and ensure contact with the resin. The electrolyte was in

contact with the resin for an hour and no leaks were registered, indicating that the resin is capable of containing the electrolyte.

Figure 4.12 Film from test 1 applied in the PVC substrate, covering the cut executed in the middle plate.

The increase in the concentration of AS in component A resulted in more homogeneous mixtures of these two components, as it was observed for tests 2 (30% AS) and 3 (50% AS). In these tests, the introduction of the electrolyte in the cut was not a problem, since the resin did not obstruct the path. As it was determined in test 1 (14% AS), the resin is capable of containing the electrolyte since test 2 (30% AS) did not present leaks through the cut – the only leaks observed were through the sides of the plates, that were not covered with film. On the other hand, the film in test 3 (50% AS) did not cover the cut – the combination of the width of the cut and the thickness of the film could have originated this phenomenon. The resin could not create a barrier and the electrolyte was not contained in between the PVC plates. The thickness of the film was not enough to maintain the film intact during the curing time necessary to form a barrier – this could be due to a flawed assembly of the test setup, due to the application of an insufficient amount of resin in that area or even physical properties of the resin, like viscosity or rate of curing for example. If the viscosity is not high enough, the resin wil flow through the cut and might not create an uniform film. If the curing rate is slower, than film will be less viscous for a longer time, decreasing its stability to endure the necessary time without flowing through the plates. Despite these results, the electrolyte was inserted and contacted with resin in other parts of the setup of the test.

Tests 4 (10% ES) to 6 (50% ES) investigated the incorporation of ES in component B. Mixing these two components was easier than mixing AS and component A, and homogeneous solutions were obtained. Consequently, the resin obtained had a similar aspect to the standard version, as it can be seen in Figure 4.13 - resin of test 5 (30% ES) before (a) and after (b) the application of the film.

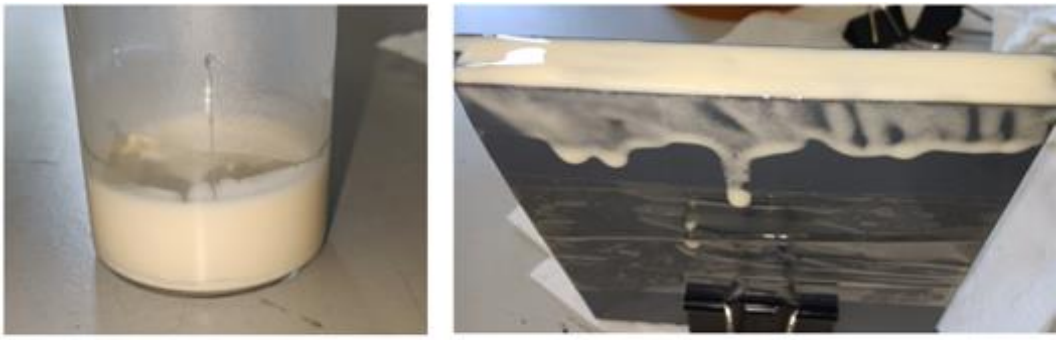

Figure 4.13 Resin of test 5 (30% ES) before (a) and after (b) the application of the film in the PVC plates.

In Figure 4.14 images of the resin of tests 5 (30% ES) and 6 (50% ES) after 1 day of curing are presented. It can be seen that it was possible to create a barrier, and effectively cover the cut. On the other hand, test 4 (10% ES) had the same outcome of test 3 (50% AS).

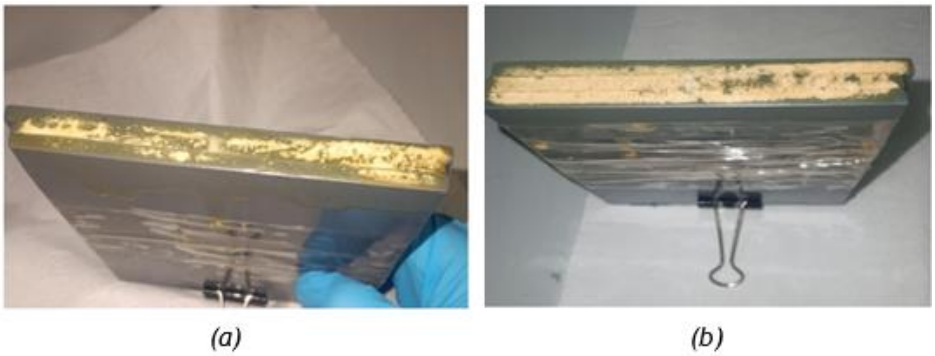

Figure 4.14 Films of tests 5 (30% ES) and 6 (50% ES) after curing for 1 day and before the introduction of the electrolyte.

The interaction of the electrolyte did not present positive results for test 4 (10% ES), as expected, since the cut was not covered. For these tests, the electrolyte was in contact with the resin for more than 1 hour (around 2 to 3 hours), to evaluate if it would increase the differences in the FTIR spectra between the resin without contacting with the electrolyte and the resin that contacted with it. Tests 5 (30% ES) and 6 (50% ES) were able to contain the electrolyte within the PVC plates. Similarly to test 2 (30% AS), test 5 (30% ES) only presented leaks through areas that were not covered with the resin. This means that the resin can connect different plates, creating a uniform surface, even when they are not under compression forces

as high as the ones applied in the cell assembly. Therefore, the application of the film around PVC gaskets in a stack should create a uniform barrier without gaps, unlike tests 3 (50% AS) and 4 (10% ES). The resin in test 6 (50% ES) flowed through the cut during the curing process, and so, the introduction of the electrolyte in the gap was difficult, as was the case for test 1 (10% AS). This could mean that the viscosity of these resins was lower, when compared to other tests, or that there was a flawed assembly of the tests, resulting in a larger gap.

In the last set of tests – the combination of the incorporation of both AS and ES in the resin formulation, the incorporation of AS was executed in the same way as for tests 1 (14% AS) to 3 (50% AS). However, the corresponding amount of epoxy groups was not provided by component B, it was assured by the addition of the necessary amount of ES. Since for 1 amine group of AS, 2 epoxy groups from ES were necessary, the percentage of ES in the component B of the mixture was much higher than the percentage of component AS.

Test 7 (10% AS, 41% ES) displayed the same behaviour as observed in test one in the mixing of components AS and A – the composition was 14% of AS and 86% of component A. Nonetheless, the addition of the solution of ES and component B allowed to obtain an apparently homogeneous resin. The mixture with all the components was agitated for 15 minutes, and it was determined that it was an excessive amount of time – close to the end of the agitation, the viscosity increased, and the component presented a gelatinous texture. This outcome made the uniform application of the film impossible, which affected the adhesion of the resin to the PVC substrate and its ability to prevent the loss of electrolyte. Figure 4.15 presents the result right after the application of the gelatinous film in the PVC plates, (a) and (b), and after 1 day of cure, (c), – the resin did not spread across the area of application, and so, the contact area between the substrate and the film was reduced.

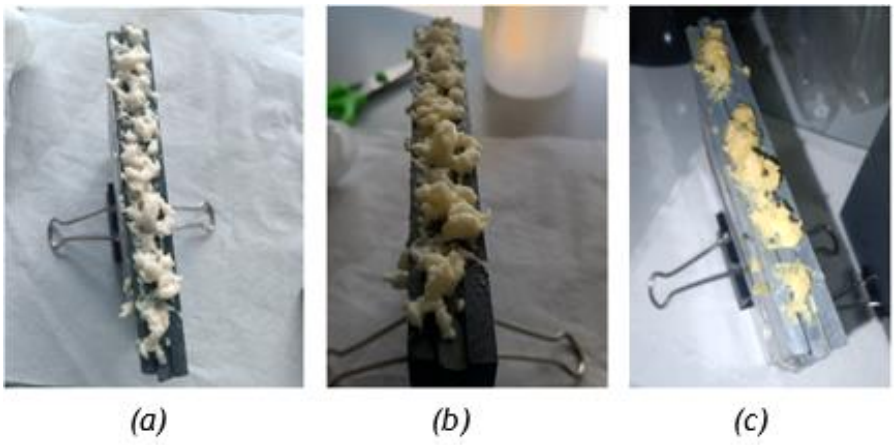

Figure 4.15 Film of test 7 (10% AS, 41% ES) right after application - (a) and (b) -, and after 1 day of cure – (c).

To avoid this phenomenon for the following tests, the agitation time was more carefully controlled. As determined for tests 1 (14% AS) to 3 (50% AS), the increase in the concentration

of AS corresponded to an increase in the homogeneity of the mixture of AS with component A. Regarding the agitation time, the final mixture of test 8 (30% AS, 73% ES) was only agitated for 3 to 5 minutes. There was an improvement in the consistency of the resin, and the application was easier – it was possible to spread the film across the area of application. However, the texture was still gelatinous and so, the film was not uniformly applied. Despite the more effective application of this film, after 1 day of cure, it could be stated that the film tends to crack and even detach form the substrate. The film after the application and after 1 day of cure can be observed in Figure 4.16 (a) and (b), respectively. Since the agitation time was already so little, and even so the curing process seems to negatively affect the application of the film, it can be determined that concentrations of silanes in this range in both components are not suitable to apply as a self-healing technique.

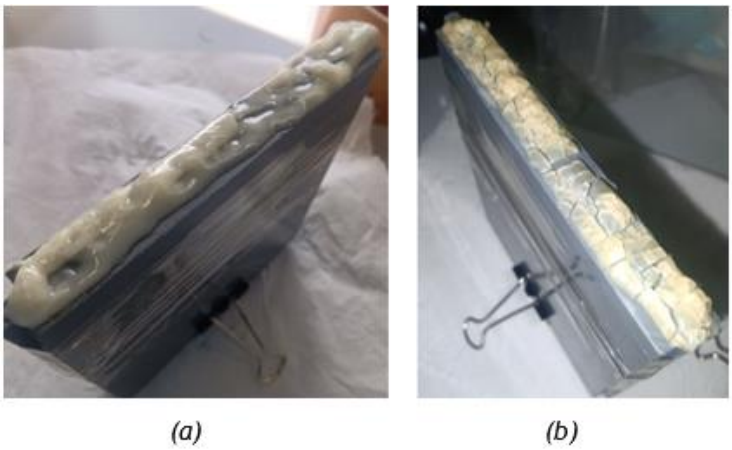

Figure 4.16 Film of test 8 (30% AS, 73% ES) right after application in the PVC substrate (a) and after 1 day of cure.

For test 9 (50% AS, 86% ES), the mix of component A with AS and component B with ES was also carefully followed. The agitation time was approximately the same as for test 8 (3 to 5 minutes). However, the texture obtained was not like the resin from test 8, it was more viscous and gelatinous, and so, the effective application was impossible. This more intense behaviour should be associated with the high concentration of silane compounds that end up affecting the curing process of the original epoxy resin. In Figure 4.17, the results of the application of the film can be seen before (a) and after 1 day of cure.

(a) (b)

Figure 4.17 Film of test 9 (50% AS, 86% ES) right after the application in the PVC substrates (a) and after 1 day of cure (b).

It can be stated that the application of a silane-terminated epoxy resin has a higher stability for compositions where only one of the components has silane monomers. It was also determined that smaller percentages of AS incorporation in component A result in non-homogeneous resins that can affect the uniformity and viability of the film. The addition of ES to component B appears to not affect negatively neither the application nor performance of the resin. Combining both silane monomers drastically changes the curing process and undermines the application of this self-healing technique. Since the concentration of silane monomers in these tests were higher, especially in component B (from 41% to 86%), the agitation could have induced the gelation process of the silane monomers, meaning that crosslinking occurred and resulted in the gelatinous texture of the resin (Brinker, et al. 1982). However, smaller concentrations of ES in component B can be investigated when combined with these concentrations of AS.

Besides evaluating the mixing, cure, and application of the resins with incorporated silane compounds, it was also necessary to analyse the chemical bonds in order to understand possible changes during the preparation of the resins and interaction with the electrolyte. The FTIR spectra are displayed in Appendix B.3. The FTIR analysis registered the transmittance of the sample as a function of the wavenumber (cm^{-1}) in the range of 400 to 4000 cm^{-1}. Several samples were analysed using FTIR: the standard epoxy resin (test 0), the electrolyte used in these tests, the silane monomers and, finally, for each test, a sample of the resin without contact with the electrolyte and with contact with the electrolyte. Only for tests 1 (14% AS) and 2 (30% AS), the resin was only analysed after contacting with the electrolyte, since the electrolyte seemed to flow in between the plates and contacted with the whole extent of the film applied. Regarding test 7 (10% AS, 41% ES), since the application was severely affected by the texture of the resin and did not hold onto the substrate, it was only analysed without contacting with the electrolyte. The identification of each peak is discriminated in Appendix B.2 for all the samples.

Regarding the analysis of test 0 (standard epoxy resin), the FTIR spectrum can be seen in Figure B.1, Appendix B.2. The most relevant peaks are placed at 559, 754 and 827 cm^{-1}, and are related to the C-Cl bond, that is present in bisphenol-A-epichlorohydrin, one of the compounds that constitutes component B in the standard resin. These peaks are also attributed to bending vibrations of the C-H bonds, present in both components of the resin (LibreTexts Chemistry 2023). These vibrations were also attributed to the peak at 1456 cm^{-1}. The stretching vibrations of C-H and methyl groups were detected at 1456, 2854 and 2927 cm^{-1} (Sigma Aldrich 2023). The bonds of component A were represented by the stretching of C-N in the peaks located in the range from 1035 to 1242 cm^{-1}. The bending vibration of N-H also appeared at 1606 cm^{-1} (InstaNano 2023). Component B was also represented by the vibration of epoxy groups, detected at 914 cm^{-1} (Yoshida 2014), by the asymmetric stretching of C-O-C at 1296 cm^{-1} (Panwar, Jassal and Agrawal 2015) and by the vibration of the aromatic C=C bond at 1510 cm^{-1} (ChemEurope 2023).

The pure silane compounds were also analysed, their spectra are presented in Figure B.2, Appendix B.2. These two compounds have a similar spectrum, displaying many peaks and bands in common. In the range of 432 to 449 cm^{-1}, both present Si-O stretching vibration (Tokoro, et al. 2014). Around 820 cm^{-1}, this vibration is also evidenced, in combination with C-H bending, which is also registered at 1442, 1469 cm^{-1}. At 1190 cm^{-1}, C-O stretching appears for both components. Regarding the differences between these compounds: AS presents peaks at 1600 and in the range of 2840 to 2940 cm^{-1} that are attributed to the bending and stretching vibrations of N-H, and stretching of C-N is also evidenced at around 1070 cm^{-1} (Sigma Aldrich 2023). ES presents peaks related to the detection of the epoxy group at around 908 and 1070 cm^{-1} (Yoshida 2014). There is also the presence of O-H bending vibrations in both components around 1400 cm^{-1} (Sigma Aldrich 2023). This could be due to the use of ethanol to clean the FTIR equipment in between readings. Otherwise, it would mean that the silane compounds had suffered partial hydrolysis.

The spectrum of the electrolyte is presented in Figure B.3, Appendix B.2. Most of the readings are large bands, and not specific peaks. The band situated between 400 and 960 cm^{-1} was attributed to vanadium species: bending vibration of V-O, and the stretching vibration of V-O, SO_4 and V-O-S (Chagnes, et al. 2010, Linnell 2020). The peaks at 1049, 1184, 1234 and 2366 cm^{-1} are attributed to sulfuric acid stretching vibrations (Linnell 2020, Appendix - IR Correlation Charts 2018). The O-H bending vibration in 1637 cm^{-1} is either associated to the water of the electrolyte or to the bonds present in sulfuric acid.

Moving on to the spectra of the activated films with and without contacting with the electrolyte. The FTIR spectra was similar for all the tests, as it can be seen in Appendix B.2 from Figure B.4 to Figure B.12. The major difference was found in the analysis of tests 8 and 9

(Figures B.11 and B.12, Appendix B.2) – since the curing of the resin made the film very hard, it was difficult to gather enough sample to place in the FTIR equipment, it kept breaking whenever the analysis was performed. Therefore, fewer individual peaks are observed, and their intensity is lower, compared to other tests.

Analysing the spectrum from test 3 (50% AS) presented in Figure 4.18, as an example, the major difference to point out is the intensity of the bands in the region of 360 to 480 cm^{-1}. As determined before for the analysis of the electrolyte spectrum (Figure B.3, Appendix B.2), this band corresponds to vanadium species and bending vibration of V-O, and the stretching vibration of V-O, SO_4 and V-O-S. Besides, since there are also peaks in the spectrum of the film without contact with the electrolyte, mainly 432, 572 and 682 cm^{-1}, these were attributed to Si-O stretching vibration, and vibration of the C-Cl bond. Since the film combines all these compounds, the same peak can be attributed to several types of vibrations. Two peaks were detected in the area of 690 to 715 cm^{-1}. These were not observed in the analysis of the epoxy resin (Figure B.1, Appendix B.2), however they were assigned to the bending of the C=C bond present in the aromatic ring of the component B. Vibrations of the C-H bond, mainly stretching and bending, were also visible in the other tests, and are placed at around the same values: 1452, 2856, 2925 and 2970 cm^{-1}.

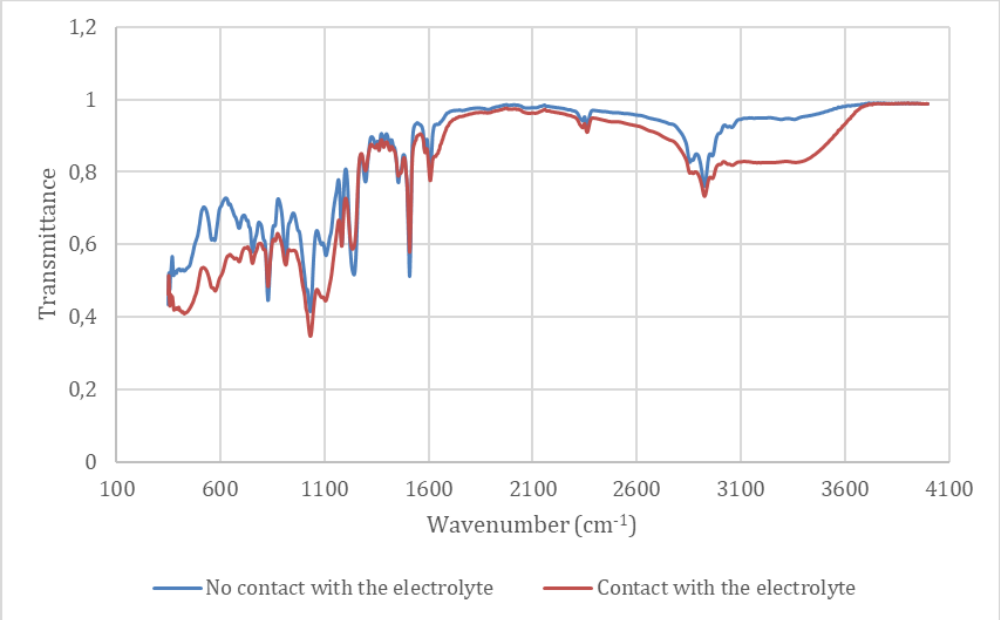

Figure 4.18 FTIR spectra of the test 3 (50% of AS) with and without contact with the electrolyte.

Regarding the determination of the existence of crosslinking, it can be stated that hydrolysis and condensation reactions took place both when the film was in contact with the electrolyte and also when there was supposedly no contact. The crosslinking is evidenced by the peaks registered at around 830 cm^{-1} that is associated with the formation of a silica network (Issa and

Luyt 2019). Besides, there are also peaks suggesting O-H stretching or Si-OH stretching, indicating the hydrolysis of the silane groups, even without contacting with the electrolyte – 914 to 916, 1361 and 2966 cm^{-1} for example (Tokoro, et al. 2014). Another evidence of the occurrence of crosslinking reactions is the presence of peaks at 1027 to 1033 cm^{-1} that indicate the antisymmetric stretching of Si-O-Si sequence (Yang, et al. 2010). Bending vibrations of O-H are also registered for the sample without the electrolyte, ate 1361 cm^{-1}. All these peaks suggest that there is no need to contact with the electrolyte to induce hydrolysis and condensation reactions between silane groups. Besides, this phenomenon could have been triggered by the water involved in the curing process of the epoxy resin – water is released to the environment and so, the contact between the moisturized environment and the silane groups could have easily induced the crosslinking.

To conclude, the incorporation of silane monomers in the components of the epoxy resin is possible, and the application and adhesion to the PVC substrates is not compromised for higher concentrations of AS and lower concentrations of ES, in the investigated interval. The FTIR spectra evidences the existence of hydrolysis and condensation reactions, indicating that the crosslinking mechanism took place just by contacting with water from the electrolyte or from the curing of the epoxy resin. Since the characteristics peaks of these reactions were observed for both samples, it cannot be stated that the hydrolysis mechanism is only triggered when there is electrolyte leakage, however, it seems to be able to prevent the loss of electrolyte.

The tests that appeared to have the best results were test 2 (30% AS), since it successfully contained the electrolyte, and tests 5 (30% ES) and 6 (50% ES), due to the smooth application of the film and preventing the loss of electrolyte. Between these 3, test 6 has a higher concentration of silane groups, and so, the crosslinking mechanism should be more effective with this test. To complement these results, it is suggested that these resins are applied on a working cell to determine the effectiveness of the method.

4.3. EIS measurements

The impedance of the vanadium redox flow cell was investigated under standard operation and with the application of the ID7 film of calcium carbonate. The objective was to determine if there was contamination of the electrolyte by being in contact with the film. In Appendix C, the values obtained from the Thales software and the Nyquist plots are presented, as well as the determination of the charge-transfer resistance. In Table 4.1, the values for the ohmic and charge-transfer resistances are presented for both tests.

Table 4.1 Values obtained for the ohmic and charge-transfer resistances for each test.

	Test 1 (with film)	Test 2 (without film)
R_{Ω} ($\Omega \cdot cm^2$)	0.660	1.101
R_{CT} ($\Omega \cdot cm^2$)	0.202	0.542

If there was contamination of the electrolyte with calcium carbonate, it would be expected that the resistance values of test 1 would be higher, mainly the charge-transfer resistance. However, the resistances determined for test 1 are smaller than the ones provided by test 2. It is expected that there is no significant contamination of the electrolyte, nor the electrodes. However, these tests should be repeated, and complemented with charge-discharge cycles in order to obtain a more correct conclusion regarding the contamination of the components of the cell.

5 Conclusion

The objective of this work was to develop self-healing techniques to prevent electrolyte leakage problems in VRFBs. These problems have severe consequences such as electrolyte imbalance, loss of energy capacity and loss of the battery efficiency, translating in extra costs in maintenance and operation.

To tackle this problem, two different techniques were explored: inducing the precipitation of sulphate salts by the application of a calcium carbonate film in PTFE gaskets and applying a film with silane-terminated compounds in PVC gaskets to induce crosslinking reactions whenever a leak occurs.

Calcium carbonate was mixed with a binder, PVDF, to adhere to the gaskets and induce the precipitation of sulphate salts to obstruct possible leaks. For this, several compositions were tested in order to determine the compositions that combined a proper adhesion to the gasket, while ensuring the availability of sufficient calcium carbonate to induce the rapid precipitation. To improve the adhesion to the PTFE gaskets, these were previously treated with an abrasive paper. It was determined that a film with 60% ratio between solids and solvent, where the solids are 95% $CaCO_3$ and 5% PVDF is the optimal option.

The interaction of the vanadium electrolyte with this film was studied, and precipitates were obtained. These were analysed through FTIR, in the range of 350 – 4000 cm^{-1}. The presence of sulphates and hydroxides and oxides was evidenced, as well as bonds incorporating vanadium atoms. This indicates the precipitation of not only calcium sulphate (the intended product), but also vanadium compounds.

This method in a set up where the leakage of electrolyte was forced. was tested. It was determined that the film was able to prevent loss of electrolyte through a cut with a cross-sectional area of 0,25 mm^2 for a circulation flowrate of 180 $mL \cdot min^{-1}$, using PTFE gaskets for a cell with an active area of 4 cm^2.

The main problems encountered were the poor adhesion of the calcium carbonate film to the material of the gaskets. This could exacerbate the leakage due to uneven thickness of the film. To improve its adhesion, surface treatments of PTFE should be explored. The influence of the torque applied in the assembly of the cell (considering the mechanical resistance of its components) in combination with different film schemes is also an interesting investigation to improve the quality of the application.

The silane-terminated compounds selected had an amine group or an epoxy group and were incorporated in components A and B of an epoxy resin, respectively. Several compositions were tested to evaluate the influence of the silane groups in the stability and applicability of the

resin. Firstly, it was determined that the incorporation of silane compounds in component A (that contained the amine group) was more homogeneous for higher concentrations, and the incorporation of silanes in component B did not present homogeneity problems.

The combination of silanes in both components turned out to be unsuitable to apply the resin in PVC plates – the viscosity increases, originating a gelatinous component that cannot be evenly applied. This indicates that the concentrations of silane monomers were too high, especially in component B - incorporation of silane varied from 41% to 86%. Therefore, the mixing and agitation of both components must have induced the gelation process of the monomers, initiating crosslinking that resulted in the obtained texture. However, lower concentrations can be studied to prevent the gelation process of the silane monomers and improve the applicability of the resin. The best results obtained – meaning that they contained the electrolyte, provided an easy application and contained a considerable concentration of silane monomers – had 30% of silanes on component A, or 50% of silanes in component B.

To evaluate the existence of crosslinking reactions after contact with the electrolyte, the resins were taken to FTIR analysis in the range of 350 – 4000 cm^{-1} after being in contact with the electrolyte and compared to the resin without contacting with the electrolyte. It can be stated that hydrolysis and condensation reactions took place even when the film was not in contact with the electrolyte, since peaks that evidenced the presence of silica network were observed for all the samples, as well as Si-OH bonds. This phenomenon could have been triggered by the water involved in the curing process of the epoxy resin, that reacted with the silane groups and induced hydrolysis and condensation reactions. Hence, it cannot be stated that the hydrolysis mechanism is only triggered when there is electrolyte leakage, constituting a mechanism only triggered by self-healing. However, this technique seems to be able to prevent the loss of electrolyte.

EIS measurements were performed on a single cell to evaluate the influence of the application of calcium carbonate film on the resistances of the cell. The values obtained for the ohmic and charge transfer resistances were 0.660 and 0.202 $\Omega \cdot cm^2$ for the test with the film, and 1.101 and 0.542 $\Omega \cdot cm^2$ for the test without the film, respectively. It was not expected that the resistances of test 2 were higher. From these results, there seems to be no significant contamination of the electrolyte nor the electrode by the film applied. However, further test and other appropriate techniques can be explored to determine more accurately the influence of this film in the performance of the cell.

6 Assessment of the work done

6.1. Objectives Achieved

The aim of this dissertation was to investigate self-healing techniques to apply in vanadium redox flow batteries, to prevent electrolyte loss. The state-of-the-art in this topic was analysed, as well as the functioning of vanadium redox flow batteries and the electrolyte.

Two techniques were chosen to be explored, that rely on precipitation and crosslinking mechanisms. It was found that preventing the loss of electrolyte was possible to a certain extent by applying these techniques. The problems and main difficulties encountered were described. There were also suggested possible investigation alternative paths to respond to the problems encountered.

Therefore, the main objective of this dissertation was achieved, by the exploration of two possible self-healing techniques.

6.2. Other Work Carried Out

The work carried out within the scope of this dissertation has been previously described in this document. No other work was developed other than the elaboration of this thesis.

6.3. Final Assessment

The main objective of this thesis was accomplished: two techniques were investigated as possible solutions to apply as self-healing in vanadium redox flow batteries. The investigation of these techniques involved research of the state-of-the-art, exploration of several possible paths to apply in the cell under study, the elaboration of a work plan to execute the chosen paths to proceed with, and finally, the implementation of this plan, from which the results were analysed.

The conclusions drawn from this work allowed to determine the success of these techniques, as well as possible topics to further investigate.

7 References

Bamgbopa, Musbaudeen O., Saif Almheiri, and Hong Sun. “Prospects of recently developed membraneless cell designs for redox flow batteries.” *Renewable and Sustainable Energy Reviews* (Elsevier) 70 (2017): 506-518.

Hooshmand, Ahmad, Reza Kianoush, Hocine Siad, Mohammed Lachemi, and Mehdi Moslemi. "Investigation of leakage and self-healing of direct tension cracks under sustained loading and high-water pressure." *Construction and Building Materials* (Elsevier) 267, no. 120879 (2020).

2023. https://holooly.com/solutions-v20/characterization-and-wetting-of-teflon-surfaces-measurements-of-contact-angles-for-several-liquids-on-a-polytetrafluoroethylene-surface-teflon-at-20-c-gave-the-following-results/.

“Appendix - IR Correlation Charts.” In *Infrared Raman Spectroscospy*, 261-263. 2018.

Arens, Lukas, Dennis Barther, Jonas Landsgesell, Christian Holm, and Manfred Wilhelm. "Poly(sodium acrylate) hydrogels: synthesis of various network architectures, local molecular dynamics, salt partitioning, desalination and simulation." *The Royal Society of Chemistry* 15 (2019): 9949-9964.

Benatti, Cláudia Telles, Célia Regina Granhen Tavares, and Ervim Lenzi. "Sulfate removal from waste chemicals by precipitation." *Journal of Environmental Management* (Elsevier) 90 (2009): 504-511.

Bengtsson, Magnus, and Kristiina Oksman. "The use of silane technology in crosslinking polyethylene/wood composites." *Composites: Part A* (Elsevier), 2006: 752-765.

Brinker, C. J., K. D. Keefer, D. W. Schaefer, and C. S. Ashley. “Sol-gel transition in simple silicates.” *Journal of Non-Crystalline Solids* (North-Holand Publishing Company) 48 (1982): 47-64.

Carvalho Jr, Waldemir M., et al. "Stability of highly supersaturated vanadium electrolyte solution and characterization of precipitated phases for vanadium redox flow battery." *Journal of Energy Chemistry* (Elsevier) 61 (2021): 436-445.

Chagnes, Alexandre, Marie-Noelle Rager, Bruno Courtaud, Jacques Thiry, and Gérard Cote. “Speciation of vanadium (V) extracted from acidic sulfate media by trioctylamine in n-dodecane modified with 1-tridecanol.” *Hydrometallurgy* (Elsevier), 2010: 20-24.

ChemEurope. *Infrared Spectroscopy correlation Table*. 2023. https://www.chemeurope.com/en/encyclopedia/Infrared_spectroscopy_correlation_table.html.

Cheng, Min. “Electrolyte Optimization and Studies for the Vanadium Redox Flow Battery.” Thesis, School of Chemical Engineering and Industrial Chemistry, 1991.

Cheng, Min. "Electrolyte Optimization and Studies for the Vanadium Redox Flow Battery." Thesis, School of Chemical Engineering and Industrial Chemistry, 1991.

Cho, Hyeongrae, Henning M. Krieg, and Jochen A. Kerres. “Application of Novel Anion-Exchange Blend Membranes (AEBMs) to Vanadium Redox Flow Batteries.” *Membranes* (MDPI) 8 (2018): 33.

Choi, Chanyong, et al. “A review of vanadium electrolytes for vanadium redox flow batteries.” *Renewable and Sustainable Energy Reviews* (Elsevier) 69 (2017): 263-274.

Ciucci, Matteo. *Renewable energy.* April 2023. https://www.europarl.europa.eu/factsheets/en/sheet/70/renewable-energy (accessed May 2023).

Cunha, Álvaro, Jorge Martins, Nuno Rodrigues, and F. P. Brito. “Vanadium redox flow batteries: a technology review.” *International Journal of Energy Research* (Wiley) 39 (2014): 889-918.

Elyashevich, G. K., N. G. Bel’nikevich, and S. A. Vesnebolotskaya. "Swelling–Contraction of Sodium Polyacrylate Hydrogels in Media with Various pH Values." *Polymer Science Series A* 51, no. 5 (2009): 550-553.

Energy Storage. 2023. https://www.irena.org/Energy-Transition/Technology/Energy-Storage.

Evans, Klaire D., Nick J. Ryan, and Ian K. McEwan. "Leak Location & Sealing using Platelet TechnologyTM." *OCEANS 2007 - Europe*. Aberdeen, UK: IEEE, 2007. 1-4.

Fusi, L., M. Primicerio, and A. Monti. "A model for calcium carbonate neutralization in the presence of armoring." *Applied Mathematical Modelling* (Elsevier) 39 (2015): 348-362.

Gal, Jean-Yves, Jean-Claude Bollinger, Henri Tolosa, and Nathalie Gache. “Calcium carbonate solubility: a reappraisal of scale formation and inhibition.” *Talanta* (Elsevier) 43 (1996): 1497-1509.

Ganek, A. G., and T. A. Corbi. “The dawning of the automatic computing era.” *IBM Systems Journal* 42 (2003): 5-18.

Gelest, Inc. "Silanes and Silicones for Epoxy Resins." *Gelest*. 2017. www.gelest.com.

Gordon, Meghan, and Maya Weber. *Global energy demand to grow 47% by 2050, with oil still top source: US EIA*. Edited by Pritish Raj. 6 October 2021. https://www.spglobal.com/commodityinsights/en/market-insights/latest-news/oil/100621-global-energy-demand-to-grow-47-by-2050-with-oil-still-top-source-us-eia (accessed March 3, 2023).

Goss, Sandra L., Karen A. Lemons, Jane E. Kerstetter, and Robin H. Bogner. "Determination of calcium salt solubillity with changes in pH and PCO2, simulating varying gastrointestinal environments." *Journal of Pharmacy and Pharmacology* (The Authors) 59 (2007): 1485-1492.

Han, Xiaopeng, et al. "Metal–Air Batteries: From Static to Flow System." *Advanced Energy Materials* (Wiley) 8 (2018).

Huang, Zebo, Anle Mu, Longxing Wu, Bin Yang, Ye Qian, and Jiahui Wang. "Comprehensive analysis of critical issues in all-vanadium redox flow battery." *ACS Sustainable Chemistry&Engineering* (ACS Publications) 10 (2022): 7786-7810.

InstaNano. *FTIR Functional Group Database Table with Search.* 2023. https://instanano.com/all/characterization/ftir/ftir-functional-group-search/ (accessed June 20, 2023).

Issa, Ahmed A, and Adriaan S Luyt. "Kinetics of alkoxysilanes and organoalkoxysilanes polimerization: a review." *Polymers (Basel)*, 2019.

Iwakiri, Igor, Tiago Antunes, Helena Almeida, João P. Sousa, Rita Bacelar Figueira, and Adélio Mendes. "Redox Flow Batteries: Materials, Design and Prospects." *Energies* (MDPI) 14 (2021).

Jiang, Yan, et al. "Reduction of lead leakage from damaged lead halide perovskite solar modules using self-healing polymer-based encapsulation." *Nature Energy* 4 (2019): 585-593.

Jirabovornwisut, Tossaporn, and Amornchai Arpornwichanop. "A review on electrolyte imbalance in vanadium redox flow batteries." *International Journal of Hydrogen Energy* (Elsevier) 44 (2019): 24485-24509.

Jirabovornwisut, Tossaporn, and Amornchai Arpornwichanop. "A review on the electrolyte imbalance in vanadium redox flow batteries." *International Journal of Hydrogen Energy* (Elsevier) 44 (2019): 24485-24509.

Kang, Guo-dong, and Yi-ming Cao. "Application and modification of poly(vinylidene fluoride) (PVDF) membranes - A review." *Journal of Membrane Science* (Elsevier), 2014: 145-165.

Kim, Donghyeon, Yongbeom Kim, Youngho Lee, and Joonhyeon Jeon. "1,2-Dimethylimidazole based bromine complexing agents for vanadium bromine redox flow batteries." *International Journal of Hydrogen Energy* (Elsevier) 44 (2019): 12024-12032.

Kim, Ki Hyun, Gi Bu Kim, and Gil Dai Lee. "Development of carbon composite bipolar plate (BP) for vanadium redox low battery (VRFB)." *Composite Structures* (Elsevier) 109 (2014): 253-259.

Kurdowski, Wieslaw, and Aleksandra Bochenek. "Three principles of concrete corrosion prevention." *Cement, Wapno, Beton*, 2012: 434-442.

Lee, Nam Jin, et al. “Development of Carbon Composite Bipolar Plates for Vanadium Redox Flow Batteries.” *Bull Korean Chemical Society* 33 (2012): 3589-3592.

León, C. Ponce de, A. Frías-Ferrer, J. González-García, D. A.~ Szánto, and F. C. Walsh. “Redox flow cells for energy conversion.” *Journal of Power Sources* (Elsevier) 160 (2006): 716-732.

Leung, Puiki, Xiaohong Li, Carlos Ponce de León, Leonard Berlouis, C. T. John Low, and Frank C. Walsh. "Progress in redox flow batteries, remaining challenges and their applications in energy storage." *RSC Advances* 2 (2012): 10125-10156.

Li, Liyu, et al. “A Stable Vanadium Redox-Flow Battery with High Energy Density for Large-Scale Energy Storage.” *Advanced Energy Materials* (Wiley Online Library) 1 (2011): 394-400.

Li, Zhibao, and George P. Demopoulos. "Solubility of CaSO4 Phases in Aqueous HCl + CaCl2 Solutions from 283 K to 353 K." *Journal of Chemical Engineering Data* (American Chemical Society) 50 (2005): 1971-1982.

LibreTexts Chemistry. *Infrared Spectroscopy Absorption Table*. 2023. https://chem.libretexts.org/Ancillary_Materials/Reference/Reference_Tables/Spectroscopic_Reference_Tables/Infrared_Spectroscopy_Absorption_Table (accessed June 25, 2023).

Lim, T. M., M. Ulaganathan, and Q. Yan. "Chapter 14." In *Advances in membrane and stack design of redox flow batteries (RFBs) for medium- and large-scale energy storage*, by T. M. Lim, M. Ulaganathan and Q. Yan, 477-507. Singapore: Woodhead Publishing Series in Energy, 2015.

Linnell, Stephanie Frances. “Exploration of vanadium sulfates as positive electrodes for battery applications.” PhD Thesis, University of St. Andrews, 2020.

Lorke, Silke, Uwe Muller, Robert Meissl, and Oliver Bruggemann. "Covalent cross-linking of polymers at room temperature." *International Journal of Adhesion and Adhesives*, 2019: 150-159.

Lourenssen, Kyle, James Williams, Faraz Ahmadpour, Ryan Clemmer, and Syeda Tasnim. “Vanadium redox flow batteries: A comprehensive review.” *Journal of Energy Storage* (Elsevier) 25 (2019).

Mazur, P., et al. “A complex four-point method for the evaluation of ohmic and faradaic losses within a redox flow battery single-cell.” *MethodsX* (Elsevier) 6 (2019): 534-539.

Milshtein, Jarrod D., Robert M. Darling, Javit Drake, Michael L. Perry, and Fikile R. Brushett. “The Critical Role of Supporting Electrolyte Selection on Flow Battery Cost.” *Journal of The Electrochemical Society* 164 (2017): 3883-3895.

Minke, Christine, Ulrich Kunz, and Thomas Turek. “Techno-economic assessment of novel vanadium redox flow batteries with large-area cells.” *Journal of Power Sources* (Elsevier) 361 (2017): 105-114.

Mohamed, M. R., S. M. Sharkh, H. Ahmad, M. N. Abu Seman, and F. C. Walsh. “Design and development of unit cell and system for vanadium redox flow batteries (V-RFB).” *International Journal of the Physical Sciences* (Academic Journals) 7 (2012): 1010-1024.

Morin, C. J., L. Geulin, A. Desbène, and P. L. Desbène. "Study of the acid hydrolysis of (3-methacryloxypropyl)trimethoxysilane by capillary electrophoresis-ion-trap mass spectrometry." *Journal of Chromatography A*, 2004.

Navalpotro, Paula, Catarina M. S. S. Neves, Jesus Palma, Mara G. Freire, João A. P. Coutinho, and Rebeca Marcilla. “Pioneering Use of Ionic Liquid-Based Aqueous Biphasic Systems as Membrane-Free Batteries.” *Advanced Science* (Wiley) 5 (October 2018).

Nyquist, Richard A., and Ronald O. Kagel. “Infrared Spectra of Inorganic Compounds.” *Academic press* (Elsevier), 1971: 1-18.

Pang, Bo, et al. "Superior acidic sulfate ester group based high conductive membrane for vanadium redox flow battery." *Journal of Power Sources*, 2021.

Panwar, Kamlesh, Manjeet Jassal, and Ashwini K Agrawal. “In situ synthesis of Ag–SiO2 Janus particles with epoxy functionality for textile applications.” *Particuology* (Elsevier) 19 (2015): 107-112.

Park, Ji Young, and Jin-Baek Kim. "Room Temperature Processable Organic-Inorganic Hybrid Photolithographic Materials Based on Methoxysilane Cross-Linker." *Polymer Journal*, 2008.

Peng, Yun, Bingjie Sun, and Peiyi Wu. “Two-Dimensional Correlation Infrared Spectroscopic Study on the Crystallization and Gelation of Poly(Vinylidene Fluoride) in Cyclohexanone.” *Applied Spectroscopy* (PubMed) 62 (2008): 295-301.

Pinto, Alexandra M. F. R., B. Vânia Oliveira, and Daniela S. Falcão. "Direct alcohol fuel cells basic science." In *Direct Alcohol Fuel Cells for Portable Applications*, 17-80. Academic Press, 2018.

Pinto, Alexandra M. F. R., Vânia B. Oliveira, and Daniela S. Falcão. "Experimental methods of characterization." In *Direct Alcohol Fuel Cells for Portable Applications*, 113-155. Academic Press, 2018.

Purcar, Violeta, et al. "Effect of Modified Silica Materials on Polyvinyl Chloride (PVC) Substrates to Obtain Transparent and Hydrophobic Hybrid Coatings." *Applied Sciences* (MDPI) 11 (2021).

Rahman, Faizur. "Stability and properties of supersaturated vanadium electrolytes for high energy density vanadium redox flow battery." Ph.D. thesis, School of Chemical Engineering and Industrial Chemistry, The University of New South Wales, Sydney, Australia, 1998.

Ran, Zhipeng, Xiaobing Liu, Xiaolian Jiang, Yeping Wu, and Hong Liao. "Study on curing kinetics of epoxy-amine to reduce temperature caused by the exothermic reaction." *Thermochimica Acta* (Elsevier) 692 (2020).

Sanchez-Díez, Eduardo, et al. "Redox flow batteries: Status and perspective towards sustainable stationary energy storage." *Journal of Power Sources* (Elsevier) 481 (2021).

Sigma Aldrich. *IR Spectrum Table & Chart*. 2023. https://www.sigmaaldrich.com/PT/en/technical-documents/technical-article/analytical-chemistry/photometry-and-reflectometry/ir-spectrum-table (accessed June 20, 2023).

Skyllas-Kazacos, Maria. "Novel vanadium chloride/polyhalide redox flow battery." *Journal of Power Sources* (Elsevier) 124 (2003): 299-302.

Skyllas-Kazacos, Maria, George Kazacos, Grace Poon, and Hugh Verseema. "Recent advances with UNSW vanadium-based redox flow batteries." *International Journal of Energy Research* (Wiley InterScience) 34 (2010): 182-189.

Skyllas-Kazacos, Maria, Liuyue Cao, Chris Menictas, and Jens Noack. "A review of electrolyte additives and impurities in vanadium redox flow batteries." *Journal of Energy Chemistry* (Elsevier), 2018: 1-23.

Skyllas-Kazacos, Maria, Liuyue Cao, Michael Kazacos, Nadeem Kausar, and Asem Mousa. "Vanadium Electrolyte Studies for the Vanadium Redox Battery - A Review." *ChemSusChem* (Wiley Online Library) 9 (2016): 1-24.

Thoubboron, Kerry. *What are the pros and cons of renewable energy?* 2 November 2022. https://news.energysage.com/advantages-and-disadvantages-of-renewable-energy/ (accessed March 2023).

Tian, Chih-Han, Reiyu Chein, Kan-Lin Hsueh, Chun-Hsing Wu, and Fang-Hei Tsau. "Design and modeling of electrolyte pumping power reduction in redox flow cells." *Rare Metals* 30 (2011).

Tokoro, Chiharu, Shinya Suzuki, Daisuke Haraguchi, and Sayaka Izawa. "Silicate removal in aluminum hydroxide co-precipitation process." *Materials (Basel)* (PubMed), 2014: 1084-1096.

Toro, Juan Carlos Ojeda, Izabela Dobrosz-Gómez, and Miguel Ángel Gómez García. "Sodium sulfate solubility in (water + ethanol) mixed solvents in the presence of hydrochloric acid: Experimental measurements and modeling." *Fluid Phase Equilibria* (Elsevier) 384 (2014): 106-113.

Van Loon, Lisa L., and Heather C. Allen. "Methanol Reaction with Sulfuric Acid: A Vibrational Spectroscopy Study." *J. Phys. Chem. B*, 2004: 17666-17674.

Varga, Liz, and Lauren McMillan. "Towards self-healing in water infrastructure systems." In *Proceedings of the Institution of Civil Engineers – Smart Infrastructure and Construction*, by Liz Varga and Lauren McMillan. ICE Publishing, 2022.

Ventosa, Edgar. "Semi-solid flow battery and redox-mediated flow battery: two strategies to implement the use of solid electroactive materials in high-energy redox-flow batteries." *Current Opinion in Chemical Engineering* (Elsevier) 37 (September 2022).

Wang, Xiao, Jingchao Chai, and Jianbing "Jimmy" Jiang. "Redox flow batteries based on insoluble redox-active materials. A review." *Nano Materials Science* (Elsevier) 3 (2021): 17-24.

Weber, Adam Z., Matthew M. Mench, Jeremy P. Meyers, Philip N. Ross, Jeffrey T. Gostick, and Qinghua Liu. "Redox flow batteries: a review." *Journal Applied Electrochemistry* 41 (2011): 1137–1164.

Xiong, Jing, Minghua Jing, Ao Tang, Xinzhuang Fan, Jianguo Liu, and Chuanwei Yan. "Mechanical modelling and simulation analyses of stress distribution and material failure for vanadium rdox flow battery." *Journal of Energy Storage* (Elsevier) 15 (2018): 133-144.

Yang, Lixia, Jun Feng, Wenguang Zhang, and Jun-e Qu. "Experimental and computational study on hydrolysis and condensation kinetics of γ-glycidoxypropyltrimethoxysilane (γ-GPS)." *Applyed Surface Science* (Elsevier) 257 (2010): 990-996.

Yoshida, Shuichiro. "Quantitative evaluation of an epoxy resin dispersion by infrared spectroscopy." *Polymer Journal* (Nature) 46 (2014): 430-434.

Appendix A. Precipitation as a self-healing technique

A.1 Determination of the composition of the solutions and FTIR analysis

For ID1, the intended composition was a solids/solvent ratio of 50%, and that the solid material were to be composed of 95% of calcium carbonate, and 5% of PVDF, to maximize the amount of calcium available.

For a total mass of solids of 1 g, it was determined that the mass of calcium carbonate and PVDF should be calculated respectively as

$$m_{\mathrm{CaCO_3}} = 0.95 \times 1 = 0.95\ g \tag{A.1}$$

$$m_{\mathrm{PVDF}} = 0.05 \times 1 = 0.05\ g \tag{A.2}$$

To obey the intended solids/solvent ratio, the mass of NMP was determined as following

$$m_{\mathrm{NMP}} = \frac{\left(m_{\mathrm{CaCO_3}} + m_{\mathrm{PVDF}}\right)}{0.50} = \frac{(0.95 + 0.05)}{0.50} = 2.00\ g \tag{A.3}$$

To determine the necessary volume of solvent to measure with the graduated pipette, the density of NMP was considered to be $\rho = 1.03\ \mathrm{g \cdot cm^{-3}}$

$$V_{\mathrm{NMP}} = \frac{(m_{\mathrm{NMP}})}{\rho} = \frac{2{,}00}{1.03} = 1.94\ mL \tag{A.4}$$

The results obtained from FTIR analysis are presented in the following Figures. Figure A.1 presents the spectrum of the film with calcium carbonate and PVDF applied in the gaskets.

Figure A.2 shows the FTIR spectrum of the electrolyte after precipitation with the film of calcium carbonate and PVDF.

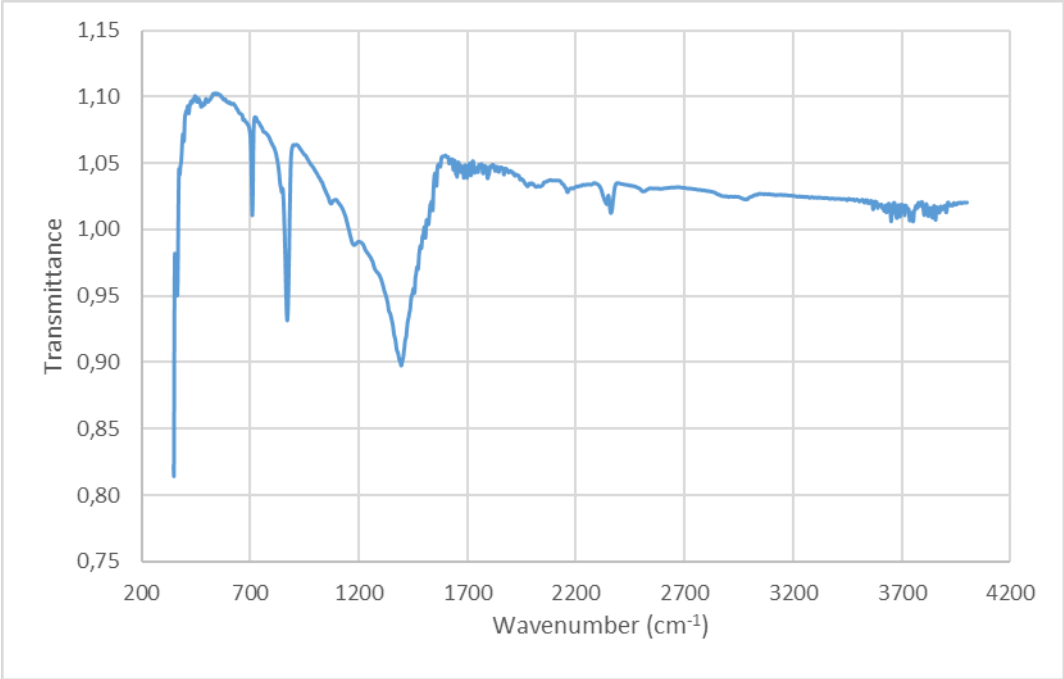

Figure A.1 FTIR spectrum of the film of calcium carbonate and PVDF applied in the gaskets.

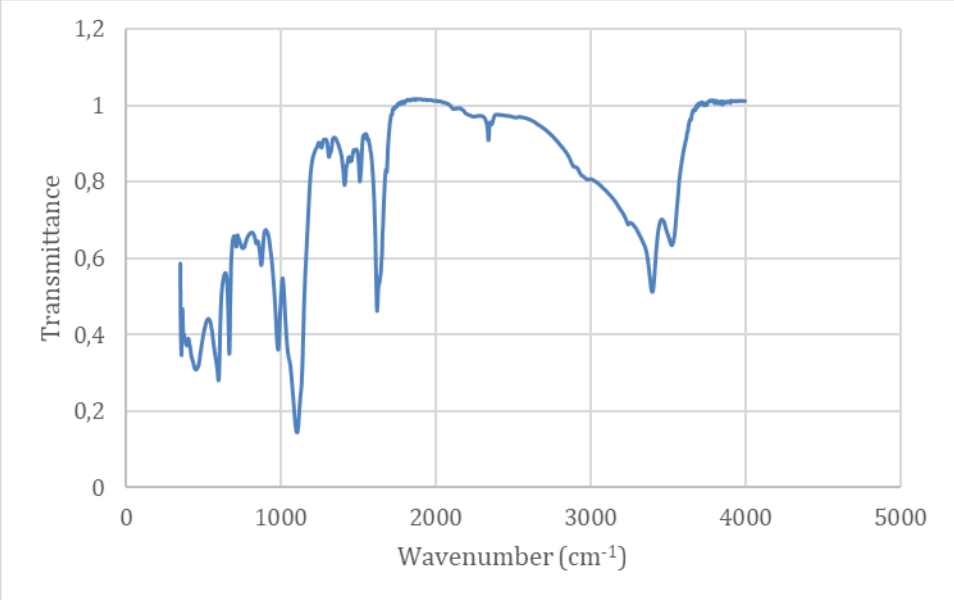

Figure A.2 FTIR spectrum of the electrolyte after precipitation with the film of calcium carbonate and PVDF.

A.2 Results of the tests using Gasket 1

The flowrate values registered for the tests performed with gasket 1 are here presented. In Table A.1, the leakage flowrates before the application of the calcium carbonate film are presented.

Table A.1 Values measured for the leakage flowrate of gasket 1 before the application of the calcium carbonate film.

	Pump flowrate ($mL \cdot min^{-1}$)	Leak flowrate ($mL \cdot min^{-1}$)			Average leak flowrate ($mL \cdot min^{-1}$)	$\frac{Average\ leak\ flowrate}{Pump\ flowrate}$ (%)
		1st measurement	2nd measurement	3rd measurement		
q_1	5	3.06	3.16	3.11	3.16	63
q_2	10	5.38	5.34	5.19	5.30	53
q_3	15	7.47	7.39	7.44	7.43	50
q_4	25	11.6	11.6	11.5	11.6	46
q_5	30	13.4	13.3	13.3	13.3	44

In Table A.2, the results of the leakage flowrate after the application of the film. The film was synthesized according to the composition ID7, and applied with a thickness of 300 μm, dried at room temperature. The gaskets that were covered with the film have a thickness of 0.2 mm and were previously polished to allow a better application.

Table A.2 Values of the leakage flowrate of gasket 1 after the application of ID7 film with 300 μm, dried at room temperature.

Pump flowrate ($mL \cdot min^{-1}$)	Leak flowrate ($mL \cdot min^{-1}$)			Average leak flowrate ($mL \cdot min^{-1}$)	Average leak flowrate without the film ($mL \cdot min^{-1}$)
	1st measurement	2nd measurement	3rd measurement		
5	1.76	1.34	1.39	1.50	3.16

A.3 Results of the tests using Gasket 2

The flowrate values registered for the tests performed with gasket 2 are here presented. In Table A.3, the leakage flowrates before the application of the calcium carbonate film are presented.

Table A.3 Values measured for the leakage flowrate of gasket 2 before the application of the calcium carbonate film.

	Pump flowrate ($mL \cdot min^{-1}$)	Leak flowrate ($mL \cdot min^{-1}$)			Average leak flowrate ($mL \cdot min^{-1}$)	$\frac{Average\ leak\ flowra}{Pump\ flowrate}$ (%)
		1st measurement	2nd measurement	3rd measurement		
q_1	15	0.131	0.0951	0.0832	0.103	0.690
q_2	20	0.165	0.171	0.166	0.167	0.840
q_3	25	0.263	0.0939	0.163	0.173	0.690
q_4	30	0.204	0.237	0.250	0.230	0.760
q_5	35	0.365	0.418	0.415	0.399	1.14

In Table A.4, the results of the leakage flowrate after the application of the film. The film was synthesized according to the composition ID7, and applied with a thickness of 500 µm, dried at 40 °C. The gaskets that were covered with the film have a thickness of 0.2 mm and were previously polished to allow a better application.

Table A.4 Values of the leakage flowrate of gasket 2 after the application of ID7 film with 500 µm, dried at 40 °C.

Pump flowrate ($mL \cdot min^{-1}$)	Leak flowrate ($mL \cdot min^{-1}$)			Average leak flowrate ($mL \cdot min^{-1}$)	Average leak flowrate without the film ($mL \cdot min^{-1}$)
	1st measurement	2nd measurement	3rd measurement		
15	0.194	0.166	0.210	0.190	0.103

Figure A.3 consists of the photos of the gaskets covered with the film after the experiment from Table A.4.

(a) (b)

Figure A.3 Photos of the gaskets covered with 500 µm of ID7 film, dried at 40 °C, after experiment with gasket 2 – (a) is one of the gaskets and (b) is the other one.

In Table A.5, the results of the leakage flowrate after the application of the film. The film was synthesized according to the composition ID7, and applied with a thickness of 500 µm, dried at room temperature. The gaskets that were covered with the film have a thickness of 0.5 mm and were previously polished to allow a better application. This film was applied with a different scheme, to leave a margin without any film around the electrode, to prevent the contamination of the electrolyte in circulation. This scheme, as well as the photos of the gaskets after this experiment are presented in Figure 4.5 (chapter 4).

Table A.5 5 Values of the leakage flowrate of gasket 2 after the application, leaving a margin around the electrode, of ID7 film with 500 µm, dried at room temperature.

Pump flowrate ($mL \cdot min^{-1}$)	Leak flowrate ($mL \cdot min^{-1}$)			Average leak flowrate ($mL \cdot min^{-1}$)	Average leak flowrate without the film ($mL \cdot min^{-1}$)
	1st measurement	2nd measurement	3rd measurement		
5	0,346	---	---	0,346	<<0,103

In Table A.6, the results of the leakage flowrate after the application of the film. The film was synthesized according to the composition ID6, and applied with a thickness of 500 µm, dried at room temperature. The gaskets that were covered with the film have a thickness of 0.5 mm and were previously polished to allow a better application.

Table A.6 Values of the leakage flowrate of gasket 2 after the application of ID6 film with 500 μm, dried at room temperature.

Pump flowrate ($mL \cdot min^{-1}$)	Leak flowrate ($mL \cdot min^{-1}$)			Average leak flowrate ($mL \cdot min^{-1}$)	Average leak flowrate without the film ($mL \cdot min^{-1}$)
	1st measurement	2nd measurement	3rd measurement		
5	0.175	0.200	---	0.188	<<0.103

A.4 Results of the tests using Gasket 3

The flowrate values registered for the tests performed with gasket 3 are here presented. In Table A.7, the leakage flowrates before the application of the calcium carbonate film are presented.

Table A.7 Values measured for the leakage flowrate of gasket 3 before the application of the calcium carbonate film.

	Pump flowrate ($mL \cdot min^{-1}$)	Leak flowrate ($mL \cdot min^{-1}$)			Average leak flowrate ($mL \cdot min^{-1}$)	$\frac{Average\ leak\ flowrat}{Pump\ flowrate}$ (%)
		1st measurement	2nd measurement	3rd measurement		
q_1	180	0.0646	0.0643	0.0679	0.0656	0.0364
q_2	200	0.0756	0.0756	0.0813	0.0775	0.0388
q_3	220	0.0939	0.0797	0.0849	0.0862	0.0392
q_4	230	0.108	0.106	0.101	0.105	0.0457
q_5	241	0.196	0.190	0.167	0.184	0.0763

In Table A.8, the results of the leakage flowrate after the application of the film. The film was synthesized according to the composition ID7, and applied with a thickness of 500 μm, dried at room temperature. The gaskets that were covered with the film have a thickness of 0.5 mm and were previously polished to allow a better application. This film was applied with a different scheme, to prevent the contamination of the circulating electrolyte and the exacerbation of the leakage. This scheme, as well as the photos of the gaskets after this experiment are presented in Figure A.4.

Table A.8 Values of the leakage flowrate of gasket 3 after the application, leaving a margin around the electrode, of ID7 film with 500 µm, dried at room temperature.

Pump flowrate ($mL \cdot min^{-1}$)	Leak flowrate ($mL \cdot min^{-1}$)			Average leak flowrate ($mL \cdot min^{-1}$)	Average leak flowrate without the film ($mL \cdot min^{-1}$)
	1st measurement	2nd measurement	3rd measurement		
180	0.0751	0.0861	---	0.0806	0.0656

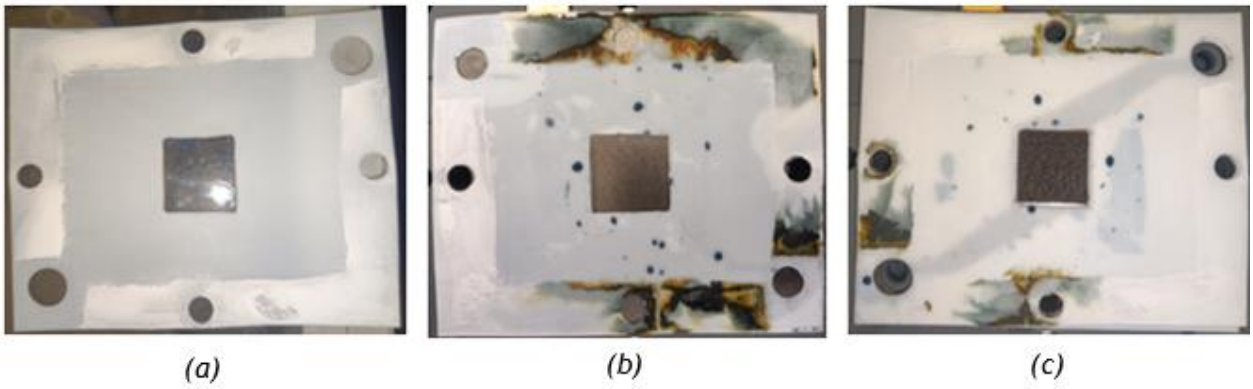

Figure A.4 PTFE gaskets with a 500 µm film of ID7 applied with a different scheme - (a) scheme applied; (b) and (c) gaskets with the film after the experiment with gasket 3.

In Figure A.5 are the photos of an experiment in the same conditions as the experiment represented in Figure A.4, where the loss of electrolyte was prevented.

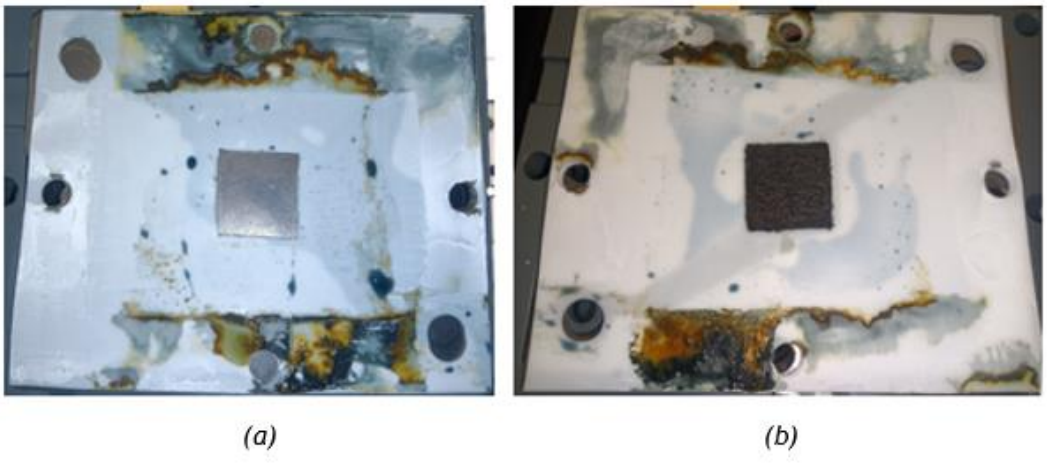

Figure A.5 PTFE gaskets with a 500 µm film of ID7 applied with a different scheme - (a) and (b) gaskets with the film after the experiment with gasket 3.

In Table A.9, the results of the leakage flowrate after the application of the film. The film was synthesized according to the composition ID7, and applied with a thickness of 500 µm, dried at room temperature. The gaskets that were covered with the film have a thickness of 0,5 mm and were previously polished to allow a better application. This film was applied with a

different scheme, to prevent the contamination of the circulating electrolyte and the exacerbation of the leakage. This scheme, as well as the photos of the gaskets after this experiment are presented in Figure A.6.

Table A.9 Values of the leakage flowrate of gasket 3 after the application, leaving a margin around the electrode, of ID7 film with 500 µm, dried at room temperature.

Pump flowrate ($mL \cdot min^{-1}$)	**Leak flowrate ($mL \cdot min^{-1}$)**			**Average leak flowrate ($mL \cdot min^{-1}$)**	**Average leak flowrate without the film ($mL \cdot min^{-1}$)**
	1st measurement	2nd measurement	3rd measurement		
180	0.0390	---	---	0.0390	0.0656

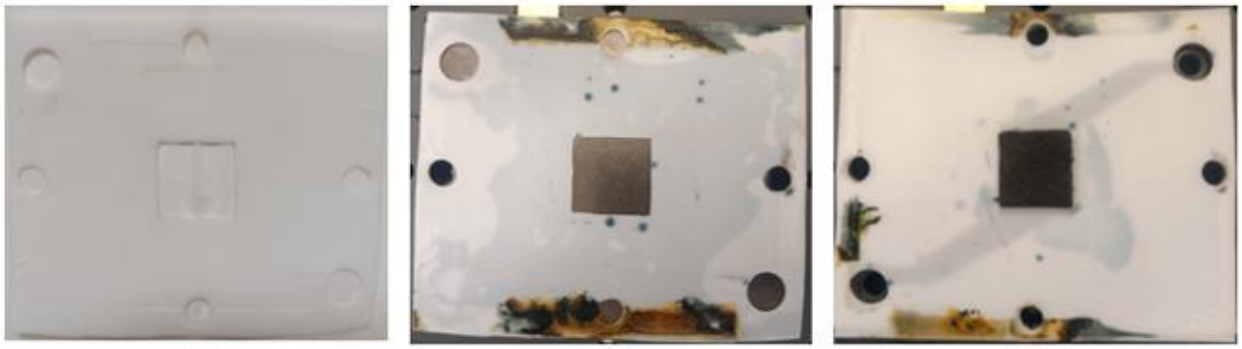

Figure A.6 PTFE gaskets with a 500 µm film of ID7 applied with a different scheme - (a) scheme applied; (b) and (c) gaskets with the film after the experiment with gasket 3.

Appendix B. Crosslinking as a self-healing technique

B.1 Determination of the composition of the resins

To determine the necessary amount of each component, the total volume was calculated using the PVC plates measurements presented in Table B.1.

Table B.1 Dimensions of the PVC plates.

Dimensions of the gaskets	
Thickness	0.4 cm
Width	10 cm
Length	10 cm

The volume of resin necessary to make up a film that covers the bottom of the test setup was determined considering a thickness of 0,2 mm, as explained in equation B.1.

$$V_{film} = 3 \times 0.4 \times 10 \times 0.2 = 2.4\ cm^3 \quad \text{(B.1)}$$

The density of the resin was considered to be $\rho = 1.2\ \mathrm{g \cdot cm^{-3}}$, so, the mass of film for each test is as determined in equation B.2

$$m_{film} = \rho \times V_{film} = 1.2 \times 2.4 = 2.88\ g \quad \text{(B.2)}$$

According to the supplier of the epoxy resin used in these tests, the components come in the following proportions: $\frac{A}{B} = \frac{0,76}{0,24}$. Therefore, for a total mass of 2.88 g, the mass of components A and B for test 0 (standard version of the resin) are presented in equations B.3 and B.4.

$$m_A = 0.76 \times m_{film} = 0.76 \times 2.88 = 2.19\ g \quad \text{(B.3)}$$

$$m_B = 0.24 \times m_{film} = 0.24 \times 2.88 = 0.69\ g \quad \text{(B.4)}$$

In the following equations, the calculations to determine the quantities of each component for the incorporation of AS in component A are presented for test 1. Since the substitution is of 10 %, the mass of AS was determined by equation B.5.

$$m_{AS1} = 0.10 \times m_A = 0.10 \times 2.19 = 0.22\ g \quad \text{(B.5)}$$

To adjust the ratio of epoxy/amine components, the mols of epoxy groups to add needs to be determined. In equation B.6, the number of amine groups is determined, which corresponds to half of the corresponding epoxy groups (equation B.7) – since AS is a secondary amine, each molecule can bond with two epoxy groups.

$$n_{AS1} = \frac{m_{AS1}}{MM_{AS}} = \frac{0.22}{147.29} = 0.00149\ mol \quad \text{(B.6)}$$

$$n_{epoxy1} = 2 \times n_{AS1} = 2 \times 0.00149 = 0.00299\ mol \quad \text{(B.7)}$$

The next step is to determine the amount of component B that corresponds to the mass of AS incorporated in the resin. In Table B.2, the information on the composition of component B provided by the supplier is described.

Table B.2 Information on the composition of component B provided by the supplier.

Compound	Quantity (%)
Benzyl alcohol	1-10
Bisphenol-A-epichlorohydrin (BE)	25-100
2,3-epoxypropyl neodecanoate (EN)	1-25

For the calculations, the composition was considered to be 10% of benzyl alcohol, 75% of bisphenol-A-epichlorohydrin and 15% of 2,3-epoxypropyl neodecanoate. Therefore, in 10 g of component B, the amount of each compound is calculated in equations B.8 and B.9.

$$n_{BE} = \frac{0.75 \times m_{film}}{MM_{BE}} = \frac{0.75 \times 2.88}{320.8} = 0.00673\ mol \quad \text{(B.8)}$$

$$n_{EN} = \frac{0.75 \times m_{film}}{MM_{EN}} = \frac{0.75 \times 2.88}{228.33} = 0.00189\ mol \quad \text{(B.9)}$$

$$n_{total} = n_{BE} + n_{EN} = 0{,}00863\ mol \quad \text{(B.10)}$$

For the amount of epoxy groups calculated in equation B.7, the amount of component B to add is the following:

$$m_{BE1} = \frac{n_{BE}}{n_{total}} \times n_{epoxy1} \times MM_{BE} = 0.748\ g \quad \text{(B.11)}$$

$$m_{EN1} = \frac{n_{EN}}{n_{total}} \times n_{epoxy1} \times MM_{EN} = 0.149\ g \quad \text{(B.12)}$$

$$m_{epoxy1} = m_{BE} + m_{EN} = 0.898\ g \quad \text{(B.13)}$$

$$m_{B1} = \frac{m_{epoxy}}{0.75 + 0.15} = 0.997\ g \quad \text{(B.14)}$$

The mass of component A is adjusted as presented in equation B.15, and the corresponding mass of component B is calculated as demonstrated in equation B.16.

$$m_{A1} = m_A - m_{AS} = \ 1.97\ g \tag{B.15}$$

$$m_{B1_{total}} = \frac{0.24}{0.76} \times m_{A1} + m_{B1} = \ 1.62\ g \tag{B.16}$$

Reggarding the incorporation of ES in component B, test 4 is presented as an example. In equation B.17, the mass of ES is calculated for substituting 10% in component B.

$$m_{ES4} = 0.10 \times m_B = \ 0.10 \times 0.69 = 0.07\ g \tag{B.17}$$

To adjust the amount of component A it was necessary to establish a relation between the mols of epoxy and the mass of component A in the standard formulation of the resin. In equation B.18, the number of epoxy groups correspondent to 76 g of component A is calculated.

$$n_{epoxy4} = \frac{0.75 \times 24}{MM_{BE}} + \frac{0.15 \times 24}{MM_{EN}} = 0.072\ mol \tag{B.18}$$

The mass of component A is now calculated in equation B.19 based on the established relationship.

$$m_{A4} = \frac{m_{ES4}}{MM_{ES}} \times \frac{76}{n_{epoxy4}} = 0.50\ g \tag{B.19}$$

In equations B.20 and B.21 is the determination of the mass of component B, and the total mass of component A to incorporate the 10% of ES in the mixture.

$$m_{B4} = m_B - m_{ES4} = \ 0.62\ g \tag{B.20}$$

$$m_{A4_{total}} = \frac{0.76}{0.24} \times m_{B4} + m_{A4} = 2.46\ g \tag{B.21}$$

For the combination of AS with ES, the calculations of test 4 (10% of AS and 22,1% of ES) will be presented as an example. The mass of AS was determined as in equation B.5, and the number of mols was calculated through equation B.6. The number of mols of epoxy to add is also determined as in equation B.7. Since these epoxy groups come from ES, the mass of this component is calculated by equation B.22.

$$m_{ES7} = \frac{n_{epoxy1}}{MM_{ES}} = \ 0.43\ g \tag{B.22}$$

The mass of component A is determined as in equation B.15 and the mass of component B is calculated through equation B.23.

$$m_{B7} = \frac{0.24}{0.76} \times m_{A1} = 0.62\ g \tag{B.23}$$

B.2 Synthesis and application of the resins

In Table B.3 are the experimental values of the mass of each component for all the tests performed.

Table B.3 Experimental values of the mass of each component for all the tests performed.

Test	Component A (g)	Component B (g)	AS (g)	ES (g)
0	2.43	0.77	---	---
1	1.99	2.12	0.33	---
2	1.54	3.49	0.66	---
3	1.09	5.32	1.11	---
4	2.60	0.62	---	0.07
5	3.05	0.48	---	0.21
6	3.59	0.38	---	0.35
7	1.97	0.62	0.22	0.43
8	1.53	0.49	0.69	1.30
9	1.09	0.35	1.09	2.17

B.3 FTIR analysis of the epoxy-silane resins

Here are presented the FTIR spectra for all the tests and compounds used in this technique, and the respective tables with the analysis of the peaks.

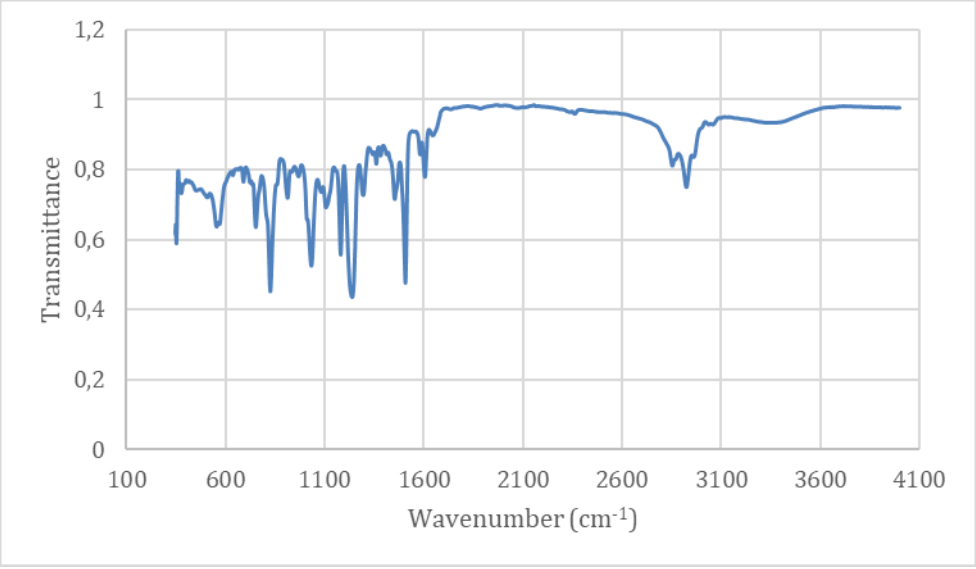

Figure B.1 FTIR spectra of the standard epoxy resin (test 0).

Table B.4 FTIR analysis of the peaks and bands observed in Figure B.1 for test 0.

Peaks (cm^{-1})	Vibration
559	C-Cl
754, 827	C-H bending and/or C-Cl
914	Epoxy groups
1035, 1110, 1182, 1242	C-N stretching
1296	C-O-C asymmetric stretching
1456, 2927	C-H bending, CH_3 asymmetric stretch
1510	aromatic C=C
1606	N-H bending
2854	C-H stretching
3373	O-H stretching

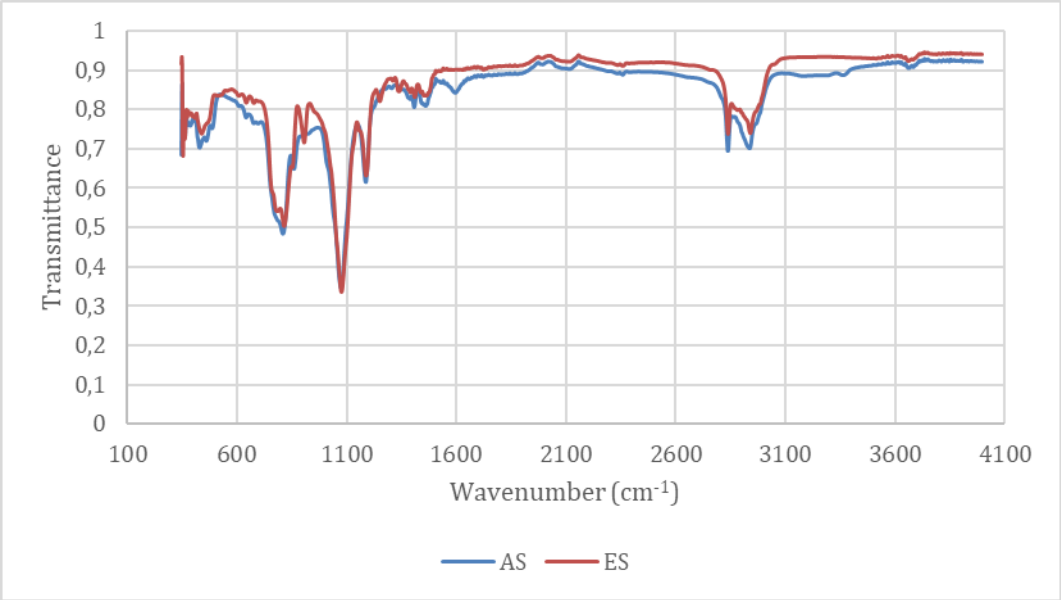

Figure B.2 FTIR spectra of the pure silane compounds incorporated in the resin.

Table B.5 FTIR analysis of the peaks and bands observed in Figure B.2 for AS and ES.

Peaks (cm^{-1})	AS	ES
432, 449	Si-O stretching	
466, 493	Si-O deformation	---
702	C-H stretching (Si-CH2-CH2-Si)	---
815, 823	C-H bending, Si-C stretching	
867	C-H bending	---
908	---	Epoxy groups
1072, 1074	C-N, C-O and/or Si-O stretching	C-O-C epoxy group, Si-O stretching
1191, 1195	C-O stretching	
1257	---	CH_2 torsion; C-H deformation; O-H deformation
1348, 1402, 1405	O-H bending	
1442, 1469	C-H bending, CH_3 asymmetric stretch	
1600	N-H bending	---
2840 - 2940	N-H and/or C-H stretching	C-H stretching

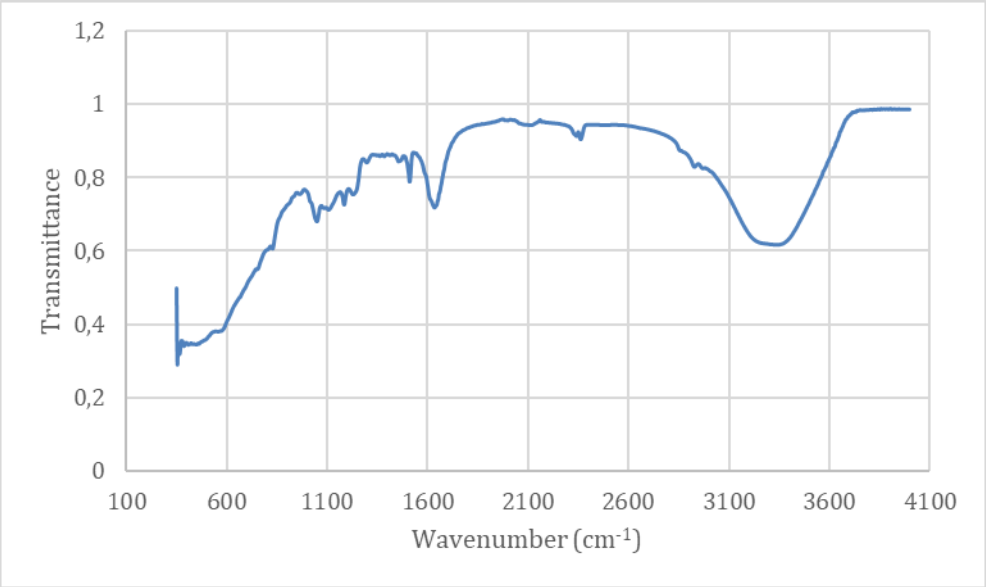

Figure B.3 FTIR spectra of the electrolyte.

Table B.6 FTIR analysis of the peaks and bands observed in Figure B.3 for the electrolyte.

Peaks (cm^{-1})	Vibration
400 – 960	Vanadium species, V-O bending, V-O stretching, -SO_4 stretching, V-O-S stretching
1049	S=O stretching, S-O stretching
1184, 1234	S-O stretching
1637	O-H bending vibration
2366	S-OH stretching
2927, 3000-5000	O-H stretching

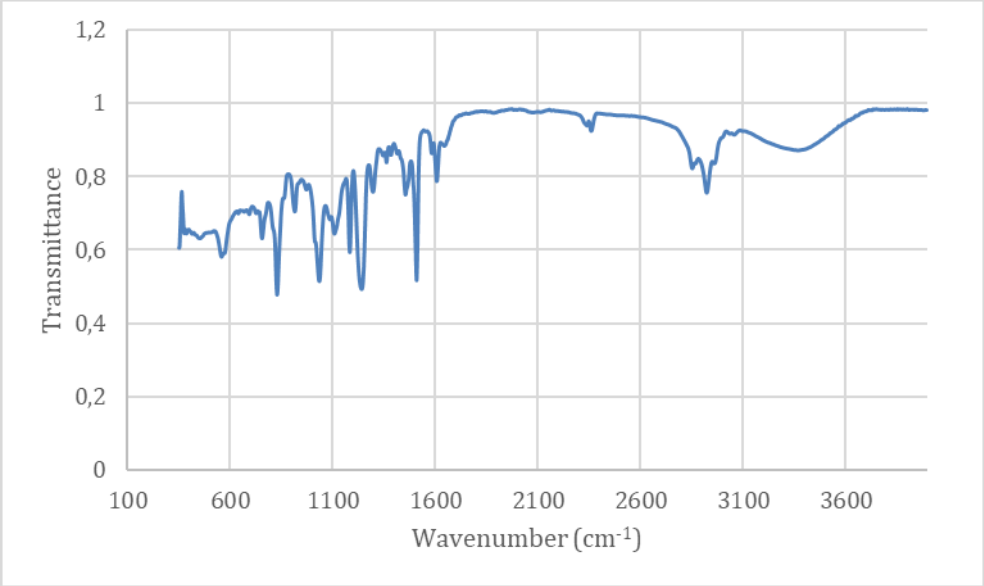

Figure B.4 FTIR spectra of the test 1 (10% of AS) with contact with the electrolyte.

Table B.7 FTIR analysis of the peaks and bands observed in Figure B.4 for test 1 with contact with the electrolyte.

PEAKS (CM^{-1})	Vibration
464	Vanadium species, V-O bending, V-O stretching, -SO_4 stretching, V-O-S stretching
572	C-Cl
756	C-H bending and/or C-Cl
827	Silica network
914	Si-OH stretch and/or epoxy groups
970	C=C bending
1035	Antisymmetric stretching of Si-O-Si sequence
1110	Si-O stretching
1182, 1234	S-O and/or C-N stretching
1294	C-O-C asymmetric stretching vibration of epoxy group
1361	O-H bending
1454	C-H bending and/or CH_3 asymmetric stretch
1508	aromatic C=C
1596, 1608	N-H bending
1650	H_2O stretch
2362	S-OH stretch
2856	C-H stretch
2925, 2966	C-H symmetric and asymmetric stretch
3100-3600	SiO-H and/or O-H stretching

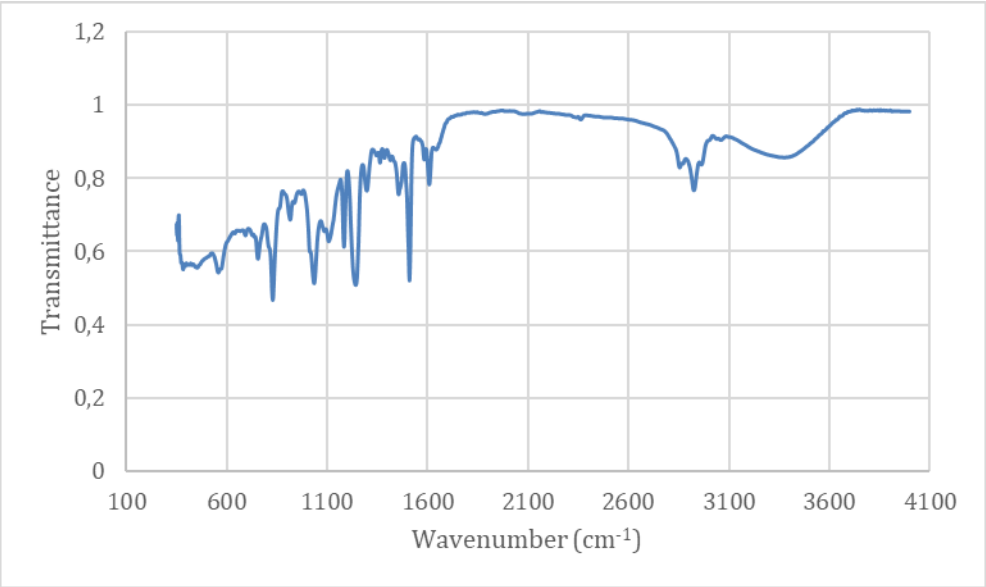

Figure B.5 FTIR spectra of the test 2 (20% of AS) with contact with the electrolyte.

Table B. 1 FTIR analysis of the peaks and bands observed in Figure B.5 for test 2 with contact with the electrolyte.

PEAKS (CM^{-1})	**Vibration**
455	Vanadium species, V-O bending, V-O stretching, -SO_4 stretching, V-O-S stretching
572	C-Cl
756	C-H bending and/or C-Cl
829	Silica network
914	Si-OH stretch and/or epoxy groups
1033	Antisymmetric stretching of Si-O-Si sequence
1108	Si-O stretching
1222	C-N stretching
1242	S-O and/or C-N stretching
1296	C-O-C asymmetric stretching vibration of epoxy group
1361	O-H bending
1458	C-H bending and/or CH_3 asymmetric stretch
1510	aromatic C=C
1579	C=C stretching
1606	N-H bending
2364	S-OH stretch
2860	C-H stretch
2927, 2966	C-H symmetric and asymmetric stretch
3220-3600	SiO-H and/or O-H stretching

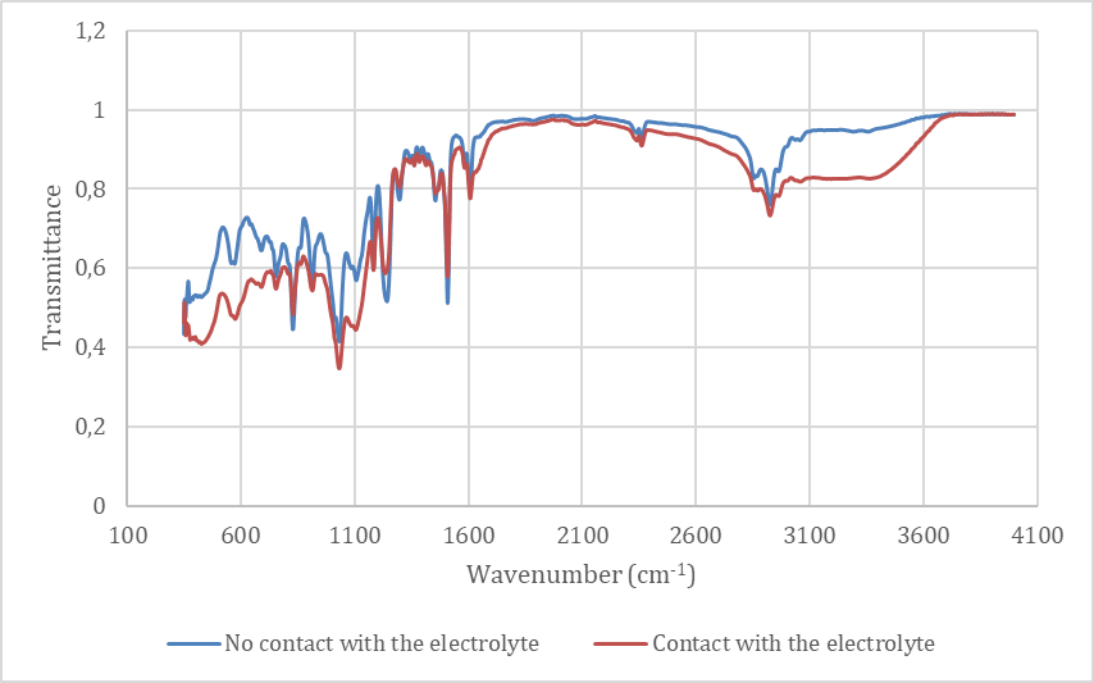

Figure B.6 FTIR spectra of the test 3 (50% of AS) with and without contact with the electrolyte.

Table B.8 FTIR analysis of the peaks and bands observed in Figure B.6 for test 3 with and without contact with the electrolyte.

Peaks (cm^{-1})	Without contact with the electrolyte	With contact with the electrolyte
432	Si-O stretching	---
360 - 480	---	Vanadium species, V-O bending, V-O stretching, -SO_4 stretching, V-O-S stretching
572, 576	C-Cl	
692, 694, 713	C=C bending	
756, 754, 771	C-H bending, C-Cl	
825-829	Silica network	
914 - 916	Si-OH stretch, Epoxy groups	
1027 - 1033	Antisymmetric stretching of Si-O-Si sequence	
1100 - 1107	Si-O stretching	
1182 - 1243	S-O and/or C-N stretching	
1296, 1299	C-O-C asymmetric stretching	
1361	O-H bending	---
1452 - 1454	C-H bending, CH_3 asymmetric stretch	
1508	Aromatic C=C	
1579	C=C stretching	---
1606, 1608	N-H bending	
2856 - 2858	C-H stretching	
2921 - 2927	C-H (CH_2 and CH_3) symmetric and asymmetric stretch	
2966 - 2970	SiO-H stretching	
3100 - 3600	---	SiO-H and/or O-H stretching

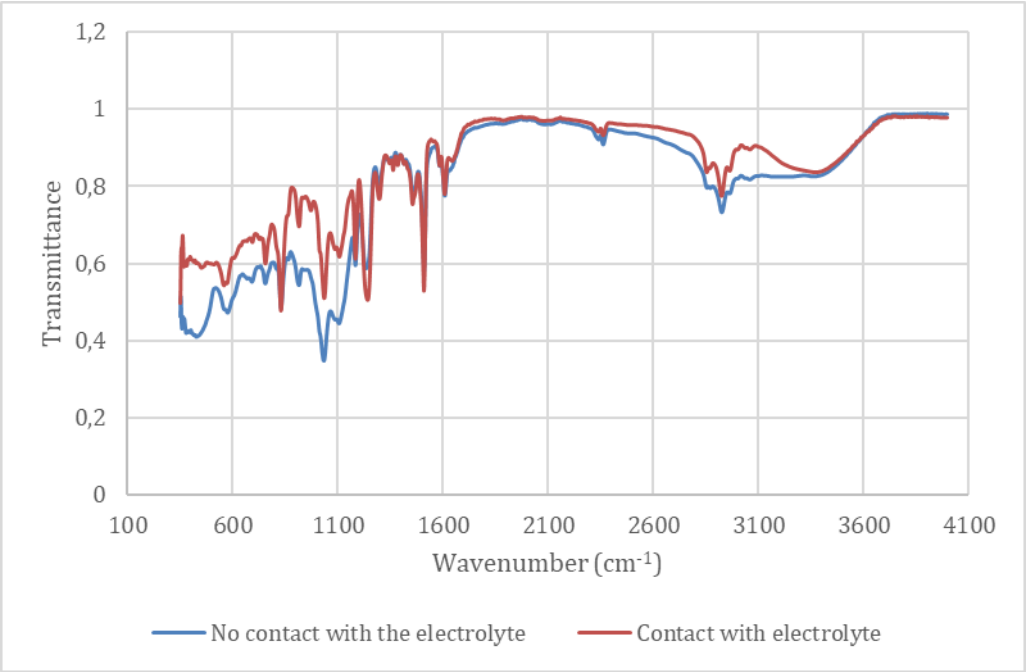

Figure B.7 FTIR spectra of test 4 (10% of ES) with and without contact with the electrolyte.

Table B.9 FTIR analysis of the peaks and bands observed in Figure B.7 for test 4 without and with contact with the electrolyte.

Peaks (cm^{-1})	Without contact with the electrolyte	With contact with the electrolyte
460	O-Si-O or Si-O deformation	O-Si-O or Si-O deformation, and/or vanadium species, V-O bending, V-O stretching, -SO_4 stretching, V-O-S stretching
557 - 571	C-Cl	
750 - 754	C-H bending, C-Cl	
825-831	Silica network	
910 - 914	Si-OH stretch, Epoxy groups	
995	C=C bending	
1029 - 1037	Antisymmetric stretching of Si-O-Si sequence	
1105, 1108	Si-O stretching	
1180 - 1242	S-O and/or C-N stretching	
1297	C-O-C asymmetric stretching	
1363 - 1365	O-H bending	---
1452 - 1458	C-H bending, CH_3 asymmetric stretch	
1508 - 1510	Aromatic C=C	
1606 - 1610	N-H bending	
2362	---	S-OH stretching
2850 – 2856, 2921 - 2927	C-H (CH_2 and CH_3) symmetric and asymmetric stretch	
3100 - 3600	SiO-H and/or O-H stretching	

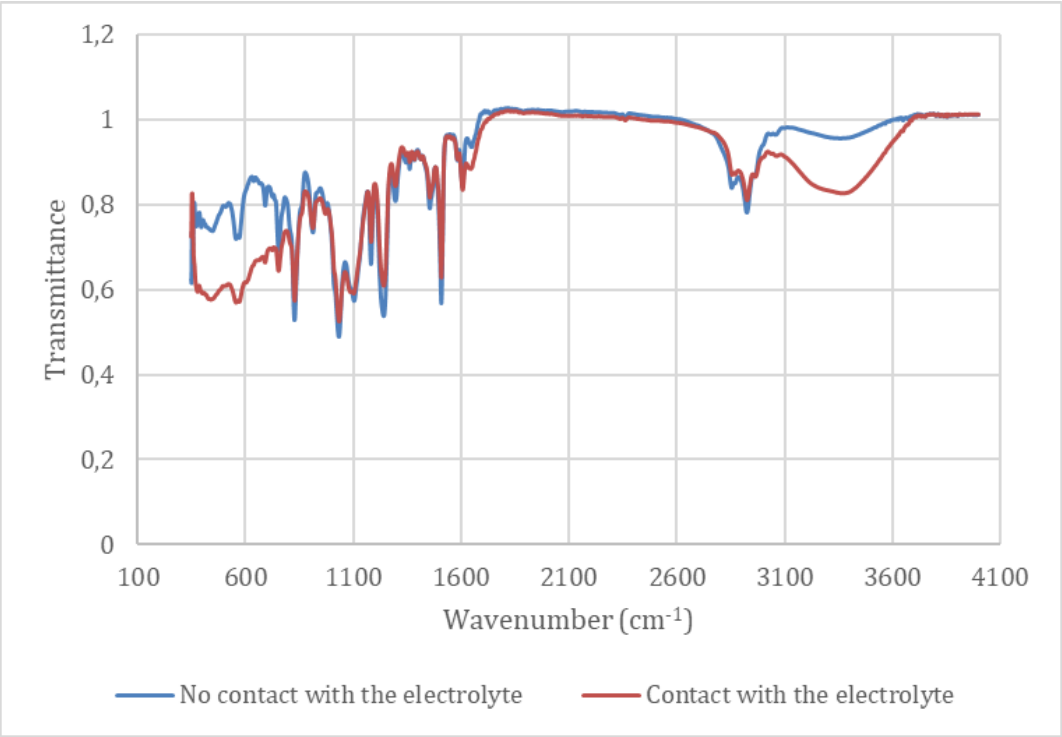

Figure B.8 FTIR spectra of test 5 (30% of ES) with and without contact with the electrolyte.

Table B.10 FTIR analysis of the peaks and bands observed in Figure B.8 for test 5 without and with contact with the electrolyte.

Peaks (cm^{-1})	Without contact with the electrolyte	With contact with the electrolyte
451, 459	O-Si-O or Si-O deformation	O-Si-O or Si-O deformation, and/or vanadium species, V-O bending, V-O stretching, -SO_4 stretching, V-O-S stretching
572 - 576	C-Cl	
696	C=C bending	---
750 - 754	C-H bending, C-Cl	
829, 831	Silica network	
908, 914	Si-OH stretch, Epoxy groups	
995	C=C bending	
1027 - 1039	Antisymmetric stretching of Si-O-Si sequence	
1105, 1108	Si-O stretching	
1182 – 1184, 1234 - 1242	S-O and/or C-N stretching	
1297	C-O-C asymmetric stretching	
1363 - 1365	O-H bending	---
1452 - 1458	C-H bending, CH_3 asymmetric stretch	
1500 - 1510	Aromatic C=C	
1602 - 1608	N-H bending	
1647	---	H_2O stretch
2860, 2867, 2925, 2929, 2964	C-H (CH_2 and CH_3) symmetric and asymmetric stretch	
3100 - 3600	SiO-H and/or O-H stretching	

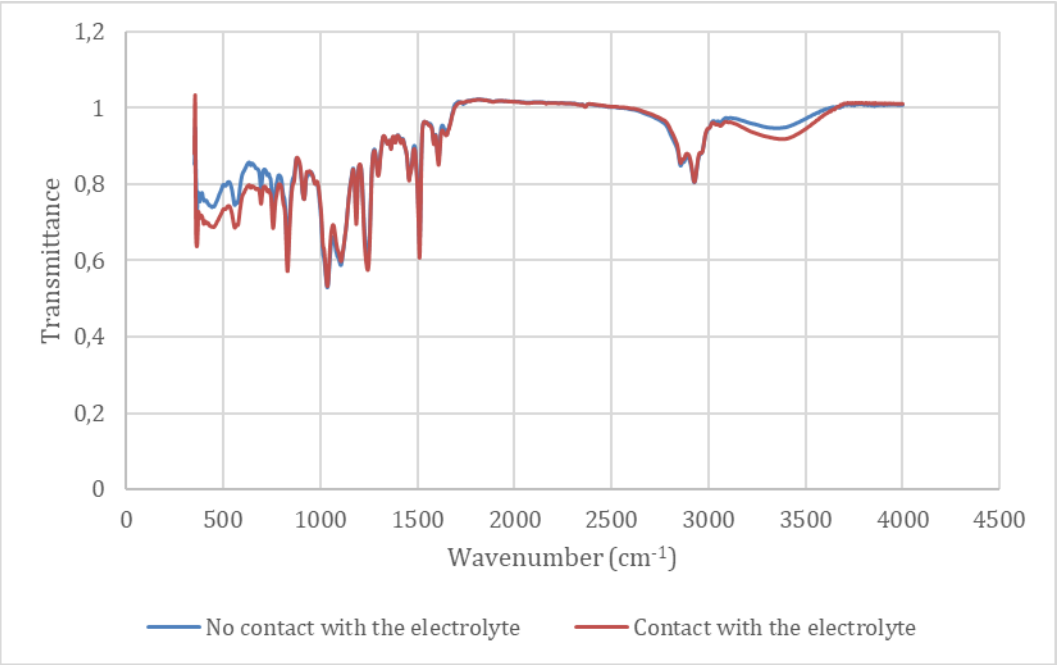

Figure B.9 FTIR spectra of test 6 (50% of ES) with and without reacting with the electrolyte.

Table B.11 FTIR analysis of the peaks and bands observed in Figure B.9 for test 6 without and with contact with the electrolyte.

Peaks (cm^{-1})	Without contact with the electrolyte	With contact with the electrolyte
459 - 462	O-Si-O or Si-O deformation	O-Si-O or Si-O deformation, and/or vanadium species, V-O bending, V-O stretching, -SO_4 stretching, V-O-S stretching
572	C-Cl	
688 - 694	C=C bending	
752 - 757	C-H bending, C-Cl	
831	Silica network	
906, 916	Si-OH stretch, Epoxy groups	
995	C=C bending	
1027 - 1037	Antisymmetric stretching of Si-O-Si sequence	
1103 - 1108	Si-O stretching	
1182, 1220, 1234, 1242, 1247	S-O and/or C-N stretching	
1290 - 1297	C-O-C asymmetric stretching	
1365	O-H bending	---
1456 - 1459	C-H bending, CH_3 asymmetric stretch	
1510	Aromatic C=C	
1602 - 1610	N-H bending	
1641 - 1654	H_2O stretch and/or O-H bending	
2858, 2925, 2929	C-H (CH_2 and CH_3) symmetric and asymmetric stretch	
3100 - 3600	SiO-H and/or O-H stretching	

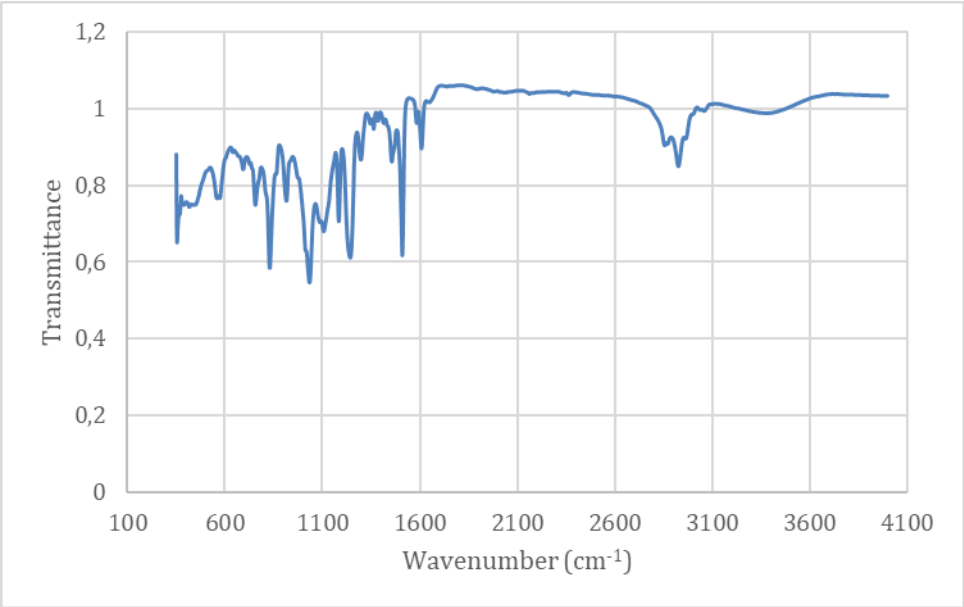

Figure B.10 FTIR spectra of test 7 (10% of AS and 41% of ES) without contact with the electrolyte.

Table B.12 FTIR analysis of the peaks and bands observed in Figure B.10 for test 7 without contact with the electrolyte.

Peaks (cm^{-1})	**Vibration**
435	O-Si-O or Si-O deformation
572	C-Cl
692	C=C bending
752	C-H bending, C-Cl
829	Silica network
914	Si-OH stretch and/or epoxy groups
1031	Antisymmetric stretching of Si-O-Si sequence
1107	Si-O stretching
1180, 1242	C-N stretching
1299	C-O-C asymmetric stretching vibration of epoxy group
1361	O-H bending
1456	C-H bending and/or CH_3 asymmetric stretch
1510	aromatic C=C
1579	C=C stretching
1606	N-H bending
2856	C-H stretch
2927, 2966	C-H symmetric and asymmetric stretch
3200-3600	SiO-H and/or O-H stretching

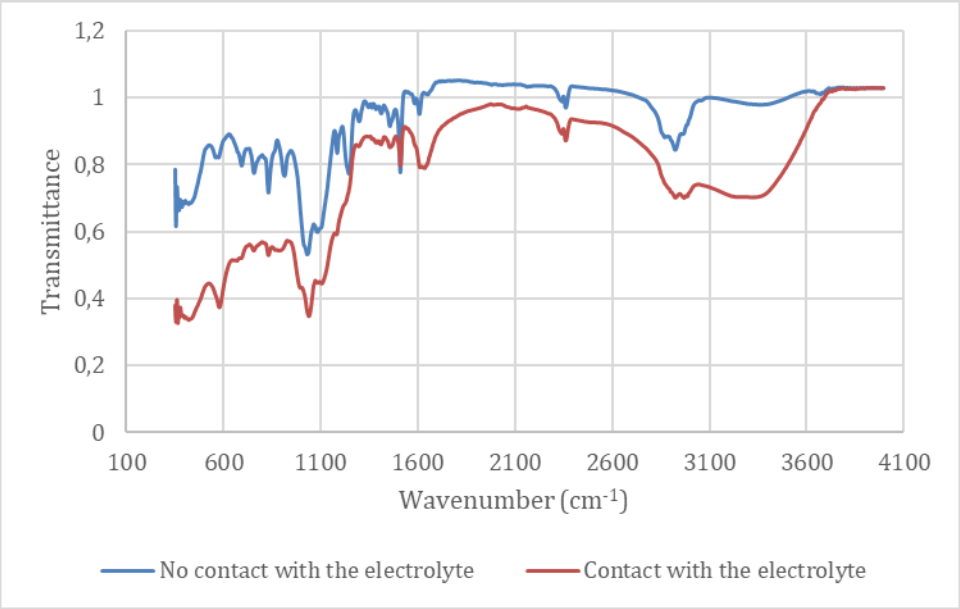

Figure B.11 FTIR spectra of test 8 (30% of AS and 73% of ES) with and without contact with the electrolyte.

Table B.13 FTIR analysis of the peaks and bands observed in Figure B.11 for test 8 with and without contact with the electrolyte.

Peaks (cm^{-1})	Without contact with the electrolyte	With contact with the electrolyte
430	O-Si-O or Si-O deformation	O-Si-O or Si-O deformation, and/or vanadium species, V-O bending, V-O stretching, -SO_4 stretching, V-O-S stretching
574	C-Cl	
690 - 692	C=C bending	
756	C-H bending, C-Cl	
829	Silica network	
914	Si-OH stretch, Epoxy groups	
1033, 1039	Antisymmetric stretching of Si-O-Si sequence	
1085	Si-O stretching	
1226, 1245	S-O and/or C-N stretching	C-N stretching
1296	C-O-C asymmetric stretching vibration of epoxy group	
1498	C-H bending, CH_3 asymmetric stretch	
1508, 1510	Aromatic C=C	
1606	N-H bending	
1635	---	H_2O stretch and/or O-H bending
2364	---	H_2O stretch and/or O-H bending
2873 - 2925	C-H (CH_2 and CH_3) symmetric and asymmetric stretch	
3100 - 3600	SiO-H and/or O-H stretching	

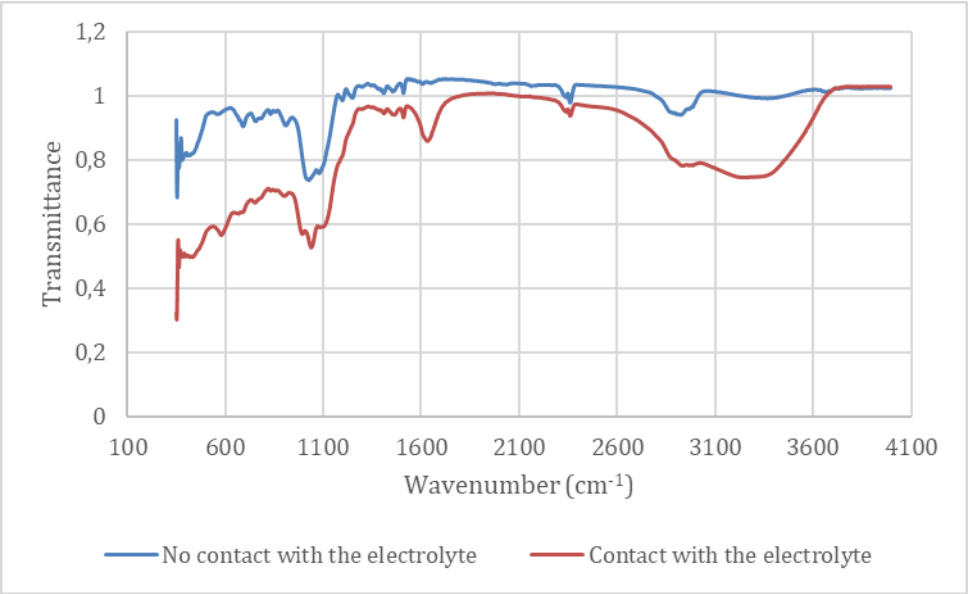

Figure B.12 FTIR spectra of test 9 (50% of AS and 86% of ES) with and without reacting with the electrolyte.

Table B.14 FTIR analysis of the peaks and bands observed in Figure B.12 for test 9 with and without contact with the electrolyte.

Peaks (cm^{-1})	Without contact with the electrolyte	With contact with the electrolyte
430	O-Si-O or Si-O deformation	O-Si-O or Si-O deformation, and/or vanadium species, V-O bending, V-O stretching, -SO_4 stretching, V-O-S stretching
574	C-Cl	
690 - 692	C=C bending	
756	C-H bending, C-Cl	
829	Silica network	
914	Si-OH stretch, Epoxy groups	
1033, 1039	Antisymmetric stretching of Si-O-Si sequence	
1085	Si-O stretching	
1226, 1245	S-O and/or C-N stretching	C-N stretching
1296	C-O-C asymmetric stretching vibration of epoxy group	
1498	C-H bending, CH_3 asymmetric stretch	
1508, 1510	Aromatic C=C	
1606	N-H bending	
1635	---	H_2O stretch and/or O-H bending
2364	---	H_2O stretch and/or O-H bending
2873 - 2925	C-H (CH_2 and CH_3) symmetric and asymmetric stretch	
3100 - 3600	SiO-H and/or O-H stretching	

Appendix C. EIS measurements

In Table C.1, the values of impedance provided by the software are presented. In Table C.2, the values of Table C.1 were respectively multiplied by the active area of the electrodes and the imaginary impedance values were multiplied by -1, to perform the Nyquist plots.

Table C.1 Values of impedance retrieved form Thales software for each test.

Test 1 (with film)		Test 2 (without film)	
Real impedance (Ω)	–Imaginary impedance (Ω)	Real impedance (Ω)	–Imaginary impedance (Ω)
0,155	-0,192	0.256	-0.139
0.154	-0.135	0.257	-0.0938
0.154	-0.0941	0.260	-0.0612
0.154	-0.0636	0.265	-0.0369
0.156	-0.0410	0.269	-0.0193
0.158	-0.0236	0.273	-0.00575
0.161	-0.0103	0.278	0.00529
0.165	0.000183	0.282	0.0143
0.170	0.00843	0.289	0.0221
0.175	0.0150	0.294	0.0292
0.182	0.0200	0.303	0.0361
0.189	0.0233	0.311	0.0428
0.197	0.0251	0.320	0.0496
0.204	0.0249	0.333	0.0561
0.211	0.0235	0.347	0.0618
0.217	0.0211	0.365	0.0661
0.221	0.0182	0.382	0.0678
0.225	0.0152	0.400	0.0667
0.228	0.0125	0.418	0.0624
0.229	0.0105	0.432	0.0556
0.231	0.00848	0.445	0.0474
0.232	0.00689	0.453	0.0392
0.233	0.00568	0.459	0.0316
0.233	0.00456	0.464	0.0256
0.234	0.00394	0.466	0.0209
0.235	0.00340	0.469	0.0172
0.235	0.00300	0.471	0.0146
0.235	0.00266	0.473	0.0128
0.236	0.00251	0.475	0.0116
0.236	0.00240	0.477	0.0105
0.237	0.00243	0.478	0.00990
0.237	0.00261	0.480	0.00983
0.238	0.00257	0.482	0.00906
0.238	0.00258	0.483	0.00862
0.239	0.00302	0.485	0.00823
0.239	0.00353	0.487	0.00869

Test 1 (with film)		Test 2 (without film)	
Real impedance (Ω)	–Imaginary impedance (Ω)	Real impedance (Ω)	–Imaginary impedance (Ω)
0.240	0.00409	0.486	0.00991
0.241	0.00428	0.488	0.0116
0.241	0.00473	0.489	0.0130
0.242	0.00551	0.493	0.0137
0.243	0.00625	0.496	0.0186
0.244	0.00818	0.511	0.0188
0.247	0.00943	0.508	0.0229
0.249	0.0103	0.518	0.0193
0.252	0.00861	0.524	0.0138
0.254	0.00719	0.537	0.00796
0.255	0.00582	0.529	0.00855
0.255	0.00461	---	---
0.255	0.00388	---	---
0.256	0.00329	---	---

Table C.2 Values of real impedance and symmetric values of imaginary impedance multiplied by the active area to do the Nyquist plot.

Test 1 (with film)		Test 2 (without film)	
Re(Z) (Ω·cm^2)	-Im(Z) (Ω·cm^2)	Re(Z) (Ω·cm^2)	-Im(Z) (Ω·cm^2)
0.620	-0.768	1.02	-0.557
0.615	-0.542	1.03	-0.375
0.615	-0.376	1.04	-0.245
0.618	-0.254	1.06	-0.148
0.624	-0.164	1.08	-0.077
0.633	-0.0944	1.09	-0.0230
0.645	-0.0411	1.11	0.0211
0.660	0.000731	1.13	0.0571
0.679	0.0337	1.16	0.0883
0.701	0.0599	1.18	0.117
0.727	0.0800	1.21	0.144
0.756	0.0934	1.24	0.171
0.786	0.100	1.28	0.198
0.816	0.0998	1.33	0.224
0.844	0.0940	1.39	0.247
0.867	0.0842	1.46	0.264
0.885	0.0727	1.53	0.271
0.899	0.0609	1.60	0.267
0.910	0.0501	1.67	0.250
0.918	0.0419	1.73	0.222
0.923	0.0339	1.78	0.189
0.928	0.0276	1.81	0.157
0.931	0.0227	1.84	0.126
0.934	0.0182	1.85	0.102

Test 1 (with film)		Test 2 (without film)	
Re(Z) ($\Omega \cdot cm^2$)	-Im(Z) ($\Omega \cdot cm^2$)	Re(Z) ($\Omega \cdot cm^2$)	-Im(Z) ($\Omega \cdot cm^2$)
0.936	0.0158	1.86	0.0838
0.938	0.0136	1.88	0.0690
0.940	0.0120	1.88	0.0584
0.942	0.0107	1.89	0.0513
0.944	0.0100	1.90	0.0465
0.945	0.00959	1.91	0.0418
0.947	0.00971	1.91	0.0396
0.948	0.0104	1.92	0.0393
0.950	0.0103	1.93	0.0363
0.952	0.0103	1.93	0.0345
0.954	0.0121	1.94	0.0329
0.957	0.0141	1.95	0.0347
0.960	0.0163	1.95	0.0396
0.963	0.0171	1.95	0.0465
0.966	0.0189	1.96	0.0520
0.968	0.0220	1.97	0.0548
0.973	0.0250	1.99	0.0744
0.977	0.0327	2.05	0.0752
0.986	0.0377	2.03	0.0915
0.997	0.0413	2.07	0.0773
1.01	0.0345	2.10	0.0552
1.01	0.0288	2.15	0.0318
1.02	0.0233	2.12	0.0342
1.02	0.0184	---	---
1.02	0.0155	---	---
1.02	0.0132	---	---

In Figures C.1 and C.2. the Nyquist plots are presented for tests 1 and 2. respectively.

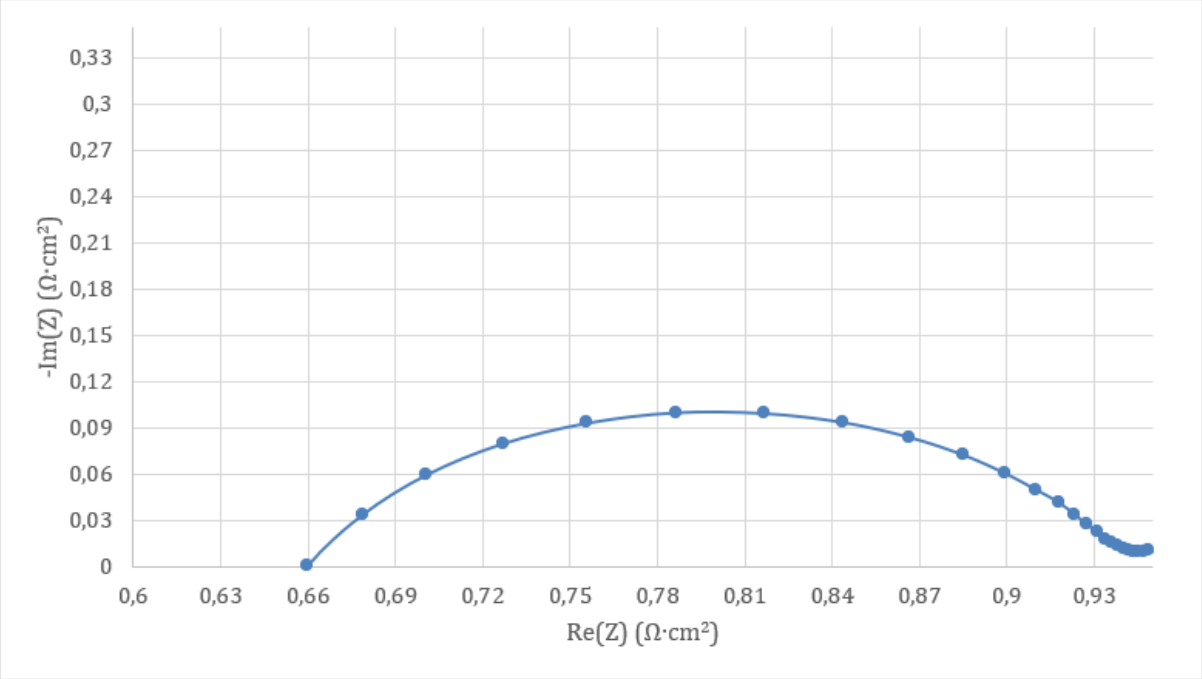

Figure C.1 Nyquist plot for test 1 (with film).

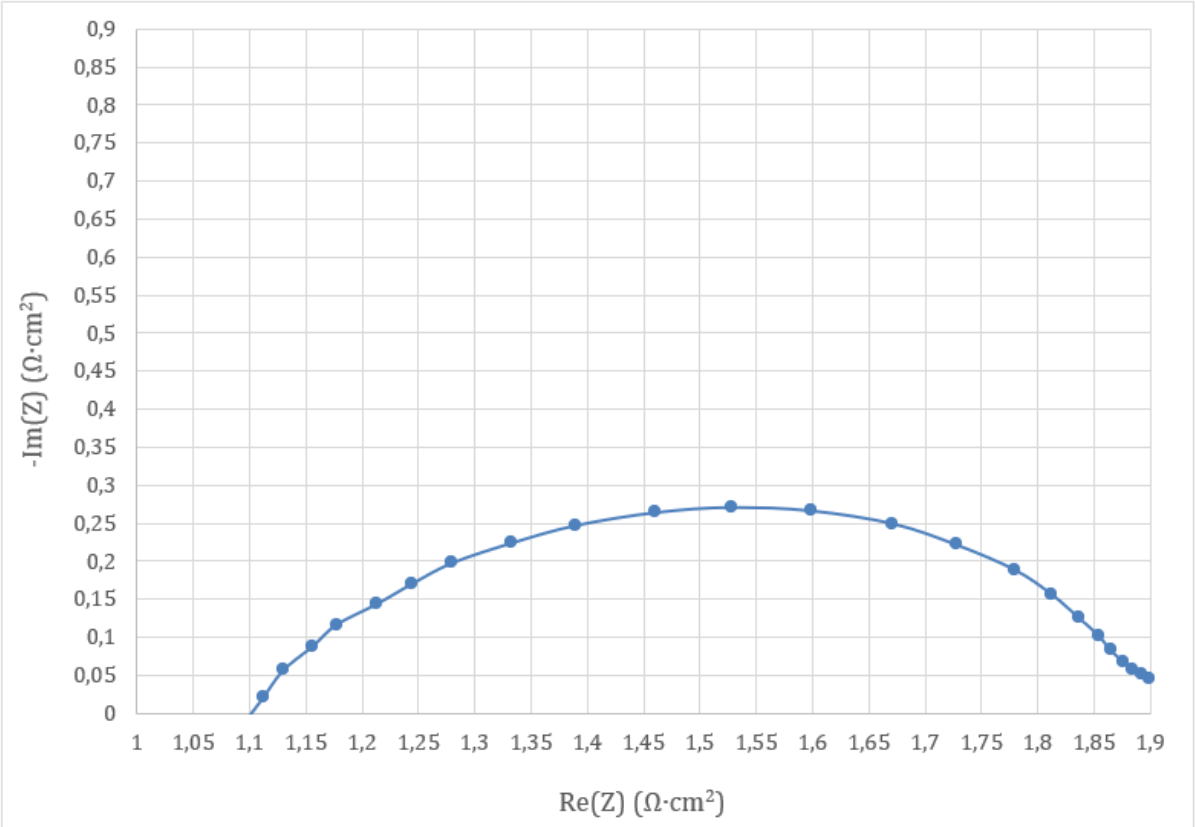

Figure C.2 Nyquist plot for test 2 (standard cell assembly).

The determination of the diameter of the semicircle is here explained for test 1 (the same method was followed for test 2):

First. two values of Re(Z) with the same -Im(Z) were chosen – for -Im(z)=0.03 Ω·cm^2. there are two Re(Z) values:

$$Re(Z)_1 = 0.926\ \Omega\cdot cm^2 \quad (C.1)$$

$$Re(Z)_2 = 0.676\ \Omega\cdot cm^2 \quad (C.2)$$

$$Re(Z)_1 - Re(Z)_2 = 0.250\ \Omega\cdot cm^2 \quad (C.3)$$

So. the value of Re(Z) for the centre point of the semicircle should be as calculated in equation C.4:

$$Re(Z)_{centre} = \frac{Re(Z)_1 - Re(Z)_2}{2} + Re(Z)_2 = 0.801\ \Omega\cdot cm^2 \quad (C.4)$$

The value of -Im(Z) for the centre of the semicircle is $-Im(Z)_{centre} = 0.101\ \Omega\cdot cm^2$. which corresponds to its radius. therefore. the values of Re(Z) where the semicircle crosses the horizontal axis are in equations C.5 and C.6. In equation C.7 is the determination of the charge transfer resistance

$$x_{centre1} = Re(Z)_{centre} - (-Im(Z)_{centre}) = 0.700\ \Omega\cdot cm^2 \quad (C.5)$$

$$Re(Z)_2 = Re(Z)_{centre} + (-Im(Z)_{centre}) = 0.902\ \Omega\cdot cm^2 \quad (C.6)$$

$$R_{TC} = Re(Z)_2 - x_{centre1} = 0.202\ \Omega\cdot cm^2 \quad (C.7)$$